2012

Low temperature carbon material deposition with photo-enhanced chemical vapor deposition

KyungNam Kang
Louisiana State University and Agricultural and Mechanical College

LOW TEMPERATURE CARBON MATERIAL DEPOSITION WITH PHOTO-ENHANCED CHEMICAL VAPOR DEPOSITION

A Dissertation

Submitted to the Graduate Faculty of the
Louisiana State University and
Agricultural and Mechanical College
In partial fulfillment of the
Requirements for the degree of
Doctor of Philosophy

in

Division of Electrical and Computer Engineering
School of Electrical Engineering and Computer Science

by
KyungNam Kang
B.S., Chung-Ang University, Korea, 1999
M.E., Texas A&M University, 2003
M.S., Louisiana State University, 2007
December 2012

ACKNOWLEDGEMENTS

Though only my name appears on the cover of this dissertation, a great many people have contributed to its production. I would like to express to all those who gave me the chance to complete this dissertation.

First of all, I want to thanks to my advisor Dr. Pratul K. Ajmera. I have been incredibly lucky to have an advisor who gave me the independence to explore on my own, and at the same time his advice to recover when I was embarrassed. Dr. Ajmera taught me how to think, solve and improve ideas. His patience and support helped me overcome many crisis situations and finish this dissertation. I hope that one day I would become as good an advisor to my students as Dr. Ajmera has been to me.

I am also grateful to the committee members. I am truly indebted and thankful to my supervisor at CAMD, Dr. Yoonyoung Jin. His careful concern of my daily life and academic and technical teaching supported to overcome from my failures. Dr. Theda Daniels-Race is one of the best teachers who I have had in my life. I am grateful to Daniels-Race for her encouragement and practical advice. I will never forget her generous smile. I am also indebted to Dr. Murphy. His acceptance of my committee member should not be easy but his regard for the feeling of students makes to be a committee member.

I would like to acknowledge Dr. Jin-Woo Choi, Dr. Jost Goettert, Dr. Daniel Park, Dr. Seung-Jong Park and Dr. Hak-Chul Shin for numerous discussions and lectures on related topics that helped me improve my knowledge in the area.

I am obliged to many of my colleagues who supported me. Especially I appreciate Jeonghwan Kim, Edward Song and JunSeo Choi for social and academic connections. Their support and care helped me overcome setbacks and stay focused on my graduate study. I greatly

value their friendship and I deeply appreciate their belief in me. I am also appreciative to Golden Hwang, who is former EMDL manager. He helped during my experiment in EMDL.

Most outstandingly, none of this would have been possible without the love and patience of my wife, Su Bok Jeong. I would like to express my heart-felt gratitude to my family and my in-laws.

THANK YOU ALL AND LOVE YOU

TABLE OF CONTENTS

LIST OF TABLES

LIST OF FIGURES

ABSTRACT

Photo-enhanced chemical vapor deposition (CVD) technique is investigated here for low temperature deposition of carbon nanotubes (CNTs) and hexagonal diamond. Most current deposition methods require high substrate temperature. Photo-enhanced CVD utilizes light energy to dissociate carbon containing precursor molecules and hence has a potential for low temperature deposition. CCl_4, having a high absorption coefficient compared to other commonly employed hydrocarbons in the UV emission spectrum from a Xe arc lamp, is selected as a carbon precursor in this work.

Extensive experimentation conducted by varying Al/Ni/Al catalyst layer thicknesses on SiO_2 coated Si substrates, substrate annealing temperature in the range 350 - 450 °C for 25 min, and chamber pressure in the range 0.22 - 10 Torr in ammonia ambient, yielded suitable catalyst layers of thicknesses 3/2/3, 5/1/5 and 5/3/5 nm and annealing pressure of 10 Torr. For photo-enhanced CVD deposition, experiments are conducted with various Ar/CCl_4 flow ratio in 1.5 - 19 range, total chamber pressure in 3 - 10 Torr range, and substrate temperatures in 350 - 450 °C range.

Optimal condition for CNT deposition in this work is found to be 30 min at 400 °C at 5 Torr total pressure with Ar/CCl_4 ratio of 9 with 5/1/5 nm thick catalyst annealed at 400 °C. Raman spectroscopy indicates MWCNT growth and I-V measurements yield sheet resistivity of 22 kΩ/sq.

The densest hexagonal diamond deposition is obtained at 450 °C, 3 hr deposition time, at 10 Torr with Ar/CCl_4 ratio of 2.3 with 5/3/5 nm thick catalyst annealed at 450 °C. Lesser dense hexagonal diamond platelets are obtained at 450 °C, 3 hr deposition time, at 10 Torr with Ar/CCl_4 ratio of 2.3 with 3/2/3 nm thick catalyst annealed at 450 °C.

Based on the physical structures observed at various stages of growth in SEM images, a model is proposed for nucleation and subsequent growth of hexagonal diamond platelets with graphene layer playing role both during nucleation and during platelet growth. Raman spectroscopy and XPS results confirm the deposition material to be hexagonal diamond. The grown material is characterized with UV-Vis spectroscopy for optical and with a nanoindenter for electrical and mechanical properties.

CHAPTER 1. INTRODUCTION

1.1 Motivation

There are several carbon allotropes such as graphite, graphene, carbon nanotubes, carbon nanofiber and diamond. Those materials have their own unique properties. This research is focused on carbon nanotubes and hexagonal diamond.

Carbon nanotubes (CNTs) have high electrical conductivity, surface to volume ratio, stiffness and good thermal conductivity. Carbon nanotubes have been researched intensively because of their interesting properties. There are many conventional CNT deposition methods such as arc-discharge [1], laser ablation [2], plasma enhanced chemical vapor deposition (PECVD) [3] and thermal chemical vapor deposition (CVD) [4]. In general, these methods need a high substrate temperature typically over 500 °C to deposit CNTs. However, a high deposition temperature limits its application in certain cases. For example, when the deposition temperature is higher than about 450 °C, it is difficult to use CNTs as an interconnect layer in the standard semiconductor integrated circuit (IC) industry. Also, large area and selective area deposition are desirable. Thermal CVD method for CNT synthesis is convenient for large area deposition for mass production, but it has certain limitations in selective area deposition. PECVD can deposit at low temperatures under 400 °C, but it has difficulty for large area and/or selective area deposition. These limitations of low substrate temperature, large area and selective area deposition capability cannot be overcome with conventional CNT deposition methods.

Hexagonal diamond is an allotropic form of carbon and is called lonsdaleite. It is a harder material than cubic diamond. The structure of cubic diamond and hexagonal diamond respectively correspond to the zinc blende and the wurtzite structures. Hexagonal diamond is rare

because the structural energy of hexagonal diamond is higher than that of cubic diamond. In general, it can be found in meteorites. There are several methods to synthesize hexagonal diamond such as static-pressure [5], shock-compression [6], shock wave impulsion [7], pulsed laser impulsion [8], microwave PECVD [9] and hot filament CVD method [10]. In general, hexagonal diamond is synthesized by applying high pressure and temperature to hexagonal graphite (HG). This physical method theoretically needs extremely high pressure (>12 GPa) and high temperature (~ 1000 ˚C) [11]. The CVD method does not need such an extreme condition, however, it is difficult to obtain high purity hexagonal diamond. The hexagonal diamond is usually found with other carbon materials such as cubic diamond, graphite or amorphous carbon obtained by CVD synthesis at high temperature (~ 800 ˚C) on specially treated substrate surface such as nano-crystalline diamond or h-GaN strained films [10].

Motivation in this work is to investigate photo-enhanced CVD as a different and an alternate method for deposition of CNT and other allotropic forms of carbon. It has promise for low-temperature growth for CNTs and also for hexagonal diamond as discussed below.

In this research, photo-enhanced CVD method is utilized to deposit CNT and hexagonal diamond at low substrate temperatures. This, to our knowledge, is a new method for CNT and hexagonal diamond deposition at low substrate temperature that has not been attempted earlier. This method has been employed earlier for other semiconductor growth at low temperature in our laboratory [12]. The photo-enhanced CVD system is somewhat similar to the thermal CVD system and retains many of the advantages of the thermal CVD growth process. However, photon energy assists the precursor decomposition either photolytically or pyrolytically. Thus CNT can be deposited at low bulk substrate temperature. A growth temperature below 450 °C is

desirable for compatibility with standard CMOS IC fabrication process. Also, large area and selective deposition is desirable for a number of applications.

1.2 Background on Carbon Materials

Carbon, the backbone of organic materials, having atomic number six has six electrons with two in the K-shell ($1S^2$) and four in the L-shell ($2S^2$, $2P^2$). The binding energy of two core electrons in K-shell is large and they are not involved in chemical reactions. However, the binding energies of four valence electrons in the L-shell are smaller and they are involved in forming chemical bonds. These four valence electrons form hybrid orbitals such as sp^3, sp^2 and sp. The structure of carbon atom depends on the type of hybridization and determines the nature of the carbon material. Table 1.1 shows different forms of carbon and their valence hybridization orbitals, bond length and bond energy. Figure 1.1 shows the diamond and graphite structures of carbon.

Table 1.1. Hybridization type and bonding details for various forms of carbon [13–14].

	Hybridization				
	sp^3		sp^2		sp
Form of carbon material	Diamond	Hexagonal diamond	Graphite	Nanotube	Carbynes
Bond length (nm)	0.1536	0.1538	0.142	0.144	0.121
Bond energy (eV/atom)	7.2	Less than 7.2	7.4	Less than 7.4	8.67

In carbon, there are two electrons in 2S orbital, and two electrons in 2P orbital in the ground state. However, the electron distribution can be changed to one electron in 2S orbital, and

three electrons in 2P orbitals for the excited state. This excited state reduces energy difference between 2S and 2P orbitals through hybridization by mixing 2S and 2P orbitals. For instance, sp^3 hybridization occurs when 2S orbital combines with three 2P orbitals, sp^2 hybridization occurs when 2S orbital combines with two 2P orbitals and sp hybridization occurs when 2S orbital mixes with one 2P orbital. There are four sp^3 orbitals, which are 109.5° apart from each other and form σ bonds resulting in the diamond crystal structure. There are three sp^2 orbitals, which are 120° apart from each other and result in graphite structure. As indicated in Table 1, the sp^2 bond in graphite is stronger than the sp^3 bond in diamond.

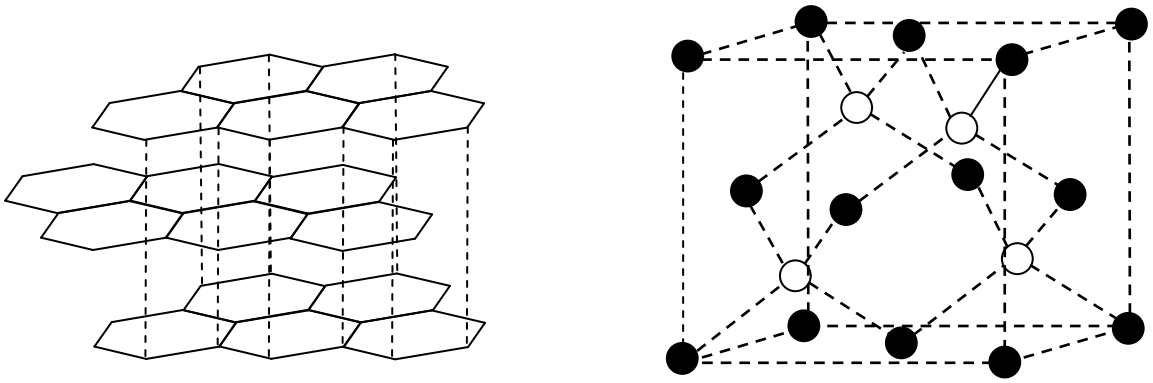

(a) (b)

Figure 1.1. Structures of (a) graphite and (b) diamond forms of carbon.

1.3 Carbon Nanotube

Carbon nanotube (CNT) is a cylindrical shape formed by carbon atoms arranged in a honeycomb lattice. The CNT diameter can vary from a few nanometers to tens of nanometers according to the size of catalyst. CNT can be classified by the number of walls as either single-

wall (SWCNT) or as multi-wall CNT (MWCNT). SWCNT has one cylindrical shell and MWCNT consists of two or more co-axial cylindrical shells.

The CNTs were discovered by Iijima in 1991 [1]. The first discovered CNTs were MWCNT. Iijima deposited SWCNT by using an arc discharge method in 1993 [15]. A SWCNT can be looked upon as a single graphene layer that closes on itself. The SWCNTs can be classified by chirality depending on the carbon atom arrangement. The atomic arrangement of an achiral CNT has reflection symmetry on a mirror plane perpendicular to the CNT axis but that of a chiral CNT does not. Achiral SWCNTs can be separated into two types by its chiral vector as an armchair or as a zigzag type [16]. These types can be classified by the arrangement of carbon atoms along the cross section of a CNT. Armchair type of CNT has cis-type while the zigzag type of CNT has trans-type cross-sections at the ends respectively as shown in Fig.1.2. A chiral type of CNT has a mixture of cis and trans types of carbon arrangement at the cross section end.

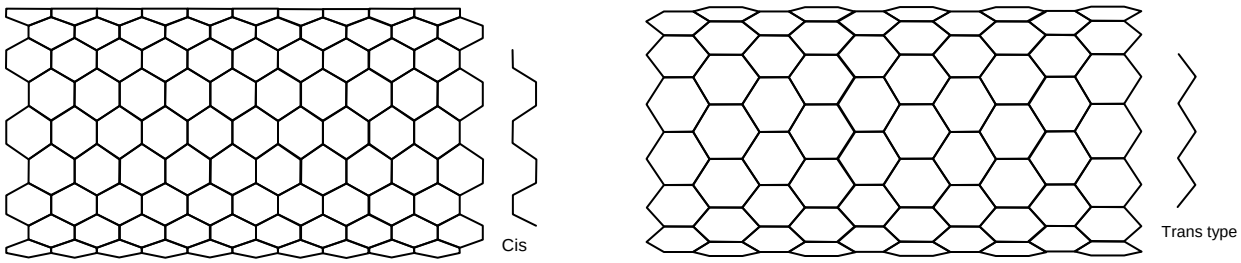

Figure 1.2. Achiral SWCNT cross sections. (a) armchair type ("cis-type" of carbon arrangement) and (b) zigzag ("trans-type" of carbon arrangement).

Figure 1.3 shows an unfolded chiral SWCNT surface indicated by the dotted line segment ABED. The unit cell of CNT is formed by folding the dotted line segment ABED so that both end points (A and B) of the chiral vector $\vec{C} = \overrightarrow{AB}$ are the same point for the CNT. Of course, D and E also represent the same point for the CNT. The chiral vector $\vec{C}$ and translational vector $\vec{T}$

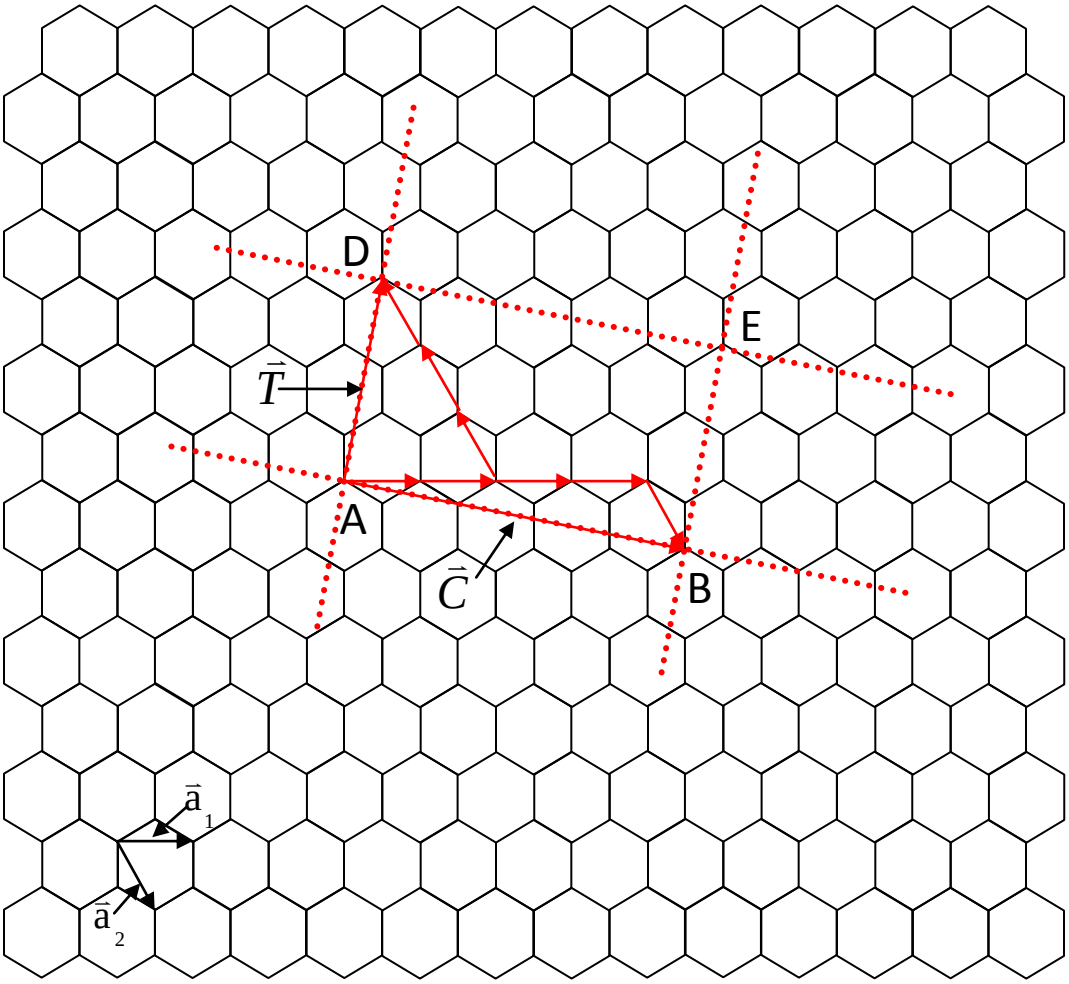

Figure 1.3. Structure of an unfolded SWCNT. $\vec{C}$ is the chiral vector and $\vec{T}$ is the translational vector. $\vec{a}_1$ and $\vec{a}_2$ are lattice unit vectors. For the case shown, $\vec{T} = \overrightarrow{AD} = 2\vec{a}_1 - 3\vec{a}_2$ and $\vec{C} = \overrightarrow{AB} = 4\vec{a}_1 + \vec{a}_2$. This is an example of a chiral SWCNT with chirality (4,1).

in Fig. 1.3 can be defined by the combination of lattice unit vectors $\vec{a}_1$ and $\vec{a}_2$. The magnitude of chiral vector $\vec{C} = \overrightarrow{AB}$ is the same as the circumference of CNT. The end point of the translational vector $\vec{T} = \overrightarrow{AD}$ shown as point D is the closest point isotropic to the starting point A. The cylindrical axis of the CNT is perpendicular to the chiral vector $\vec{C}$ and parallel to the translational vector $\vec{T}$. The chiral vector $\vec{C}$ and translational vector $\vec{T}$ can always be written as: $\vec{C} = n\vec{a}_1 + m\vec{a}_2$; (n and m are integers), and $\vec{T} = t_1\vec{a}_1 + t_2\vec{a}_2$; ($t_1$ and t_2 are integers).

The circumference of CNT $\left|\vec{C}\right| = \sqrt{\vec{C}\cdot\vec{C}} = a\sqrt{n^2 + m^2 + nm}$, where $a = \left|\vec{a}_1\right| = \left|\vec{a}_2\right|$ and $\vec{a}_1 \bullet \vec{a}_2 = a^2 \cos 60^\circ = 0.5a^2$. The unit cell ABED of a CNT is defined by its chiral and translational vectors. The unit cell gives the characteristic arrangement of atoms in a CNT and the latter consists of reiteration of the unit cell. The number of hexagons N in the unit cell of SWCNT can be calculated from $\vec{C}, \vec{T}$, $\vec{a}_1$ and $\vec{a}_2$ and is given by

$$N = \frac{(\vec{C} \times \vec{T})}{(\vec{a}_1 \times \vec{a}_2)}.$$

For armchair SWCNT $n = m$ and $n, m \neq 0$, for zigzag SWCNT $m = 0$ and for chiral SWCNT $n \neq m$ and $n, m \neq 0$. Electrical property of SWCNT depends on chirality. All armchair and some zigzag SWCNTs, for which the integer value of n is also a multiple of three, have metallic properties. All other SWCNTs which are chiral and rest of the zigzag SWCNTs have semiconducting properties. The metallic SWCNTs have better electrical conductivity than MWCNTs.

The MWCNTs were the first CNTs discovered by Iijima in 1991 while conducting research for fullerene utilizing arc-discharge method. In general, calculating electrical property of MWCNTs is complicated. Hence, electrical properties of double-wall and four-wall CNTs

were calculated first [17–18]. The electrical property of MWCNTs depends on the property of each of the SWCNTs comprising the MWCNT. For instance, a double-wall CNT may represent both metallic and semiconducting properties if the two coaxial SWCNTs comprising the double-wall CNT respectively have metallic and semiconducting properties [19–20]. In general, the structures of co-axial CNTs comprising a MWCNTs are not necessary commensurate with each other. It means that if the first CNT is achiral, then next CNT need not be achiral. It could be either achiral or chiral for a given MWCNT. Combination of armchair and zigzag CNTs in a MWCNTs is possible. If first CNT is armchair, then the next CNT can also be armchair for a MWCNT [21].

1.4 Hexagonal Diamond

Hexagonal diamond is one of carbon allotropes. It was found in meteorite [22]. It has the same sp^3 hybridization as the cubic diamond structure. The structures of cubic and hexagonal diamond respectively correspond to the zinc blende and the wurtzite structures. The cubic diamond has only chair rings. However, hexagonal diamond has mixed chair and boat rings. Chair configuration has four carbon atoms on a plane and the remaining two carbon atomss locate on the opposite side of the plane. The boat configuration has four carbon atoms on a plane and the remaining two carbons locate on the same side of the plane. Figure 1.4 shows the chair and boat configurations. The figure shows numbered carbon atoms. The 2, 3, 4 and 5 carbon atoms in the chair and the boat configuration are in the same plane. The 1 and 6 carbon atoms are on the opposite sides of the plane in the chair configuration but are on the same side of the plane in the boat configuration.

The chair configuration has less energy than the boat configuration and hence the total energy of hexagonal diamond is higher than that of the cubic diamond. That is the reason why cubic diamond is more stable than hexagonal diamond [23].

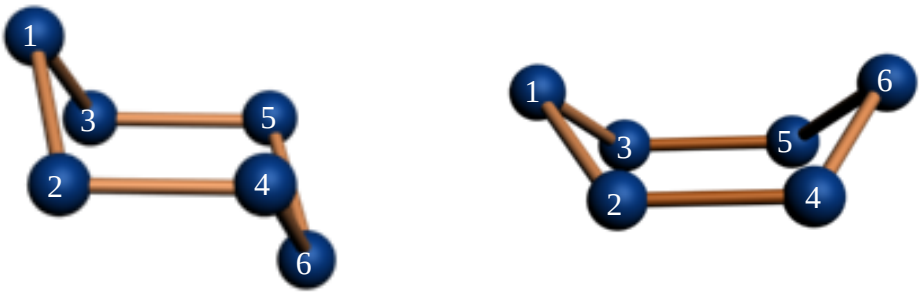

Figure 1.4. (a) The chair configuration and (b) the boat configuration of carbon atoms.

Figure 1.5 shows (111) planes of the cubic and the hexagonal diamond structures. The lattice constant of cubic diamond is 3.57 Å and that of hexagonal diamond is $a = 2.52$ Å and $c = 4.12$ Å.

The synthesis methods for hexagonal diamond can be classified as physical or chemical method. Physical method is more popular than chemical method for hexagonal diamond synthesis. Physical methods include solid to solid transformation such as graphite to hexagonal diamond or cubic diamond to hexagonal diamond by applying high pressure and high temperature. Hexagonal diamond was first synthesized under high pressure (>130 Kbar) and high temperature (> 1000˚C) by Bundy [5]. The simulation results show hexagonal diamond is harder than cubic diamond [24] and has smaller band gap than cubic diamond [25].

Limited information is currently available on hexagonal diamond because of difficulties in synthesizing this material.

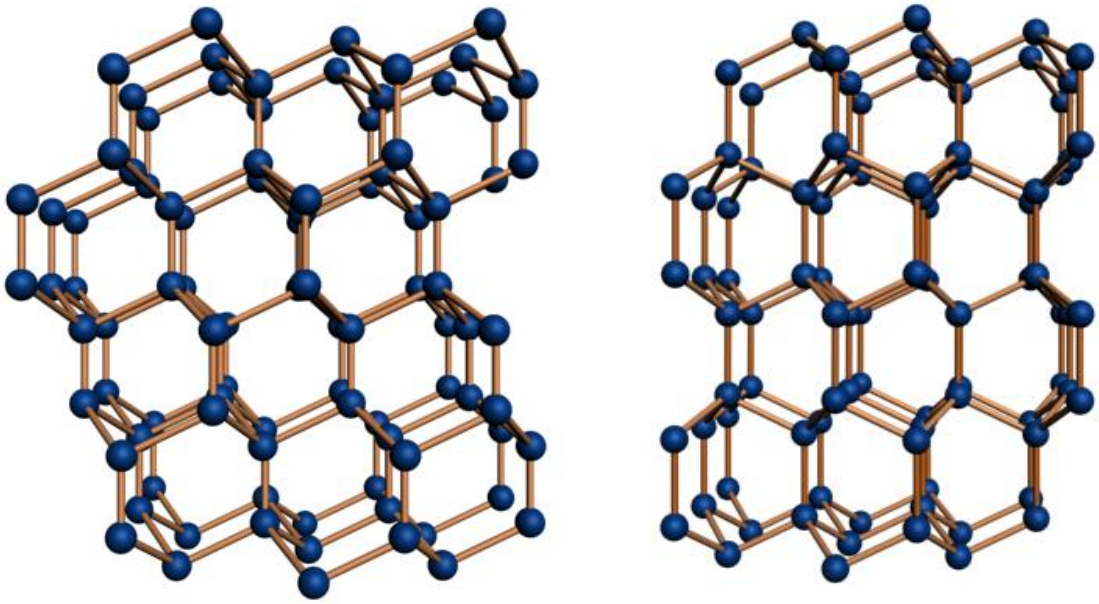

Figure 1.5. (a) (111) plane of cubic diamond structure and (b) (111) plane of hexagonal diamond structure. The (111) planes are parallel to the plane of the paper.

1.5 Research Objectives

The purpose of this research is to develop photo-enhanced CVD as an alternative method for carbon material synthesis under low substrate temperature and in selective areas. Low substrate temperature and selective area deposition are important for semiconductor device applications.

Chapter 2 reviews the background for CNT and hexagonal diamond deposition. The various catalysts, precursors, deposition temperatures and deposition methods are discussed.

Chapter 3 provides the historical background of photo-enhanced CVD method. The experimental setup for this research is discribed.

Chapter 4 gives the preparation of catalyst and precursor used for the photo-enhanced CVD growth. Annealing conditions for the catalyst for the hexagonal diamond and for the CNT

deposition are discussed. The growth parameters such as substrate temperature, annealing conditions and deposition conditions are described.

Chapter 5 discusses the results of hexagonal diamond and CNT deposition.

In chapter 6, the deposition mechanism of hexagonal diamond is proposed. The deposited hexagonal diamond and CNT layers are characterized. The characterization includes SEM images, Raman spectra, Young's modulus, XRD, XPS data, UV-VIS absorption and I-V curves.

Chapter 7 provides summary and conclusions of this work. Also, suggestions for future work on carbon material deposition with photo-enhanced CVD are given.

CHAPTER 2. BACKGROUND OF CARBON NANOTUBE AND HEXAGONAL DIAMOND DEPOSITION

2.1 CNT Growth Temperature

Substrate temperature in a CNT deposition process plays a critical role. For a CVD deposition technique, if the deposition temperature is kept too low, it is difficult to synthesize CNTs. If the temperature of CNT deposition process is kept too high, amorphous carbon can also be deposited on the catalyst thereby preventing CNT from growing and reducing the CNT yield.

In general, there are two temperatures of interest in a CNT deposition process. One temperature is associated with catalyst nanoparticle preparation and the other is the temperature for CNT deposition. If catalyst nanoparticles are prepared chemically utilizing processes such as sol-gel or impregnation method, the temperature required can be below 200 °C. However, physical catalyst nanoparticle preparation involving sputtering or electron beam evaporation generally needs a higher temperature since it usually involves annealing of deposited metal thin films to form nanoparticles. The temperature necessary for physical catalyst nanoparticle preparation depends on ambient gas, type of CNT synthesis and the thickness and type of deposited catalyst thin films. The required annealing temperature range, in general, is broad from around 300 to 900 °C.

As stated earlier, CNT deposition can be obtained by any of the three commonly employed processes, namely arc-discharge, laser ablation or the CVD technique. The carbon extraction process from the precursor depends on the deposition method used. Hence, the CNT growth temperature varies with the deposition method employed. Arc-discharge and laser ablation methods use graphite rods as a carbon source thus they need high source temperature to obtain carbon by evaporating the graphite rod with thermal energy. In the case of laser ablation,

the thermal energy is derived from photons. The CNT growth temperature in an arc-discharge method is around 1000 °C and for laser ablation is around 1200 °C. CVD methods use carbonaceous gas or liquid materials as carbon precursors. The energy for decomposition of carbon precursor material is less than that of graphite rods and hence temperature for CNT deposition by CVD methods can be lower. Thermal CVD uses only heat energy and PECVD uses both the thermal and plasma energy to obtain carbon atom from its precursor. This difference in energy source can permit CNT deposition at different temperatures. In addition to carbon extraction from precursor, energy is needed for moving carbon atoms to appropriate lattice location to form CNT structure. The CNT growth temperature for thermal CVD method is broad from 500 to 900 °C. The potential energy of a CNT is inversely proportional to the square of the CNT radius. Thus SWCNT deposition needs higher temperature than MWCNT to obtain higher energy carbon atoms during deposition [26]. PECVD methods can synthesize CNTs at temperatures as low as 250 °C. In addition, choice of suitable catalyst materials permits temperature reduction.

2.2 Catalysts

When CNT was first discovered, a catalyst was not used in its formation. MWCNTs were first obtained with an arc discharge method. Use of catalyst was subsequently introduced to obtain SWCNT deposition with both arc-discharge [15] and laser ablation methods [27]. These latter two techniques employed graphite rods that contained catalyst material. When this catalyst embedded target graphite rod is evaporated, catalyst molecules are simultaneously present with carbon in the gas phase. The role of a catalyst is important in CNT growth. There are two categories of catalysts, namely the main catalyst and a co-catalyst. The main catalyst is a material such as iron, cobalt, nickel and molybdenum while a co-catalyst is a material such as

aluminum, niobium, titanium or iridium. Main catalyst can deposit CNT by itself. A co-catalyst cannot deposit CNT by itself. However, a co-catalyst is used for a specific role such as achieving a higher CNT yield, improvement in SWCNT yield, decreasing CNT deposition temperature or reducing defects. Yoon et al. compared cobalt and cobalt-molybdenum for MWCNT deposition and found that use of only Co reduces defects in the grown CNT compared to a Co-Mo catalyst [28]. Cantoro et al. used aluminum as a co-catalyst with different main catalysts, iron, nickel, and cobalt, and observed that Al can improve SWCNT yield [29]. Delzeit et al. used iridium, aluminum, niobium and titanium as a co-catalyst with iron. They found that both Ir and Al improved SWCNT yield and that Al was more effective than Ir. However, they found that Nb and Ti were not helpful as co-catalyst with iron [30].

When the catalyst is prepared properly for CNT growth, the carbon containing species from gas phase will be adsorbed on the surface of the catalyst. The former subsequently decomposes and carbon atoms begin to saturate the catalyst. CNT can be grown after the catalyst is saturated by carbon. This is a generally accepted mechanism for CNT growth utilizing a catalyst. This mechanism is called vapor-liquid-solid growth mechanism [31].

2.3 Catalyst Preparation Methods

In general, catalyst preparation involves two steps. The first step is to obtain nanoparticles of the catalyst and the second step is to activate the catalyst for CNT deposition. Ermakova et al. tried to deposit CNT with bulk iron as a catalyst and concluded that bulk iron did not perform as a catalyst for CNT deposition [32] and that one needs catalyst nanoparticles for CNT growth. There are several methods to produce catalyst nanoparticles. Pan et al. used sol-gel method for making iron nanoparticles [33]. Venegoni et al. used impregnation method [34]. Ago et al. used reverse micelle method [35]. Wang et al. used magnetron sputtering method [36].

The chemical treatment methods, such as sol-gel, impregnation, reverse micelle etc., form nanoparticles directly but involve time consuming and relatively complex processes. Physical methods, such as sputtering, electron beam deposition etc., deposit thin film layers of the catalyst. These methods need an annealing step to obtain nanoparticles from the deposited thin film. The physical methods are usually faster and simpler than chemical methods. Heat energy is supplied to thin films to obtain nanoparticles. The rate of substrate temperature increase during annealing decides mechanism responsible for conversion of catalyst thin film to nanoparticles. When the temperature is rapidly increased e.g. at a rate of 320 °C/min., explosive reaction can occur between Al and Ni thin film overlying layers present to form the catalyst. If the rate of increase in temperature is slow e.g. 40 °C/min., nanoparticles are obtained by the annealing process [37]. Explosive reaction can occur when the amount of emitted heat by atomic mixing is higher than the heat removed by thermal diffusion [38]. Both above rate dependent processes allow transformation of thin film layers to nanoparticles, but the size of nanoparticle in each case is different. Ma et al. obtained nanoparticles from 10 nm thick Al and 20 nm thick Ni layers with the above two approaches. They found nanoparticle size of approximately 40 nm upon gradual annealing to be much smaller than that of 200 nm size nanoparticles obtained at a higher anneal rate from an explosive reaction [38]. The thickness of the catalyst film is also an important factor for CNT deposition, because it is also responsible for deciding the size of catalyst nanoparticles formed and hence the diameter of the grown CNT [39–40].

2.4 CNT Growth Mechanisms

There are many hypotheses for CNT growth mechanisms and it is currently not clear which one is the dominant growth mechanism. However, researchers consider the basic model of CNT growth mechanism to be similar to the mechanism of carbon filament formation process.

Tenser et al. made carbon fibers with acetylene and mentioned role of hydrogen for catalyst activation and growing carbon fiber from a nanoparticle surface [41]. Baker et al. observed the formation of carbon nanofibers with electron microscopy in real time [42]. They suggest the following steps for carbon fiber deposition. The carbonaceous precursors are adsorbed and subsequently decomposed on the surface of the catalyst. The decomposed carbon atoms diffuse through the catalyst and saturate it. The carbon begins to precipitate after saturation. There are two types of subsequent growth modes. One is tip-type growth mode. Here, the catalyst locates on the top of the growing nanofiber. The other is called the base-type growth, where the catalyst locates on the bottom of the nanofiber. The actual growth mode is decided by interaction between the catalyst and the substrate surface [43]. If the interaction between the catalyst and the surface is strong, the catalyst locates on the bottom of the fiber resulting in the base growth mechanism. If the interaction between the catalyst and the surface is not strong enough, the catalyst locates on the top of the growing fiber resulting in the tip growth mechanism. The tip and bottom growth mechanisms depend on other CNT deposition parameters as well. Melechko et al. experimented with PECVD method under identical catalyst and substrate conditions and observed that tip or base-type growth can be controlled by manipulating the ratio of acetylene to ammonia gas in the deposition ambient [44].

The driving force behind carbon diffusion through the catalyst is still under debate. The carbon diffusion process can be due to bulk diffusion and/or surface diffusion [45]. Bulk diffusion driving force can result from temperature gradient [42, 46] or from carbon concentration gradient in the catalyst [47–48]. Helveg et al. suggest that the carbon does not need to diffuse inside the catalyst metal [45]. They experimented in situ with Ni as a catalyst and methane as the carbon precursor gas with a high-resolution transmission electron microscope

(HRTEM). They found that the Ni particles elongate first and a graphene layer was observed along the edge of the elongated Ni catalyst. They suggested surface diffusion of carbon along the edge of the nickel nanoparticle to be the mechanism for formation of carbon nanotubes [45]. Takagi et al. grew SWCNT with Au, Ag, Cu, Pt and Pd catalyst with thermal CVD methods [46]. Au has much smaller binding energy for carbon compared to conventional catalysts like Fe, Ni and Co. However, SWCNT can be grown with Au as a catalyst. They assumed that the carbon atoms precipitate and cover the conventional nanoparticle catalyst to make a hemispherical cap. This hemispherical cap has graphite structure and works as a precursor of SWCNT deposition. The catalyst nanoparticles play a role of a template for forming a hemispherical cap for further CNT growth.

2.5 Current Carbon Nanotube Deposition Methods

After discovery of carbon nanotubes (CNT) because of its unique electrical and mechanical properties, many methods were experimented with to deposit CNT. Of these, more commonly employed methods for CNT deposition can be classified as belonging to one of the following three main techniques: a) arc-discharge, b) laser ablation and c) chemical vapor deposition (CVD). Though each method may utilize a different mechanism, they all need to supply proper energy for carbon extraction from its precursor source and maintain suitable substrate condition for CNT growth. The choice of the CNT deposition method depends on the application. The three common methods to deposit CNT are briefly described below.

2.5.1 Arc-Discharge Method

Arc-discharge method uses two carbon rods as electrodes with plasma between the electrodes as shown in Fig. 2.1. The positive graphite rod (anode) works as a carbon source. Since carbon atoms are extracted from graphite, this method requires a higher deposition

temperature than other methods that use carbonaceous gases as a carbon source. The distance between the anode and the cathode is less than 1 mm, the voltage between electrodes is in the range of 20-25 V and the dc current is in the range of 50-120 A. The deposition chamber pressure is around 450 Torr in an inert Ar or He ambient. The CNTs are deposited on the negative electrode (cathode). The mass of the positive electrode keeps on decreasing during the CNT deposition. Iijima used this method and discovered MWCNTs [1] first, and subsequently two years later deposited SWCNT with this technique employing a transition metal as a catalyst [15]. Other researchers have also used a graphite anode containing transition metals as shown in Fig.2.2. This method permits growth of SWCNTs [49–50].

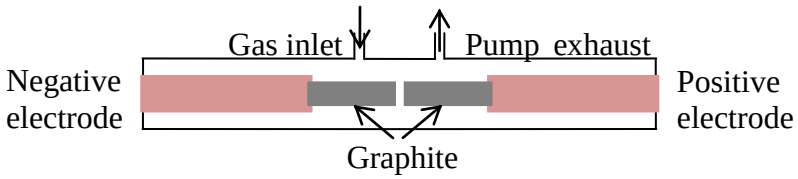

Figure 2.1. Schematic diagram of arc-discharge method for multiwall carbon nanotube deposition.

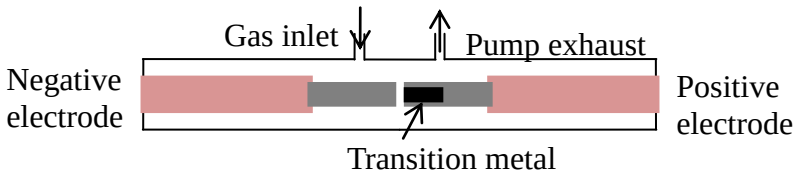

Figure 2.2. Schematic diagram of arc-discharge method for singlewall carbon nanotube deposition.

2.5.2 Laser Ablation Method

Laser ablation method uses photon energy to deposit carbon. When the laser hits a target comprising of graphite mixed with transition metal Ni-Co alloy, it creates gases containing carbon and transition metal. CNTs are formed immediately after the evaporation of target. The evaporated gases and CNT flow with inert gas such as Ar or N_2 and CNT is formed on the water-cooled copper at the end of the furnace as indicated in Fig. 2.3. In general, the SWCNTs which are synthesized by laser ablation method are metallic [2].

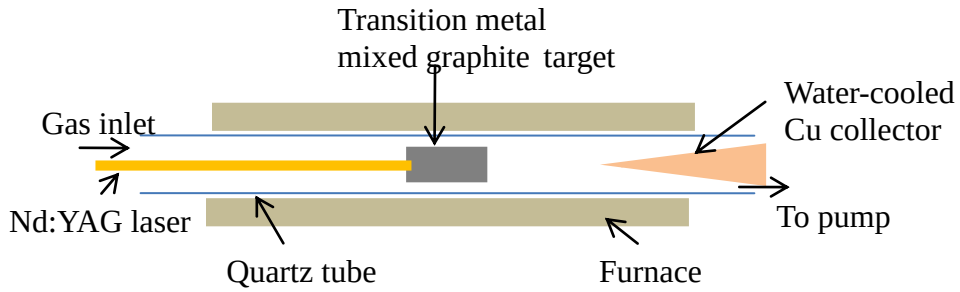

Figure 2.3. Schematic diagram of laser ablation method.

2.5.3 Chemical Vapor Deposition (CVD) Method

The CNT deposition process with CVD has certain advantages and flexibility in deposition temperature, pressure, and types of precursors and catalysts used. These factors affect both the quality and quantity of deposited CNTs. Many researchers prefer the CVD method to grow CNT because it is a relatively low temperature deposition process. The previous two methods, namely arc-discharge and laser ablation, use graphite as a carbon source requiring high temperatures and large amount of energy to extract carbon atoms. However, CVD method uses a carbon containing liquid or gas material such as hydrocarbons CH_4 and C_2H_2 as a carbon source

allowing for a relatively low temperature CNT deposition. There are various CVD methods and the most are based on thermal CVD or plasma enhanced CVD (PECVD) processes. The difference between these two CVD methods is the nature of the energy source for extracting carbon atoms. Carbon atoms are extracted from the precursor molecules by pyrolytic or thermal decomposition in a thermal CVD process while plasma energy is employed along with thermal energy in the PECVD process.

2.5.3.1 Thermal CVD

In general, thermal CVD uses hydrocarbons such as CH_4 or C_2H_2 as a carbon source because of relatively low values of energy required to decompose these molecules. These hydrocarbons are liquid or gas at room temperature. An inert gas such as Ar or N_2 is used along with the precursor gas to maintain the deposition chamber pressure. The hydrocarbon gases either decompose pyrolytically in the gas phase or on the surface of the catalyst. Carbon atoms saturate the transition metal catalyst nanoparticle such as Fe, Ni or Co on the substrate. These saturated carbon atoms diffuse through metal and form carbon nanotubes [51]. Figure 2.4 is a schematic diagram of the thermal CVD method. There are two types of CNT growth mechanisms namely the tip-growth mode and the base-growth mode. These growth modes have been discussed in section 2.4. In general, SWCNT grown by thermal CVD has a tendency for the tip-growth mechanism, while MWCNT deposited by PECVD has a tendency for the base-growth mechanism. Both mechanisms are observed in the MWCNT grown by a thermal CVD process [52].

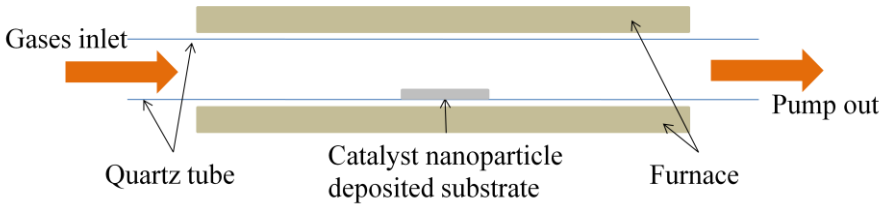

Figure 2.4. Schematic diagram of thermal CVD method.

2.5.3.2 Plasma Enhanced CVD

PECVD uses plasma energy for decomposition of carbon species. Many types of plasma sources have been tried for CNT growth including dc, rf, microwave, and rf with a magnetic field [53–56]. PECVD uses various power levels in the range of 10 W - 500 W and a negative bias voltage of magnitudes greater than 300 V. One of the big differences between PECVD and thermal CVD is the deposition temperature. When precursor is introduced inside the chamber, in a thermal CVD process, the precursor or its fragments attach to the catalyst on the substrate and carbon is extracted by thermal energy. However, precursors can be decomposed by the plasma energy in a PECVD and the extracted carbon is deposited on the catalyst on the substrate [3]. Figure 2.5 is a schematic diagram of PECVD method. This difference allows for lower substrate temperature deposition with PECVD and makes it a good technique for low temperature CNT growth. However, PECVD has three critical drawbacks. First, there is substrate damage during deposition due to ion bombardment. Second, there are difficulties associated with preparation of catalyst nanoparticles for CNT deposition. Chemical treatment method is used in PECVD to form catalyst nanoparticles because substrate temperature is usually not high enough to anneal in-situ physically deposited thin films to form nanoparticles. Chemical treatment methods are time consuming and are complex. Third, the deposited CNT by PECVD technique results are mostly MWCNT. Deposition of SWCNT by PECVD is still a challenging task. First drawback

can be solved by using remotely located PECVD [57]. SWCNT has been deposited by PECVD but at a growth temperature of 550 °C or higher [58–59].

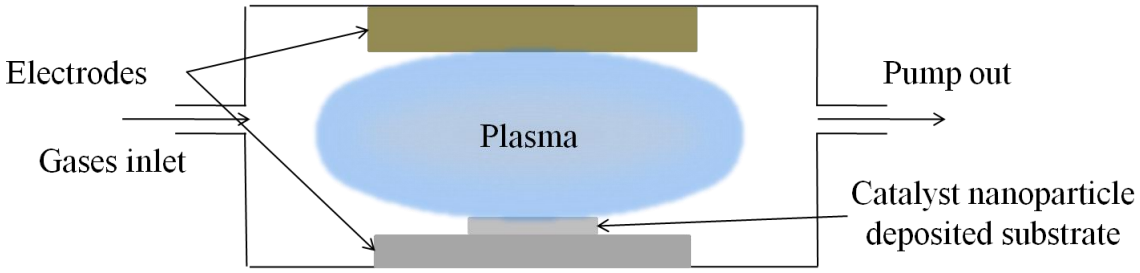

Figure 2.5. Schematic diagram of PECVD method.

2.6 Hexagonal Diamond Synthesis Methods

Hexagonal diamond is known as lonsdaleite, which is a rare formation among carbon structures. In general, hexagonal diamond synthesis method can be classified as a physical method or as a chemical method. Physical method implies solid-to-solid phase transformation. This method changes graphite or cubic diamond to hexagonal diamond by applying high pressure and high temperature (HPHT). Hexagonal diamond can be obtained by applying high pressure to graphite without high temperature but the hexagonal diamond phase reverses to graphite when the pressure is released. Bundy *et al*. used static compression method. They used over 130 kbar of pressure and over 1000 ˚C temperature [5]. He *et al.* used shock wave compression method to transform from cubic diamond to hexagonal diamond directly. The shock duration and pressure were 1 ns and 80 GPa respectively [7]. Chemical methods for hexagonal diamond deposition generally utilize similar deposition system and process as for cubic diamond deposition. Amornkitbamrung *et al.* used microwave plasma PECVD. Scratched steel is utilized

as a substrate. The experimental temperature was 450 ~ 500 ˚C and the pressure 100 ~ 107 Pa. The negative biases of substrate utilized were 0, -70, -150 and -190 V. The deposition time was 30 minutes [9]. Misra *et al.* used a hot filament CVD method shown in Fig. 2.6. They used CH_4 as a carbon source. The substrate temperature and pressure were 800 ˚C and 2.66 kPa respectively. They used h-GaN film deposited on quartz as a substrate. The deposition time was 5 hours [10].

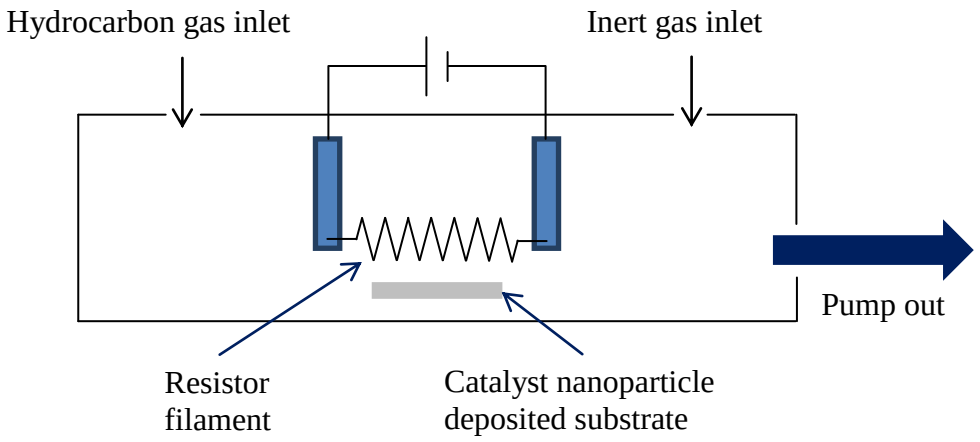

Figure 2.6. Schematic diagram of hot filament CVD method.

2.7 Chapter Summary

The experimental methods of previous CNT and hexagonal diamond deposition are presented in this chapter. Conditions for CNT deposition by these methods are also mentioned. The type, role and preparation methods for catalyst for CNT deposition are described. The hexagonal diamond synthesis methods are mentioned. However, there is limited information in literature for hexagonal diamond deposition utilizing CVD.

CHAPTER 3. PHOTO-ENHANCED CVD SYSTEM

3.1. Background of Photo-enhanced CVD

Photo-enhanced CVD was invented in 1960s to deposit elemental and compound semiconducting thin films by using photochemical processes [60]. In conventional CVD, the growth temperature is an important factor because molecular reactants must dissociate thermally. However, a high process temperature has certain disadvantages associated with impurity diffusion and dopant redistribution within a semiconducting substrate. Also, it limits the type of substrate that can be used for deposition. The PECVD process reduces some of these problems associated with high temperature by permitting a lower growth temperature. However, a PECVD process exposes the substrate to potential plasma damage from high energy ion bombardment. Photo-enhanced CVD can be an alternative method to reduce substrate deposition temperature. Photo-enhanced CVD uses photolysis in conjunction with or without pyrolysis to dissociate precursor molecules. When incident light is absorbed by the gas phase molecules, the photon energy can break the bonds of the gas phase molecules. The absorption cross section and quantum yield are critical factors for photolysis. The absorbed light is proportional to the absorption cross section and the quantum yield gives the probability of precursor decomposition by an absorbed photon. Use of a photo-sensitizer can absorb more photon energy than the actual precursor molecule used and then subsequently transfer the absorbed light energy to the precursor molecules. The light, which is absorbed by the sensitizer molecule can excite vibration modes and subsequent collisions with the precursor molecules can then result in energy transfer to the precursor molecules. Mercury is a well-known sensitizer for photo-enhanced CVD partly because mercury lamps are an inexpensive source for UV light. Various films have been deposited using Hg sensitizers. For example, Irvine *et al.* deposited HgTe film [61], Rathi *et al.*

grew silicon nitride (Si_3N_4) films [62], and Mukhopadhyay et al. deposited hydrogenated amorphous silicon oxygen (a-SiO_x:H) films [63]. There are different ways by which incident light energy can assist in a CVD process. It could directly fragment or excite the reactant molecules through photon absorption resulting in photolysis. Another mechanism is when the incident light is absorbed by the substrate. The photon energy in the latter case increases substrate surface temperature, which assists in decomposing the gas phase reactant molecules on the substrate surface. In general, these processes allow photo-enhanced CVD to deposit thin films at lower bulk substrate temperature. In addition, photo-enhanced CVD permits selective area deposition and unlike plasma-enhanced CVD, it is not accompanied by damage resulting from ion-bombardment of the substrate. Photo-enhanced CVD can employ a coherent laser light source or an incoherent lamp light source.

Bondi *et al.* have grown CNT by laser chemical vapor deposition (LCVD) method under 150 Torr by using a 100 W CO_2 laser as a light source at 10.6 μm wavelength. They used 1 mm thick graphite as a substrate and acetylene as a precursor [64]. The process can deposit CNT on a selective area on the substrate. However, CNT was deposited at a relatively high substrate temperature. They used a thermal imaging camera to measure the growing temperature for which the minimum detectable temperature of the system was 1200 K. Thus CNT deposition temperature of substrate was higher than 1200 K. The CNT deposition with laser CVD is relatively more difficult for a large area substrate as it involves scanning time for the laser beam spot.

Ehrlich *et al.* used 257.2 nm wavelength pulsed Ar^+ laser for deposition of a variety of elements by photo-CVD [65]. They depositied Sn, Al, Zn, Ga, and Ge with $Sn(CH_3)_4$, $SnCl_4$,

$Al(CH_3)_3$, $Zn(CH_3)_2$, $Ga(CH_3)_3$ and $Ge(CH_3)_4$ as precursor gases respectively. They also obtained Fresnel ring pattern deposition of cadmium.

Bauerle *et al.* used 488 nm wavelength of Ar^+ laser for Si deposition from SiH_4 precursor [66]. They obtained 5 μm wide amorphous silicon deposition by scanning the substrate perpendicular to the beam. The size of deposition chamber was about 700 cm^3 and pressure of deposition process was 99 Torr. They used laser power density varying from 300 to 3600 W/mm^2 to obtain different substrate deposition temperature from 1200 K to 1700 K.

Kawate *et al.* deposited amorphous carbon films by photo dissociation of C_2H_3Cl and CCl_4 precursors on crystalline silicon, glass and stainless steel platelet substrates utilizing a pulsed ArF excimer laser at 193 nm wavelength at various substrate temperatures ranging from 200 to 400 °C, flow rate of reagent gases from 5 to 80 sccm, chamber pressure from 0.05 to 5 Torr and deposition time from 30 min to 3 hours [67].

Fowler *et al.* deposited homoexpitaxial Si films from Si_2H_6 also using 193 nm ArF excimer laser beam parallel to the substrate by utilizing photolysis mechanism. The deposition temperature of substrate was 250 to 350 °C, total experimental pressure (He + Si_2H_6) was 600 mTorr and Si_2H_6 partial pressure was 5 - 40 mTorr [68].

Chen *et al.* utilized photo-enhanced CVD method for hydrogen passivation to improve photoluminescence intensity in Si doped GaAs, undoped GaAs and AlGaAs. They used a low-pressure Hg lamp as an ultraviolet light source and Hg as a photosensitizer [69]. The experimental conditions were 40 - 50 sccm hydrogen flow rate, 0.75 - 1.5 Torr chamber pressure, 250 - 350 substrate temperature and 3 - 4 hours exposure time.

Rathi *et al.* deposited silicon nitride film on a silicon wafer utilizing NH_3 and SiH_4 gases. They used Hg sensitized photo-enhanced CVD method utilizing a Hg lamp. They deposited

films at various substrate temperatures ranging from 100 to 400 °C, reactant gas ratio SiH_4/NH_3 from 0.01 to 0.06 and chamber pressure from 0.4 to 1.4 Torr [62].

Norton and Ajmera employed photochemical vapor deposition technique to deposit GaAs on synthetic fused silica. They utilized Hg-Xe arc lamp as a light source and AsH_3, H_2 and $Ga(C_2H_5)_3$ as precursors. The N_2 is employed as a carrier gas. The deposition conditions were 62 sccm 10 % AsH_3 in H_2 mixture flow rate, 5 sccm flow rate of N_2 through $Ga(C_2H_5)_3$ bubbler, less than 240 ˚C substrate temperature and 60 minute deposition time [12].

Sahu *et al.* deposited silicon oxide and silicon nitride double layer films. They also used Hg sensitized photo-enhanced CVD method utilizing mercury lamp as a light source. The conditions for silicon dioxide deposition included two different substrate temperatures of 250 and 300 °C; 600 mTorr chamber pressure and Si_2H_6/N_2O flow ratio of 0.04. The conditions of silicon nitride deposition were 250 °C substrate temperature, 860 mTorr chamber pressure and Si_2H_6/NH_3 flow ratio of 0.034 [70].

Chiou *et al.* deposited SiO_2 on AlGaN. They used deuterium lamp with output in 140 - 700 nm wavelength range. They deposited at various substrate temperature values in 100 - 300 °C range and at 0.9 Torr pressure [71].

Rohmund *et al.* used CO_2 laser at 10.5 μm wavelength for MWCNT deposition. The substrate temperature was controlled by changing laser power. The deposition temperature was between 770 and 860 °C, the pressure was 150 Torr and the laser power was between 42 and 46 W. They used a mixture of acetylene (C_2H_2) and ethylene (C_2H_4) gases as carbon source [72].

Alexandrescus *et al.* experimented with CO_2 laser at 10.6 μm wavelength to deposit CNT on a silicon substrate with a mixture of ethylene (C_2H_4) and acetylene (C_2H_2) ambient gases. The ethylene gas is used as a sensitizer and the acetylene supplies carbon. A 100 W CO_2 laser was

employed. The CNT deposition temperature was approximately 800 °C and chamber pressure was 150 Torr. They used both photolysis and pyrolysis mechanisms for CNT deposition [73].

There are many research results for thin film deposition with lamp assisted photo-enhanced CVD. However, to our knowledge, deposition of CNT or hexagonal diamond with lamp assisted photo-enhanced CVD has not been reported yet.

3.2. Experimental Setup

Photo-enhanced CVD system is similar to a traditional thermal CVD system except for the provision for introduction of a light source. Figure 3.1 is a schematic diagram of the photo-enhanced CVD system designed for CNT and hexagonal diamond deposition in our laboratory. The system consists of a growth chamber, gas flow system, a light source and a vacuum pump. The growth chamber has two gas inlets and one outlet for gas exhaust. The two gas inlets are for introducing ammonia and CCl_4/Ar gas mixture. The gas inlets and outlet are located at the top and bottom of the growth chamber respectively. This arrangement of gas inlets and outlet make gas flow parallel along the substrate surface. The exhausted gases pass through foreline trap and vacuum pump. They are burned before their release into the air.

The growth chamber has an optical window for allowing incident light to enter the chamber. The optical window is made of 1.875 inch diameter, 0.375 inch thick UV grade fused silica. The cylindrical graphite substrate holder contains a heater and a type-K thermocouple. The incident beam is normal to the sample surface. A pressure gauge is attached to the growth chamber. A feedthrough provides power to the heater and connection for the thermocouple wires. The detail specifications of each equipment and the setup are given below.

Figure 3.2 shows top (a) and side (b) views of the assembled photo-enhanced CVD system around the growth chamber, which comprises of a combined four-way cross and a six-

way cross fitting (from MDC). The locations of each equipment and connection are mentioned in this figure. The growth chamber is made of 304 grade stainless steel. Copper rings are utilized as gaskets. The total internal volume of the growth chamber is approximately 0.5 liter without the substrate holder.

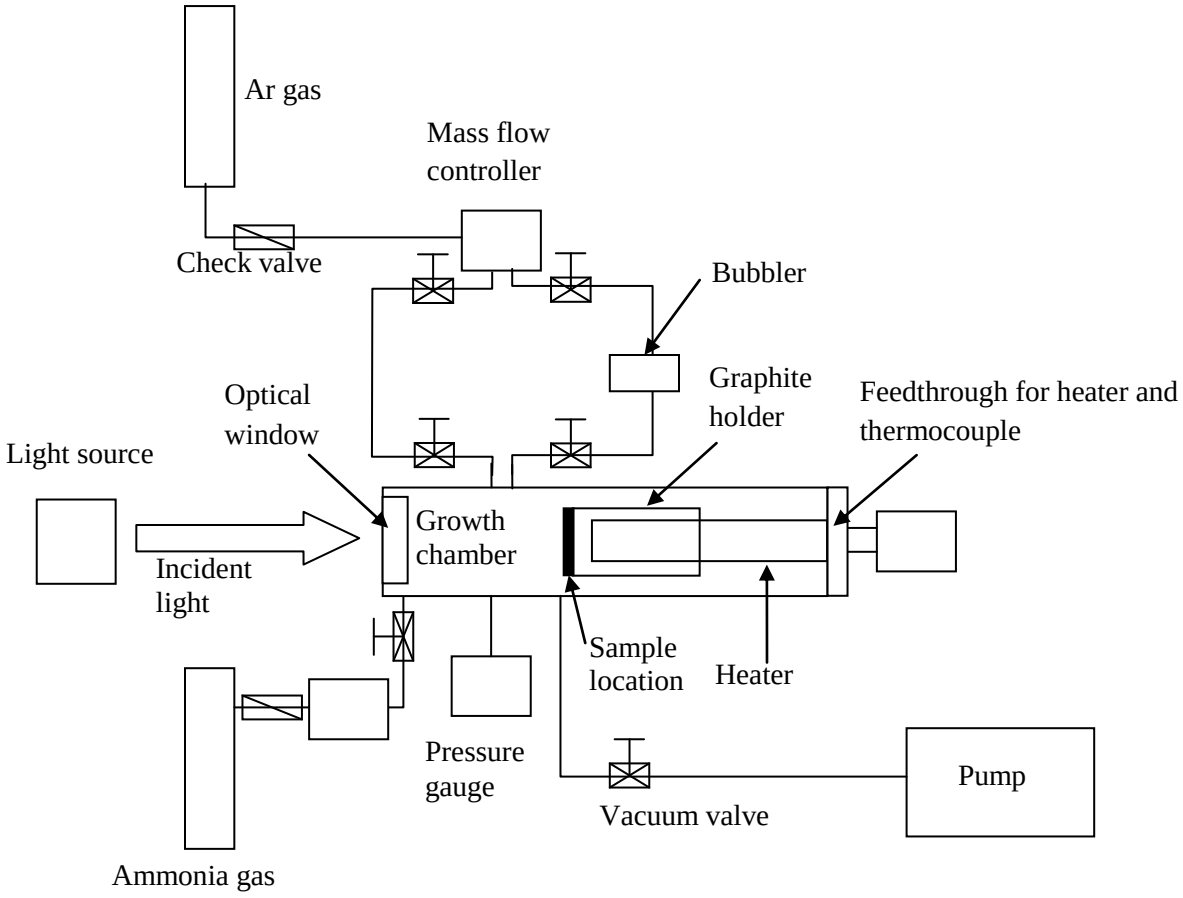

Figure 3.1. Schematic diagram of the designed photo-enhanced CVD system.

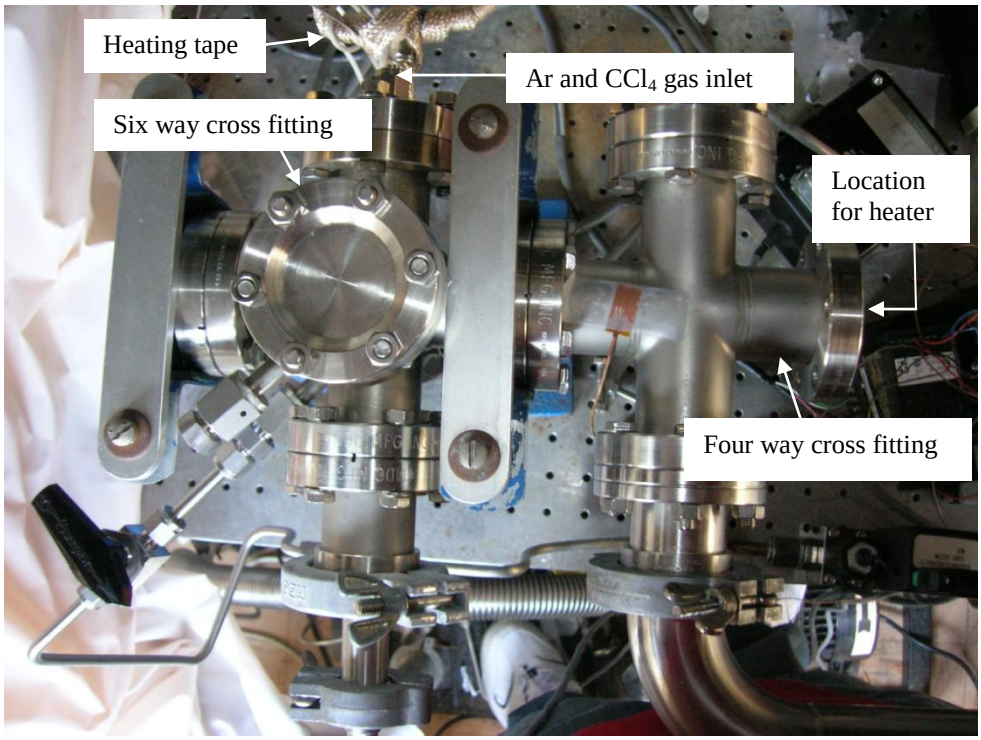

(a)

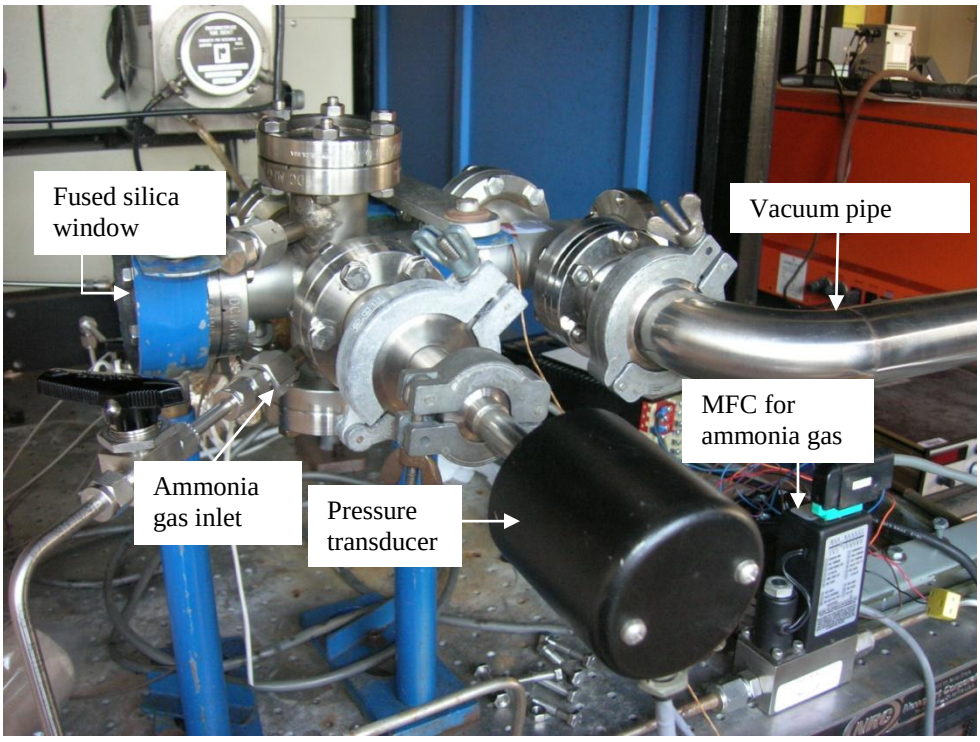

(b)

Figure 3.2. (a) Top view and (b) side view of the photo-enhanced CVD system.

Xe arc lamp (Hanovia 976 C) is used as a light source. It is housed in an Oriel 6140 housing with Newport 8540 power supply. The output of this lamp is in 200 - 2400 nm wavelength range. Figure 3.3 shows typical output from a 1000 Xe arc lamp (6269 1000 W Xe). Figure 3.4 represents the transmission as a function of the incident wavelength for the optical window provided by MDC. Figure 3.5 shows the measured transmission through the UV grade fused quartz window (from MDC) in the wavelength range from 190 to 500 nm utilizing a UV-visible spectrophotometer from Varian. The window has over 86% transparency for light with wavelengths between 200 and 2400 nm as expected.

Argon of 99.999% purity is used as the carrier gas in this work. The argon gas is present during deposition with the precursor gas. Hence, the absorption cross section of argon is an important factor in photo-enhanced CVD method. The absorption cross section of argon is zero for photon wavelength higher than 125 nm [74]. Thus absorption of photons by argon is negligible in this experiment. Carbon tetrachloride (CCl_4) from Acros Organics of 99% purity is used as the precursor. The CCl_4 molecule has a relatively high absorption cross section area and the details of precursor gas selection are given in section 4.2. Ammonia gas of 99.999% purity from Praxair of is used as the annealing ambient to assist nanoparticle formation from the catalyst thin films. Bubbler from Kimble-Knotes is used for obtaining CCl_4 vapors. Brooks 5878 series mass flowmeters and Brooks 5850 E series mass flow controllers (MFC) are used to control the flow of Ar and ammonia gases.

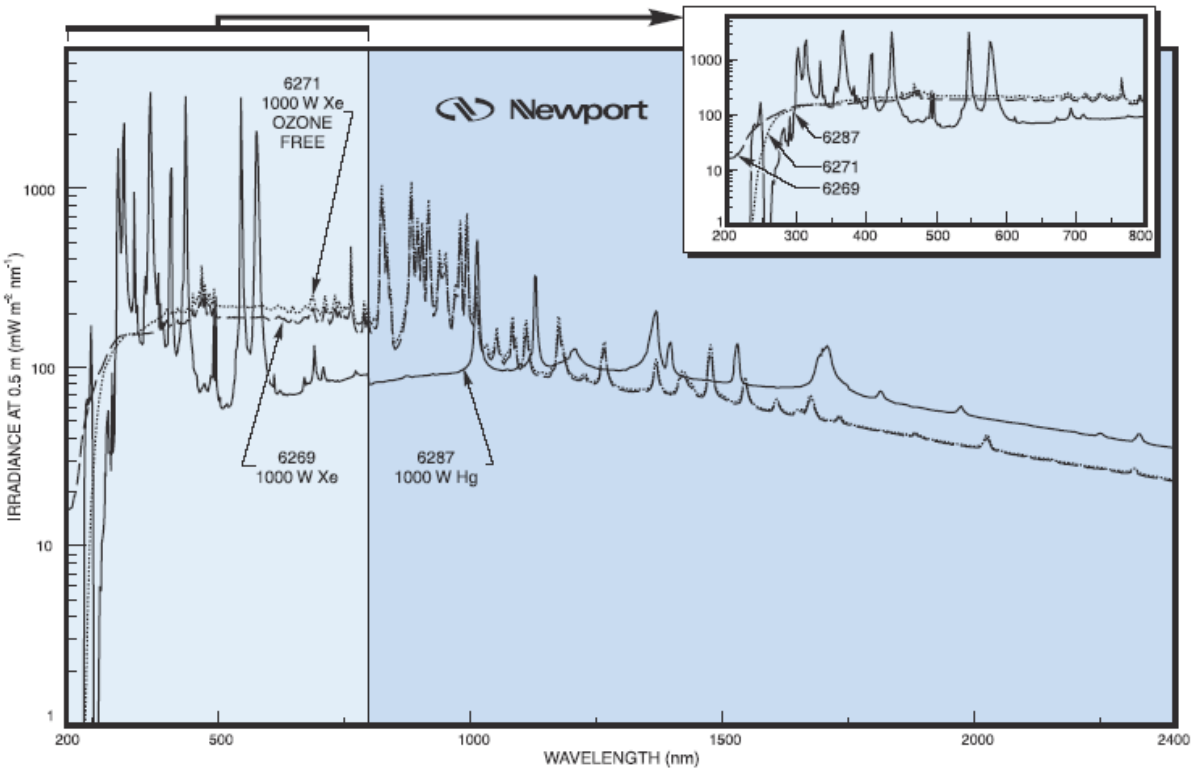

Figure 3.3. Spectral irradiance data for Xe arc lamp (6269 1000 W Xe).

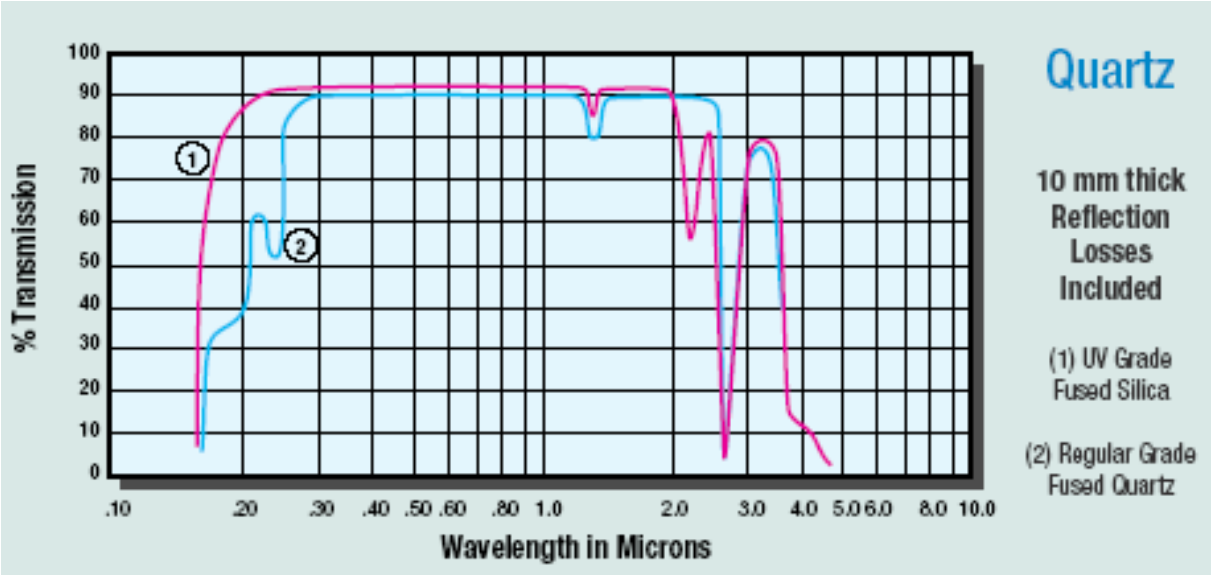

Figure 3.4. Transparency of the fused quartz optical window as a function of wavelength. UV grade fused silica is the one used in this work.

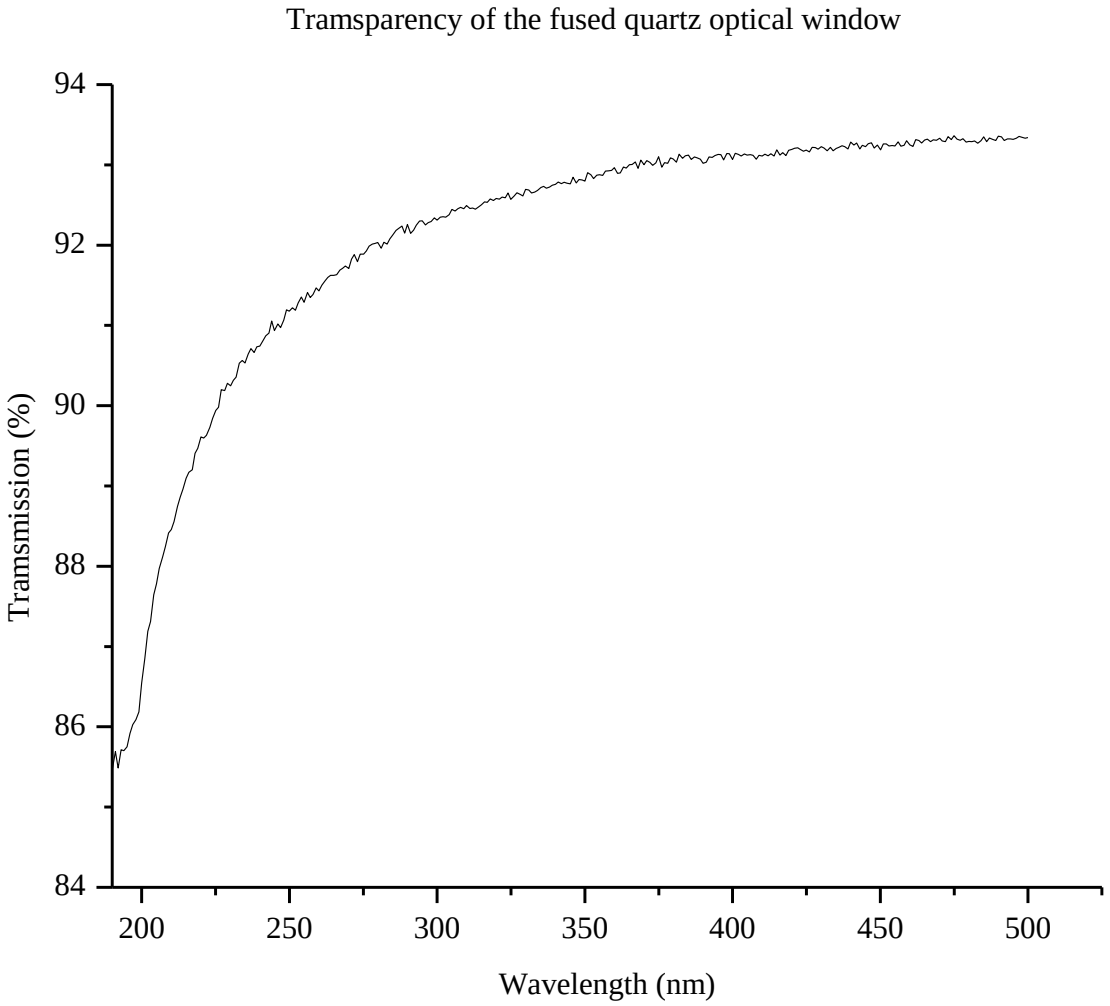

Figure 3.5. Measured transmission through the fused quartz optical window as a function of wavelength.

The substrate holder contains a heater (Firerod 9280) from Watlow, a graphite cover lid and a type K thermocouple. The temperature controller (PXR3) is from Fuji Electric Systems. The substrate heater has diameter of 0.375 in. The substrate holder is made of 1 in diameter graphite cylinder and the size of substrate sample is approximately 1cm × 0.5 cm for preliminary experiments. Ceramic bolts and washers are utilized to hold the sample to avoid contamination from metallic bolts and washers. Four different substrate samples can be loaded at a time on this

graphite substrate holder. This allows for comparison of results from different catalyst samples under the same annealing and deposition process. After the preliminary experiments, the substrate sample size is increased to approximately 1 in × 1 in for testing the feasibility of large area deposition. The thermocouple is inserted through a hole located through the side of the graphite holder and is located 0.2 cm from the top surface. Figure 3.6 shows dimensions and structure of graphite substrate holder and the heater. Figure 3.7 illustrates the graphite substrate holder and the fully assembled heater. The thermocouple connected to the temperature controller is placed into the graphite substrate holder, thus there exists a temperature difference between the surface temperature of the graphite substrate holder and that measured by the temperature controller. Table 3.1 shows the surface temperature at five different points on the graphite substrate holder with three specified temperature measured by the temperature controller. These points are marked in Fig. 3.6 (b).

CCl_4 is used in this work as a precursor for C. The process of CCl_4 phase change from liquid to gas is endothermic. The vapor pressure of CCl_4 as a function of temperature is shown in Fig 3.8. The boiling point of CCl_4 at atmospheric pressure is 76.72 °C. Heating tapes from Omega engineering were utilized for heating the feed-through lines from the bubbler to the chamber to prevent condensation of the precursor vapor.

An alcatel 2008 AC rotary mechanical pump is utilized at the exhaust to control the chamber pressure. A foreline trap is filled with activated alumina sorbent from PELCO and used to block the oil backflow from the mechanical rotary pump. A MKS Baratron (Type 221) pressure transducer is employed for chamber pressure measurement.

Table 3.1. Surface temperature measurement of graphite substrate holder in air ambient.

Temperature controller set point (°C)	Surface temperature at five different points on graphite substrate holder (°C)				
	1	2	3	4	5
400	371	382	385	384	378
425	384	401	402	399	386
450	414	421	423	419	413

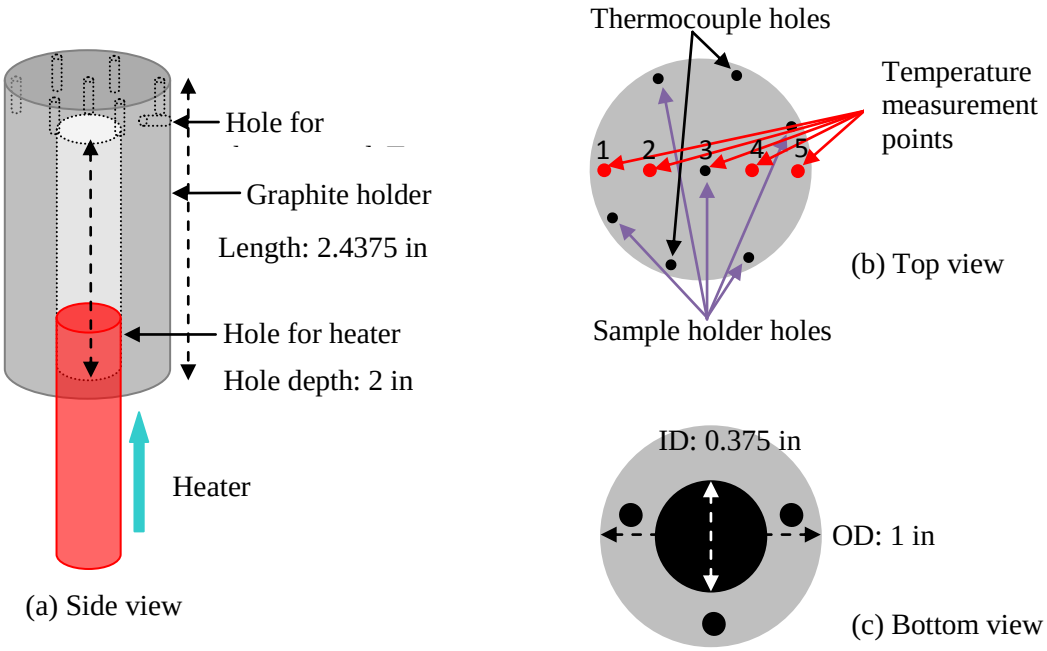

Figure 3.6. Dimensions and structure of heater and graphite substrate holder. (a) Side view, (b) top view and (c) bottom view.

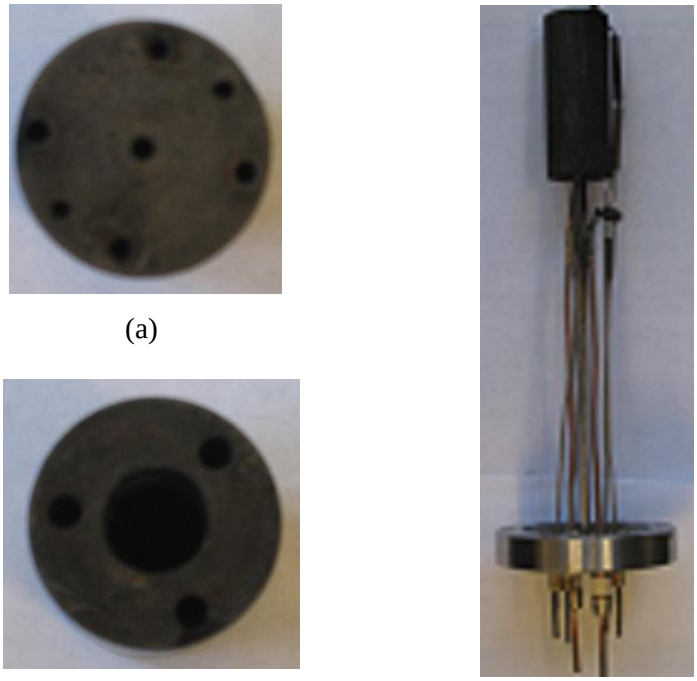

Figure 3.7. Pictures of graphite substrate holder. (a) top view, (b) bottom view and (c) assembled heater.

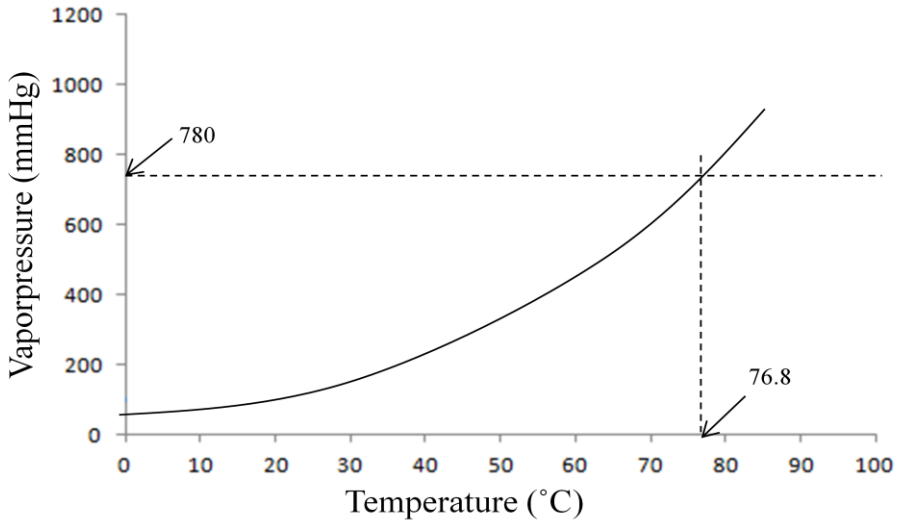

Figure 3.8. Temperature versus vapor pressure graph of carbon tetrachloride.

3.3 Chapter Summary

A review of literature and general concept behind photo-enhanced CVD are first described in this chapter. This background study of photo-enhanced CVD reveals various materials for possible deposition of carbon material at low temperature. The details of experimental setup, the roles of specific equipments and components with their characteristics are given in the latter part of this chapter.

CHAPTER 4. EXPERIMENTAL PROCEDURES

Before starting the experiment, suitable substrate preparation method and choice for proper gases have to be made. The substrate preparation of CNT is important because the size and condition of nanoparticles play a critical role in CNT deposition. However, there is limited information available on the effects of a substrate in hexagonal diamond deposition. Hence, substrate preparation is guided by information available on deposition of CNT. The substrate preparation involves annealing of the catalyst thin films deposited on the substrate sample. Ammonia gas is utilized for the annealing environment. Photo-enhanced chemical vapor deposition method is employed for this experiment. The photo-absorption coefficient plays an important role in this deposition technique. Carbon tetrachloride (CCl_4) is selected as a precursor for carbon source because CCl_4 has a larger absorption coefficient than most commonly available hydrocarbon precursors. After settling on a substrate preparation method and the selection of suitable gases, a suitable combination of growth parameters are investigated. Initially, through a set of preliminary experiments, proper conditions for annealing and for the deposition process are determined. These are latter utilized for CNT and hexagonal diamond deposition. The details are described in the following sections.

4.1 Thin Film Catalyst Preparation

Catalyst nanoparticle preparation is the first step for CNT deposition because catalyst nanoparticles permit extraction and nucleation of carbon atoms from the precursor for CNT growth. There are several methods for catalyst nanoparticle preparation such as sol-gel, impregnation, reverse micelle, sputtering and electron-beam thin film deposition [33–37]. Catalyst research for hexagonal diamond synthesis has not been thoroughly examined. Use of

thin films of h-GaN has been reported because of the similarity in structure with hexagonal diamond along with Ni, which is a more popular catalyst for hexagonal diamond synthesis [75], [76]. It is assumed here that preparation for CNT deposition should be also applicable for hexagonal diamond deposition. In this work, thin film deposition utilizing electron-beam evaporation followed by annealing of the catalyst thin film layers have been utilized for nanoparticle preparation. The technique is amenable to standard lithography for delineating areas for catalyst presence on the substrate.

Catalyst for CNT growth comprises of a main catalyst material such as nickel, iron, cobalt or molybdenum and is often accompanied by a co-catalyst material such as aluminum, niobium, titanium or iridium. The main catalyst material is the one responsible for CNT deposition [31]. The co-catalyst material is not capable of depositing CNT by itself. However, the role of a co-catalyst varies and includes factors such as CNT yield enhancement, convenience in substrate processing, improvement in SWCNT yield or lowering of CNT deposition temperature [31]. The deposited catalyst thin film layer thickness plays a critical role in CNT deposition. The thin film layer thickness controls the size of the resulting catalyst nanoparticles on the substrate after annealing, which in turn is responsible for the diameter of the CNTs being deposited. If the size of catalyst nanoparticle is too large, CNTs cannot be observed. If Al containing nanoparticle is enclosed by amorphous carbon, the interface between Al and amorphous carbon transforms to an onion like fullerene. This means that the size of catalyst nanoparticle determines the size of the fullerene. If the size of a fullerene is increased, nano-diamond structure is more stable than that of the fullerene of a larger size. In general, nano-diamond is a stable carbon material when the number of carbon atoms is between 1,100 and 25,000. Fullerene is more stable carbon material than nano-diamond, when the number of carbon

atom is lower than 1,100 [77]. Thus it is important to accurately measure and control the deposited metal catalyst layer thicknesses.

The catalyst metal layer sandwich is deposited on thermally oxidized silicon substrates by an electron beam evaporation process utilizing Temescal BJD 1800 evaporator. The evaporated film thickness during deposition is controlled by an *in situ* crystal thickness monitor. Each deposited film thickness is measured with an AFM accurately and the crystal monitor is calibrated with the help of these AFM measurements. A three-layer Al/Ni/Al sandwich structure comprising of Al top and bottom layers and a middle Ni layer is used in this work as a catalyst. The bottom Al layer assists with the formation of nanoparticles on the substrate surface from an otherwise continuous initial film during the annealing cycle and also prevents sintering of the catalyst Ni during annealing [30]. The top Al layer protects the main catalyst Ni from oxidation during sample transfer process from the electron beam deposition chamber to the CNT or the hexagonal diamond deposition chamber [29].

Four different combinations of catalyst sandwich layer thicknesses are investigated for preliminary results in this work as indicated in Table 4.1. The thickness of the mid-layer comprising of Ni is kept constant equal to 1 nm for these four cases but the thicknesses of the top and the bottom Al layers is varied from 1 nm to 10 nm as indicated in Table 4.1. Sample size for this preliminary experiment is approximately 1 cm × 0.5 cm. Four prepared sample substrates representing these four different combinations are located adjoining each other in a rectangular pattern on the heated substrate holder during an experiment run. Thus results on these four substrate samples can be compared by exposing them to identical experimental conditions to help decide which sample gives an optimal result for our case.

Table 4.1. Al/Ni/Al catalyst sandwich layer film thicknesses utilized for nanoparticle formation.

Combination	Top layer Al thickness (nm)	Mid-layer Ni thickness (nm)	Bottom layer Al thickness (nm)
# 1	1 nm	1 nm	1 nm
# 2	3 nm	1 nm	3 nm
# 3	5 nm	1 nm	5 nm
# 4	10 nm	1 nm	10 nm

4.2 Gas Precursor Selection

Various carbon containing gases, liquids and solid materials have been used as precursors for CNT and hexagonal diamond deposition. Solid carbon containing materials such as graphite and graphite containing catalysts are used as a source for carbon in arc discharge or laser ablation deposition. High energy is necessary to extract carbon atoms from a solid carbon containing material thus processing temperature for these methods tend to be high. The binding energy of graphite is 7.4 eV/atom [14]. Hexagonal diamond is synthesized by a physical method utilizing a solid carbon material. When appropriate high pressure and high temperature are applied to hexagonal graphite or cubic diamond, the structure transforms to that of hexagonal diamond.

Liquid or gas materials containing carbon, especially hydrocarbons, have been frequently used as precursors for CNT deposition employing CVD method as they can be decomposed at relatively lower energies. This is advantageous in that it may permit CNT and hexagonal diamond deposition at lower processing temperatures.

Few researchers report hexagonal diamond deposition with CVD method and methane is mentioned as a precursor. However, various carbonaceous gases are reported to deposit CNT. The hydrocarbons and carbon compounds such as carbon monoxide [78] and carbon

tetrachloride [79] are used as a carbon source in CNT growth by CVD technique. Many researchers have used hydrocarbon gas or liquid materials such as acetylene (C_2H_2) [80], methane (CH_4) [81], ethane (C_2H_6) [82] and ethylene (C_2H_4) [83]. Acetylene is one of the common carbon sources for CVD method to deposit CNT because of its low decomposition energy.

In this work, photo-enhanced CVD method is employed for CNT and hexagonal diamond deposition. A light source is utilized to assist decomposition of the precursor gas molecules. The choice of a precursor material for photo-enhanced CVD method depends on its absorption cross section at the incident light wavelengths. A Xe arc lamp is used as a light source in this work. Its light output as a function of wavelength is given in section 3.2. This broad light source output lies within the wavelength range from 200 nm to 2400 nm. In general, the absorption cross section areas of hydrocarbons are very small in the 200 - 2400 nm wavelength range.

Schoen examined absorption cross section of various hydrocarbons [84]. Figure 4.1 shows the absorption cross section of acetylene as a function of wavelength. The cross section area peaks near 78 nm wavelength and dramatically reduces for wavelength longer than 90 nm. Souza and Srivastava reported absorption cross section of C_2H_2 in the range of 12.5 to 250 nm wavelength [74]. The result shows the cross section has maximum value of 46.3 megabarn at 77.5 nm wavelength and second peak of 34.8 megabarn at 124.1 nm wavelength. The absorption cross section decrease dramatically after 124.1 nm wavelength and become almost zero at over 150 nm wavelength.

Figure 4.2 shows the absorption cross section area of ethylene. The cross section area reduces rapidly at wavelengths greater than about 100 nm [84]. The relationship between the

absorption coefficient α (cm^{-1}) and the absorption cross section area σ (cm^2) is given by $\alpha = \sigma N$, where N is the concentration of gas molecules of per unit volume.

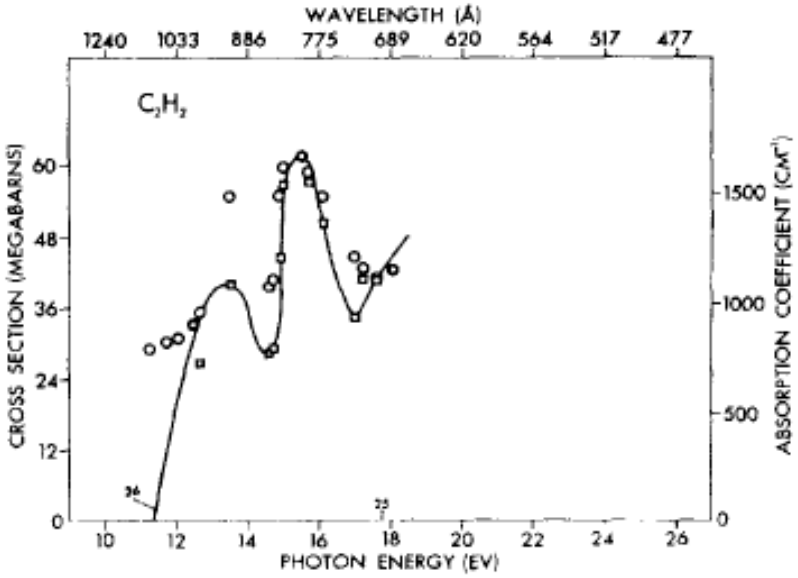

Figure 4.1. Absorption cross section area of acetylene as a function of wavelength. Barn is 10^{-24} cm^2. After reference [84].

.

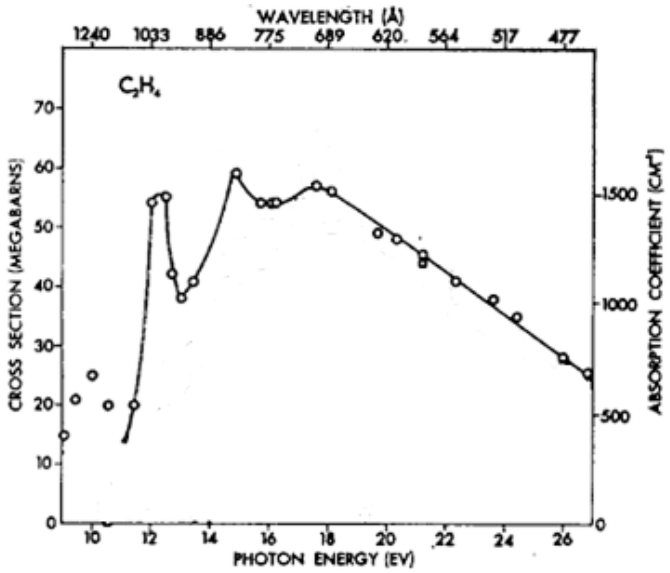

Figure 4.2. Absorption cross section area of ethylene according to wavelength. Barn is 10^{-24} cm^2. After reference [84].

Chen and Wu experimentally measured absorption cross section areas of several hydrocarbon materials [85]. Figure 4.3 shows absorption cross section area for methane. It has a maximum cross section value at approximately 127 nm and reduces rapidly beyond 130 nm. When the temperature increases, the cross section area also increases, however there is no significant difference between 150 and 370 K.

Figure 4.4 shows absorption cross section area for ethane molecule as a function of wavelength for three different temperatures. Ethane cross section does not critically depend on temperature but decreases for wavelengths greater than approximately 135 nm.

Figure 4.5 shows absorption cross section of carbon monoxide [86]. It has sharp peaks at 107 and 108 nm and very weak absorption at wavelengths longer than 160 nm.

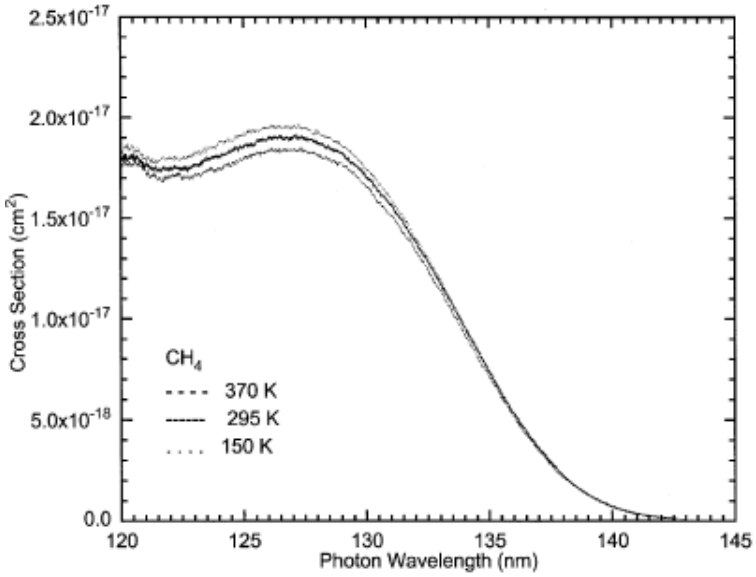

Figure 4.3. Absorption cross section area of methane as a function of temperature and wavelength. After reference [85].

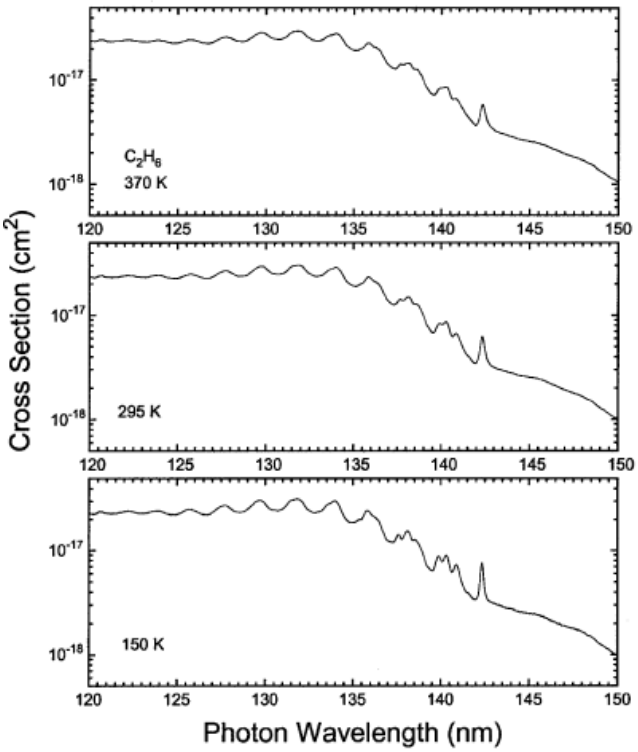

Figure 4.4. Absorption cross section area of ethane as a function of wavelength for three different temperatures. After reference [85].

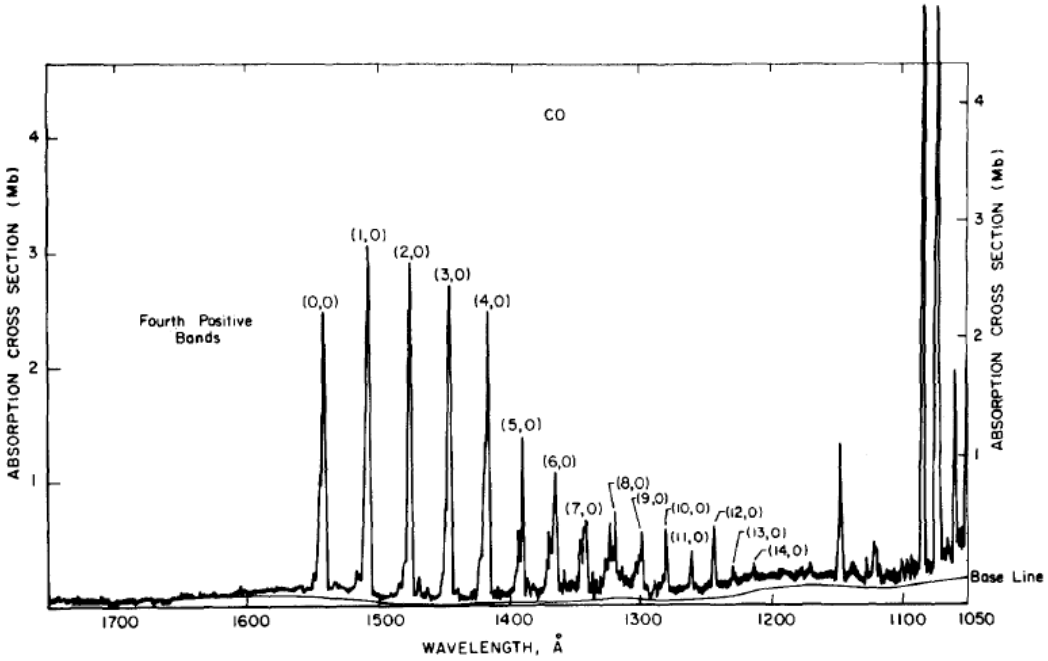

Figure 4.5. Absorption cross section area of carbon monoxide as a function of wavelength. After reference [86]. 1Mb = 10^{-18} cm^2.

Figure 4.6 shows the cross section of carbon tetrachloride [87]. It has a high value at short wavelengths (186 nm) and reduces at longer wavelengths. However, the decreasing of cross section is not as steep as seen for hydrocarbons. The cross section of carbon tetrachloride has absorption cross section values of 8×10^{-19} cm^2 at 200 nm and approximately 10^{-20} cm^2 at 240 nm. The cross section increases slightly with temperature but is not very sensitive to temperature variation in the range 220 - 300 K.

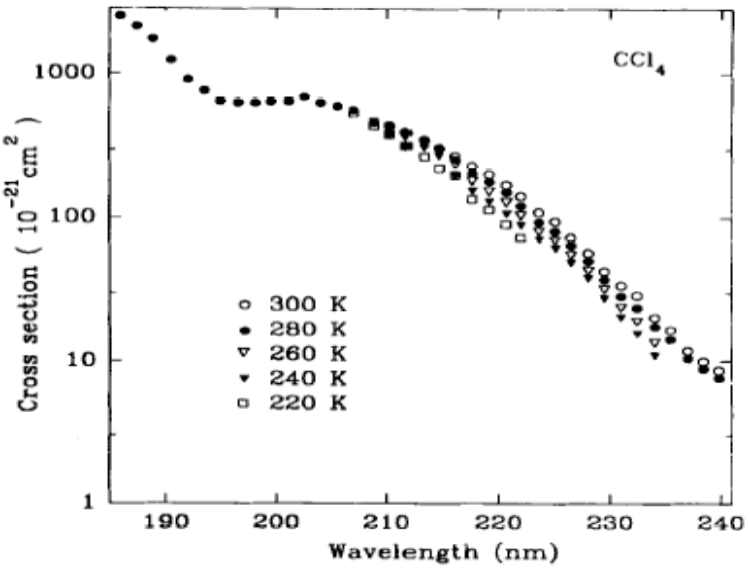

Figure 4.6. Absorption cross section area of carbon tetrachloride as a function of wavelength and temperature [87].

From these various photo-absorption cross-section considerations, it is seen that carbon tetrachloride has the largest cross section among various carbonaceous materials examined for CNT deposition with our light source in the wavelengths between 200 and 2400 nm. Hence, CCl_4 is selected for CNT deposition by photo-enhanced CVD in this work.

4.3 Photolysis of Carbon Tetrachloride

The number of CCl_4 molecules undergoing photolysis can be estimated as follows. Carrier gas Ar and CCl_4 are used for CNT depositions. When Ar flow rate is 100 sccm, the chamber pressure is approximately 1.1 Torr for a specific setting of exhaust valve. When Ar and CCl_4 are admitted to the chamber, the chamber pressure is approximately 1.25 Torr. Thus partial pressure of CCl_4 is estimated to be 0.15 Torr. The chamber size is 0.5 l. Figure 4.7 is a schematic diagram of the inside of the chamber and shows the dimensions of chamber.

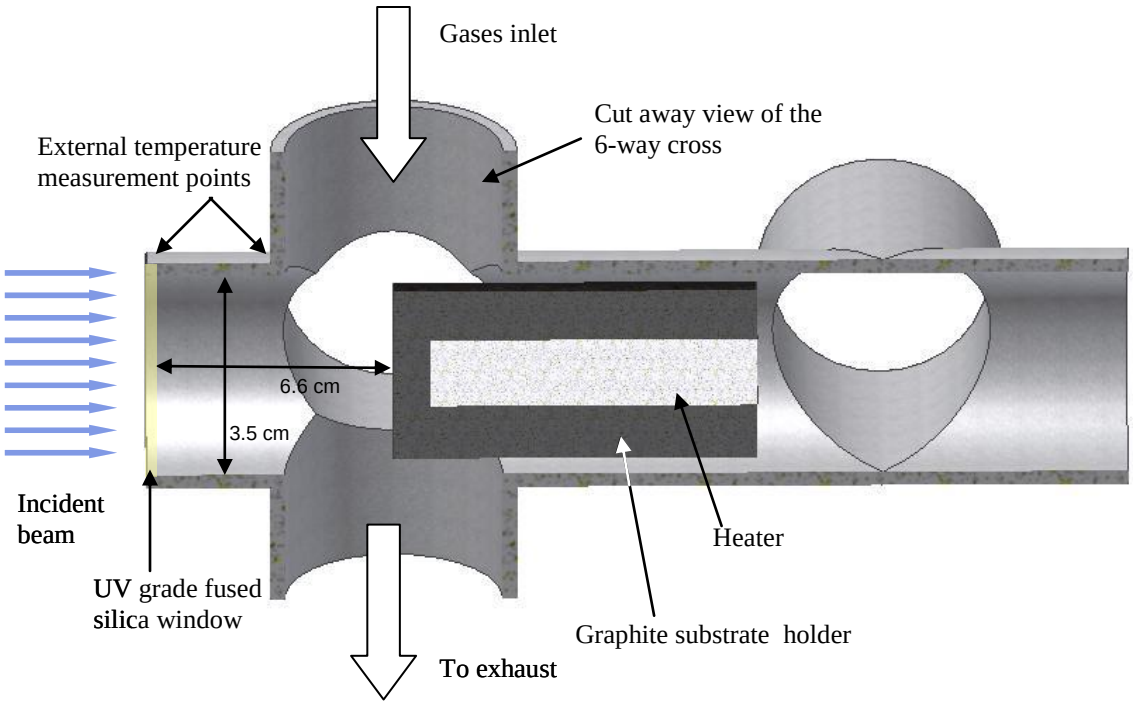

Figure 4.7. Schematic diagram of the chamber interior.

We can calculate the total moles of gas from the Ideal Gas Law: PV = nRT. Here P is total pressure, V is volume of the chamber, n is number of moles of gas, R is the gas constant and T is temperature of the chamber. The volume V of chamber and the gas constant R are fixed.

The total pressure can be maintained at 1.25 Torr. The ratio of $\frac{n_{Ar+CCl_4}}{n_{Ar}} = \frac{P_{Ar+CCl_4}}{P_{Ar}} = \frac{1.25}{1.1}$ since V, R and T are identical for both cases. Here $n_{(Ar+CCl_4)}$ is the total mole of Ar and CCl_4 gases and n_{Ar} is the mole of Ar, and $P_{(Ar+CCl_4)}$ and P_{Ar} are respectively chamber pressures associated with flow of both Ar and CCl_4 and Ar only. The n_{Ar} is estimated by knowing the chamber volume (0.5 l) and effective chamber temperature assumed to be 100 ˚C here. Total mole of Ar and CCl_4 gases is $\frac{1.25\times0.00132\times0.5}{0.0821\times373} = 2.69 \times 10^{-5}$. Thus concentration of CCl_4 (n_{CCl_4}) in 0.5 l, 0.15 Torr and 100 ˚C environment is 3.22×10^{-6} mole.

CNTs were deposited under 5 Torr, thus n_{Ar} is 9.5×10^{-5} mole and n_{CCl_4} is 1.3×10^{-5} mole. From Avogadro's number, the number of CCl_4 molecules in 1.3×10^{-5} mole is 7.83×10^{18}. In our experiment, approximately 7.83×10^{18} molecules of CCl_4 exist in the 0.5 l chamber. From the Beer-Lambert law, beam intensity I is given by $I = I_0 e^{-\sigma l N}$, where I_0 is incident beam intensity, σ is absorption cross section $\sigma = 8 \times 10^{-19}$ cm^2 from Fig. 4.6, l is length of medium and N is density of gas molecule. The incoming photon energy can be calculated from the light intensity given in Fig. 3.3. The light intensity I_0 = 18 mW/m^2 for 1 nm wavelength range centered at 200 nm and the cross section area of chamber entrance is 9.616 cm^2, thus the incident light power I'_0 is 1.73×10^{-2} mW. The number n of photons absorbed by CCl_4 per second at a given wavelength λ is $n = \frac{\lambda \cdot (I'_0 - I)}{h \cdot c} = \frac{\lambda \cdot I'_0 (1 - e^{-\sigma l N})}{h \cdot c}$. Where h is plank constant and c is speed of light. The quantum yield can be used to calculate the number of photolysed CCl_4 molecules.

$$Quantum\ yield(\Phi) = \frac{number\ of\ photolysed\ molecules}{number\ of\ absorbed\ photons}$$

The quantum yield of CCl_4 at 214 nm wavelength is 1. Thus we can assume that the number of absorbed photons by CCl_4 is the same as the number of photolysed CCl_4 molecules. The calculated number of absorbed photons by CCl_4 is 1.38×10^{13} molecules per second at 200 nm for l = 6.6 cm. When the focus is moved on the surface of sample, the collision rate of CCl_4 on the substrate is a factor for carbon material deposition. The system is assumed to be at equilibrium. The expression of number of molecules striking a surface is $\Phi_0 = \frac{\bar{p}_{CCl4}}{\sqrt{2\pi mkT}}$. Here, Φ_0 is number of molecules striking unit area of the wall per unit time, $\bar{p}_{CCl_4}$ is partial pressure of CCl_4, m is molecular mass and T is chamber temperature. The calculated collision rate of CCl_4 per unit area for our experimental condition is $\Phi_0 = \frac{66.66}{\sqrt{2\pi\times2.56\times10^{-25}\times1.38\times10^{-23}\times373}}$ is 1.17×10^{20} $cm^{-2}s^{-1}$.

4.4 Preliminary Experiment for Selecting Catalyst Layers

Preliminary experiments are carried out in order to decide on the most suitable catalyst layers and environmental conditions for annealing and deposition processes. Substrate size for this preliminary experiment is approximately 1 cm × 0.5 cm and four differently prepared sample substrates are located on the heated substrate holder at the same time. Thus number of experimental runs can be reduced and these four substrate samples can be compared to decide which sample is better for our experiments having been exposed to identical experimental conditions.

4.4.1 Annealing Conditions

The proper catalyst thickness and annealing conditions are decided after the preliminary experiments. Prior to annealing, the chamber is evacuated and Ar gas is introduced during evacuation to remove ambient air from the chamber. After 5 minutes of purging of ambient air, the Ar gas flow valve is closed and the chamber is evacuated until base pressure less than 10^{-2} Torr is reached. Ammonia gas flow and power for the heater are turned on to commence the

annealing process. The substrate holder is resistively heated using a *Watlaw Firerod 9280* heater, which is covered by graphite holder as described in section 3.2. A type K thermocouple is used for substrate temperature measurement and control. Pure ammonia gas of 99.999% purity is utilized during the annealing process as the ambient gas. The ammonia gas assists transformation of the catalyst thin film to nanoparticles [88]. The annealing temperature and the chamber pressure are varied during these preliminary experiments and adjusted to their designated values. The flow rate of ammonia gas is set at 100 sccm. The chamber pressure is changed by controlling the vacuum valve opening during the annealing process without changing the ammonia gas flow rate. Table 4.2 lists various conditions for annealing process investigated during these preliminary experiments.

Table 4.2. Catalyst annealing conditions employed in ammonia ambient.

	Run 1	Run 2	Run 3	Run 4	Run 5	Run 6	Run 7	Run 8	Run 9
Annealing temperature [°C]	350	350	350	375	375	375	400	400	400
Annealing pressure [Torr]	0.22	1	10	0.22	1	10	0.22	1	10

The result of nanoparticle formation can be observed with SEM images and the optimal annealing condition and catalyst thin film sample can be then determined.

Figure 4.8 shows SEM pictures of the four catalyst samples annealed at 400 °C and under 10 Torr chamber pressure (Run 9 in Table 4.2). These pictures show the effect of Al layer thicknesses on annealing of the catalyst sandwich. Figures 4.8 (a) and (b) correspond to the thinner Al layers and they indicate formation of a very few nanoparticles on the substrate surface

upon annealing. Figure 4.8 (d) corresponding to the thicker Al layers used indicates a low particle density. Figure 4.8 (c) corresponds to 5 nm thick Al layers and results in a denser nanoparticle formation upon annealing. The average diameter of particle size is approximately 42 nm for the 5 nm thick Al case and the particle distribution is more uniform. Figure 4.8 (d) shows that 10 nm Al layer thickness apparently is too thick with the nanoparticle formation becoming more sparse similar to the thinner Al layer thickness cases shown in figures 4.8 (a) and (b). From these measurements, a 5/1/5 nm Al/Ni/Al catalyst layer sandwich appears to be the optimal thicknesses for the 400 °C and 10 Torr annealing condition utilized here.

Figure 4.9 shows the effect of different chamber pressures during 400 °C anneal of the 5/1/5 nm thick catalyst samples corresponding to Runs 7 - 9 in Table 4.2. Figures 4.9 (a) - (c) respectively correspond to 0.22 Torr, 1 Torr and 10 Torr ambient pressure values respectively during the annealing cycle. Figure 4.9 indicates that all three samples have somewhat dense and uniform nanoparticle formation after the anneal cycle. However, the nanoparticles obtained at 1 Torr pressure were the smallest in size and the least dense followed by those formed at 0.22 Torr. The sample annealed at 10 Torr resulted in the largest and the densest nanoparticle formation among the three pressure values examined.

Figures 4.10 (a) - (c) show the results on 5/1/5 nm catalyst samples annealed in ammonia ambient at 10 Torr pressure but at three different temperature values of 350, 375 and 400 °C corresponding to Runs 3, 6 and 9 in Table 4.2. The annealing temperature is decided from this experiment. The nanoparticles obtained after annealing at 350 °C are bigger but distributed somewhat sparingly compared to the nanoparticles obtained after 375 and 400 °C annealing. The sample annealed at 375 °C shows smaller and denser nanoparticles than the one annealed at 350 °C, however they are larger and more sparsely deposited compared to the sample annealed at

400 °C. The nanoparticles deposited under 375 °C annealing temperature resemble closer to the 350 °C annealed sample than the 400 °C annealed sample. Based on the above observations, it is concluded that the catalyst annealing conditions corresponding to Run 9 in Table 4.2 and catalyst thin film thickness (5/1/5 nm) are the most appropriate for CNT and hexagonal diamond growth for this work.

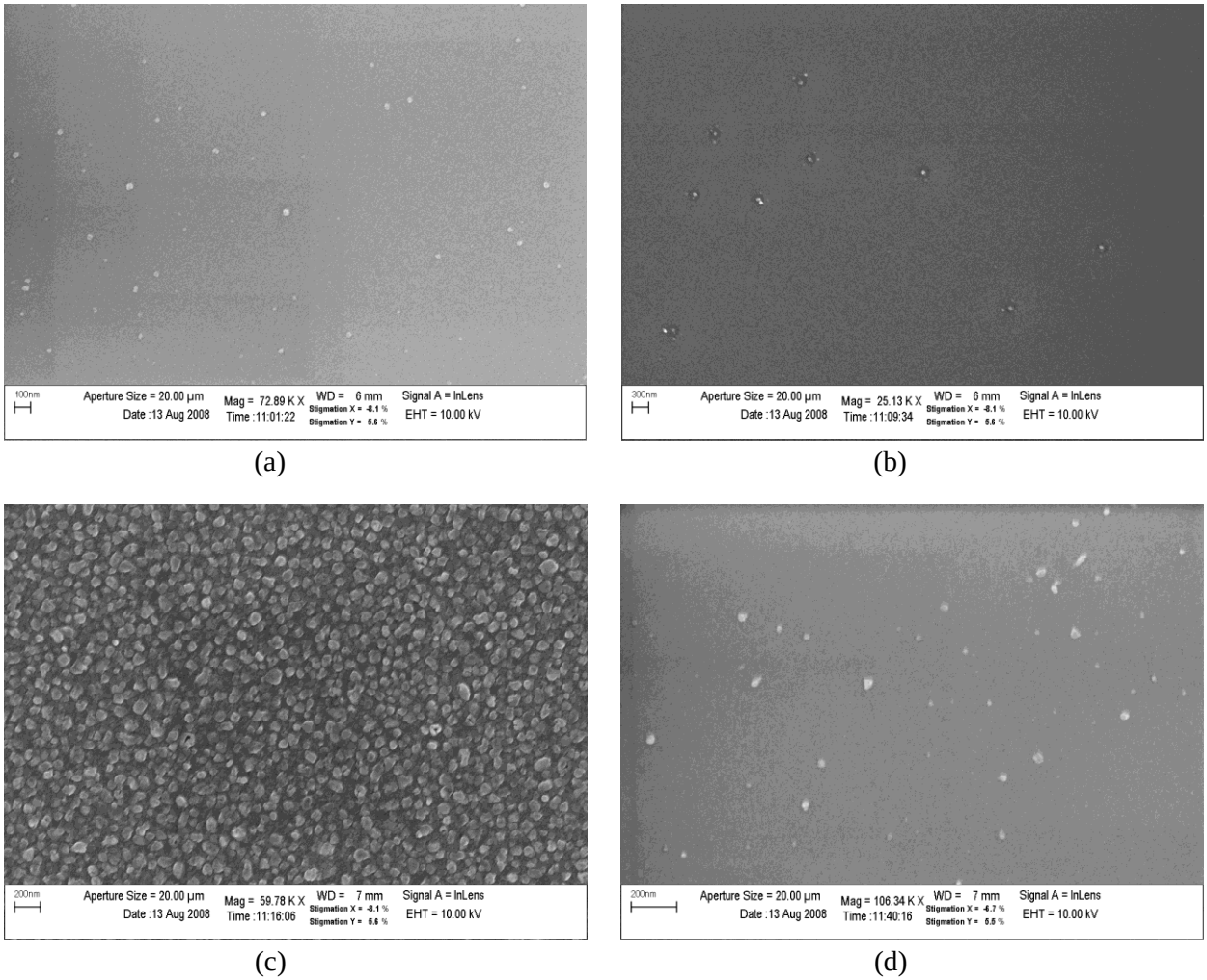

Figure 4.8. SEM pictures of samples annealed in ammonia at 400 °C and 10 Torr chamber pressure but with different aluminum thicknesses. The Al/Ni/Al catalyst thicknesses: (a) 1/1/1 nm, (b) 3/1/3 nm, (c) 5/1/5 nm and (d) 10/1/10 nm. The scale bar indicated in (a) is 100 nm, in (b) is 300 nm and in (c) and (d) are 200 nm wide.

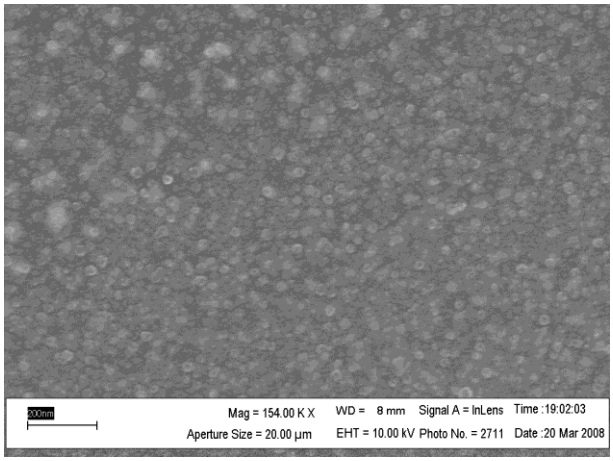

(a)

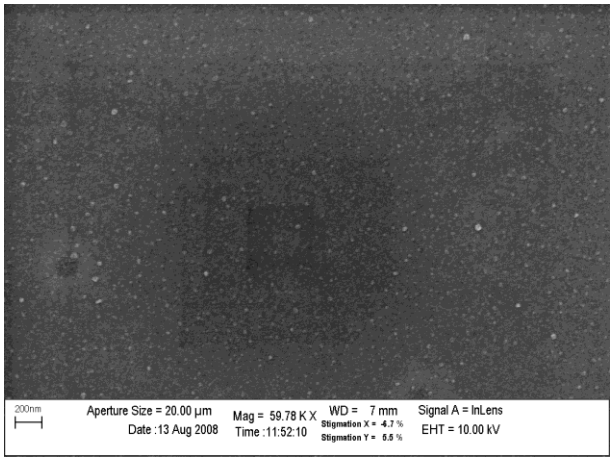

(b)

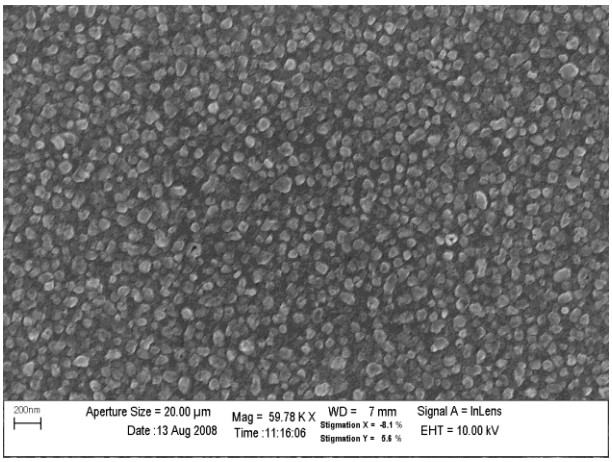

(c)

Figure 4.9. SEM pictures of 5/1/5 nm catalyst samples annealed in ammonia at 400 °C but at different chamber pressures: (a) 0.22 Torr, (b) 1 Torr and (c) 10 Torr. The scale bars are all 200 nm wide.

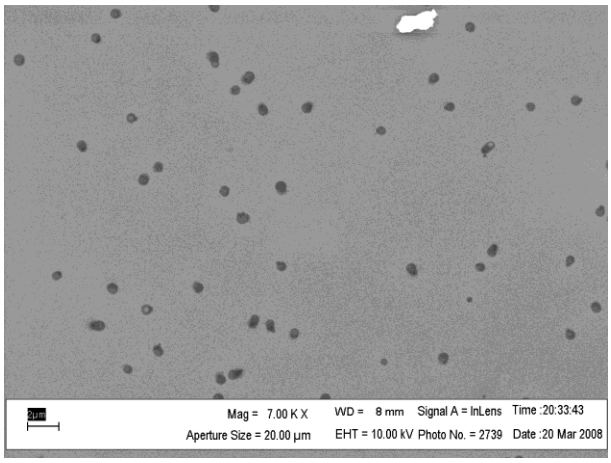

(a)

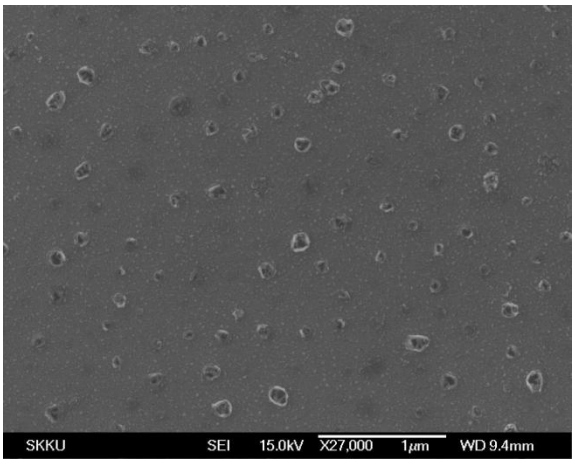

(b)

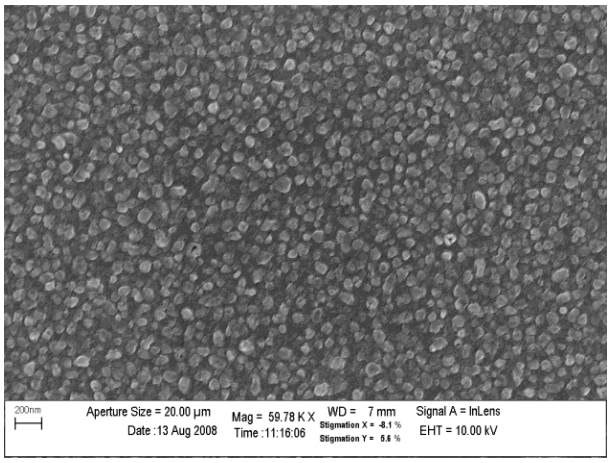

(c)

Figure 4.10. SEM pictures of 5/1/5 nm catalyst samples annealed at 10 Torr chamber pressure but at different annealing temperatures: (a) 350 °C, (b) 375 ˚C and (c) 400 °C. The scale bar in (a) is 2 µm, in (b) is 1 µm and in (c) is 200 nm wide.

The SEM images on nanoparticle formation gives information on deciding the optimal thickness of thin film catalyst and the annealing condition. Sample # 3 in Table 4.1 gave satisfactory results from our preliminary experiment. Based on this, two other catalyst layer combinations as shown in Table 4.3 are investigated.

Table 4.3. Al/Ni/Al catalyst sandwich layer film thicknesses utilized for the follow-up experiment.

Combination	Top layer Al thickness (nm)	Mid-layer Ni thickness (nm)	Bottom layer Al thickness (nm)
# 1	3 nm	2 nm	3 nm
# 2	5 nm	1 nm	5 nm
# 3	5 nm	3 nm	5 nm

Figures 4.9 and 4.10 respectively show that higher annealing pressure and temperature yield better result in terms of nanoparticle transformation. Thus 375 °C annealing temperature is replaced by 450 °C annealing temperature process and 0.22 and 1 Torr annealing pressures are eliminated in the follow-up experiment. The detailed annealing conditions for final experiment are indicated in Table 4.4.

Table 4.4. Catalyst annealing conditions employed in ammonia ambient for the follow-up experiment

	Run 1	Run 2	Run 3
Annealing temperature [°C]	350	400	450
Annealing pressure [Torr]	10	10	10

The annealing results of the follow-up experiment are shown in Figs. 4.11 - 4.13. Figures 4.11 (a) - (c) show the results on 3/2/3 nm catalyst samples annealed in ammonia ambient at 10 Torr pressure at three different temperature values of 350, 400 and 450 °C. The nanoparticles obtained after annealing at 350 °C are bigger compared to the nanoparticles obtained after 400 and 450 °C annealing. The sample annealed at 400 °C shows smaller and denser nanoparticles than the one annealed at 350 °C, however they are larger deposited compared to the sample annealed at 450 °C. The nanoparticles deposited under 400 °C annealing temperature resemble closer to the 450 °C annealed sample than the 350 °C annealed sample. Figure 4.12 and 4.13 show the results of nanoparticle formation on 5/1/5 and 5/3/5 nm catalyst samples respectively and the annealing conditions are same as that of 3/2/3 nm catalyst sample. The temperature effect on nanoparticle formation of 5/1/5 and 5/3/5 nm catalyst samples shows similar tendency of 3/2/3 nm catalyst sample with 450 ˚C anneal temperature yielding the smallest particle size.

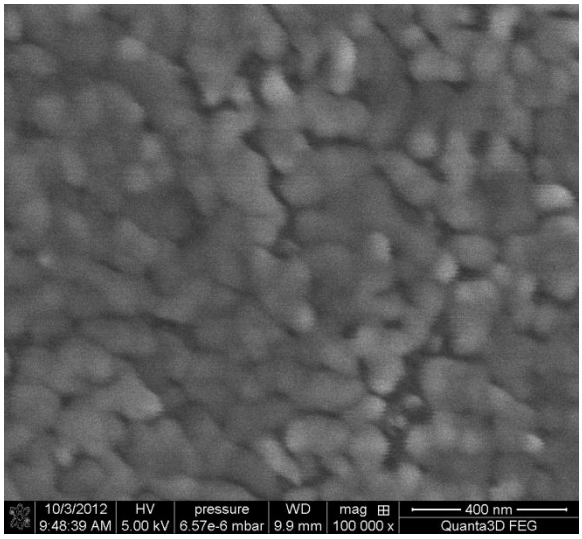

(a)

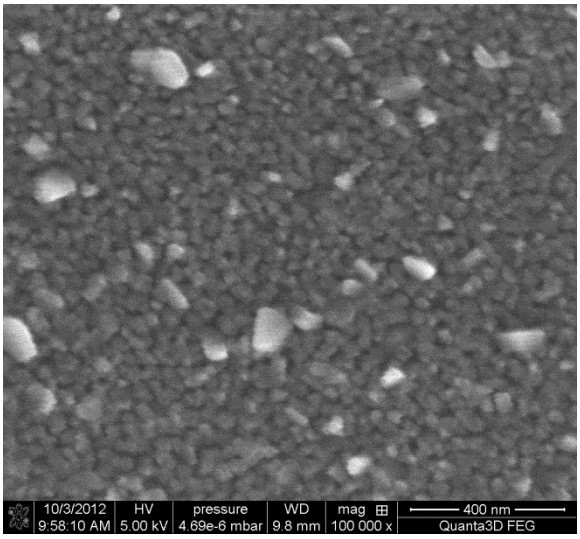

(b)

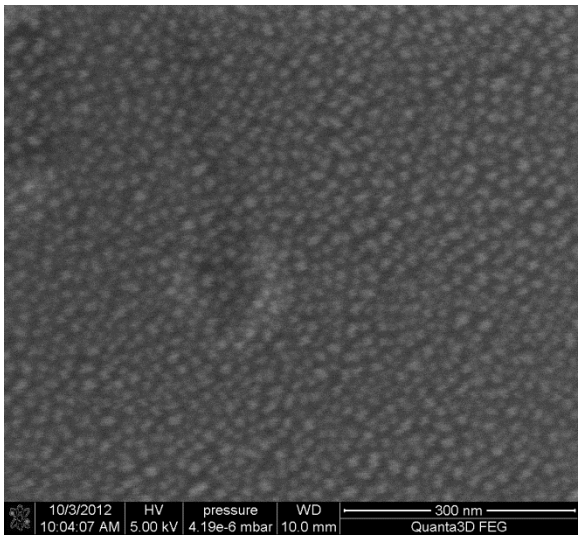

(c)

Figure 4.11. SEM pictures of 3/2/3 nm catalyst samples annealed at 10 Torr chamber pressure but at different annealing temperatures: (a) 350 °C, (b) 400 ˚C and (c) 450 °C. The scale bar in (a) and (b) are 400 nm and in (c) is 300 nm wide.

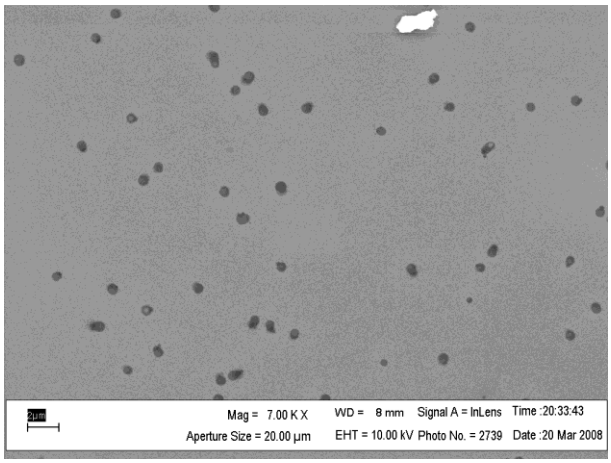

(a)

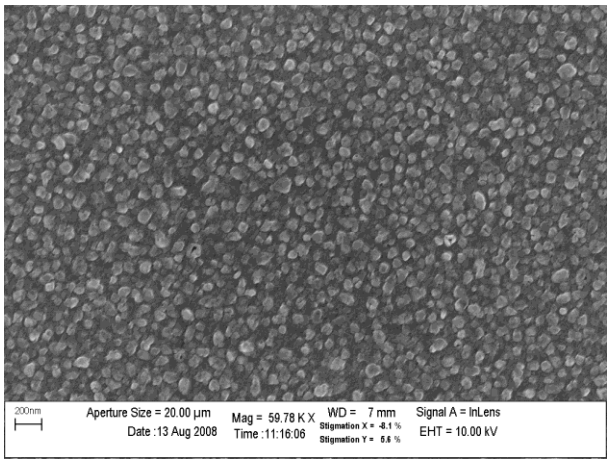

(b)

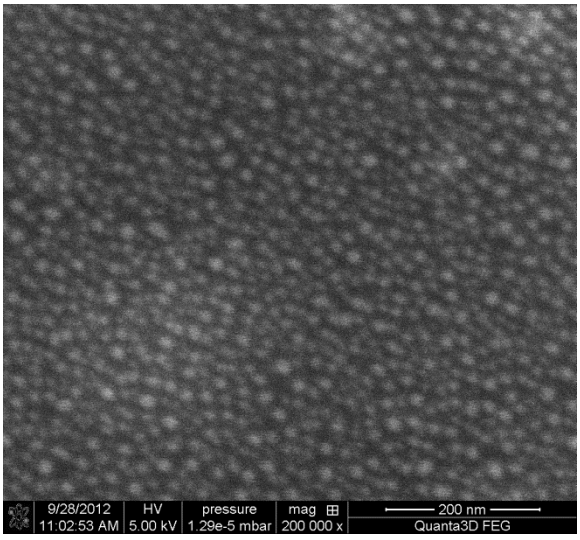

(c)

Figure 4.12. SEM pictures of 5/1/5 nm catalyst samples annealed at 10 Torr chamber pressure but at different annealing temperatures: (a) 350 °C, (b) 400 ˚C and (c) 450 °C. The scale bar in (a) is 2 µm, in (b) and (c) are 200 nm wide.

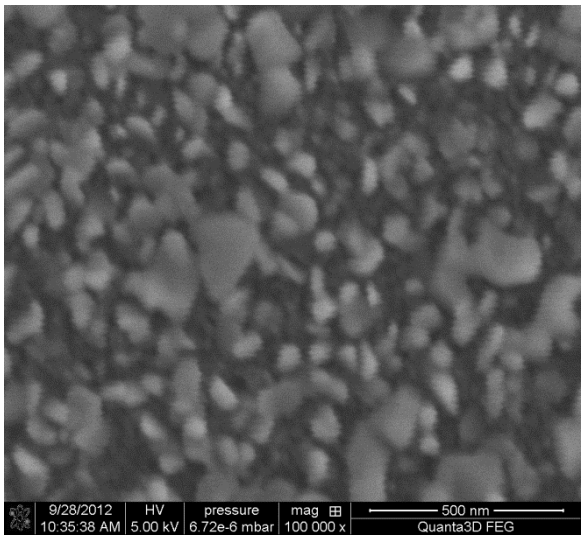

(a)

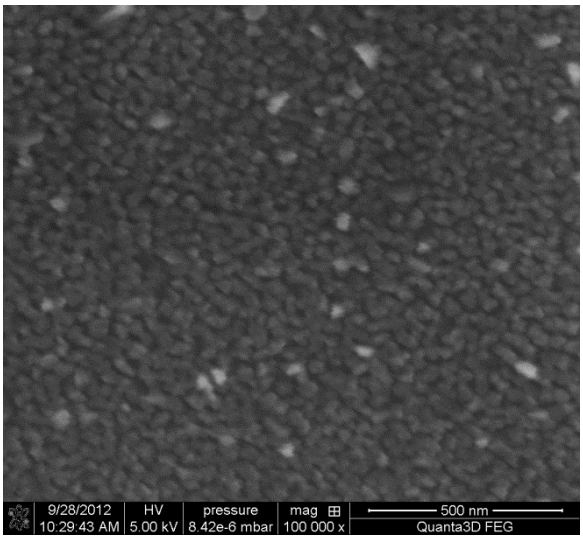

(b)

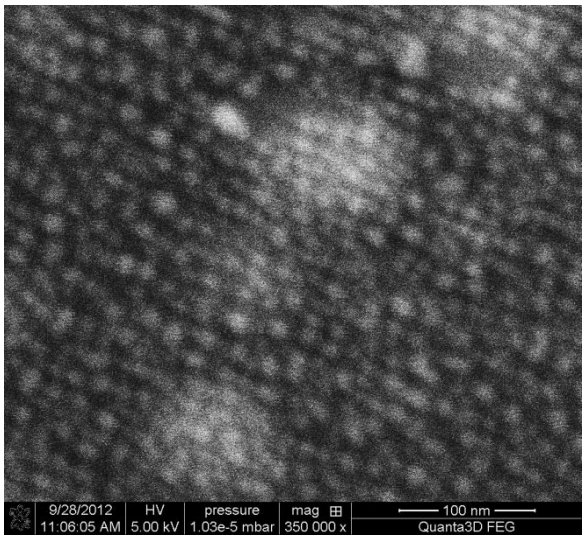

(c)

Figure 4.13. SEM pictures of 5/3/5 nm catalyst samples annealed at 10 Torr chamber pressure but at different annealing temperatures: (a) 350 °C, (b) 400 ˚C and (c) 450 °C. The scale bar in (a) and (b) are 500 nm and in (c) is 100 nm wide.

4.4.2 Preliminary Deposition Process

Preliminary study of the catalyst annealing process allows optimization of experimental conditions to transform the thin film layers into nanoparticles. Tables 4.3 and 4.4 represent selected thickness of catalyst thin film and annealing conditions respectively. After completing a 25-minute annealing cycle, the ammonia gas supply is stopped. The CNT or hexagonal diamond deposition process is started immediately following the annealing cycle by commencing the flow of CCl_4 precursor in the chamber and turning on the Xe arc lamp light source (Hanovia 976 C-1) having a broad wavelength spectrum from 200 nm to 2400 nm (Fig. 3.3). Argon is used as a carrier gas for CCl_4. The feed pipe between the CCl_4 bubbler and the growth chamber is heated to 95 °C with a heating tape. The substrate temperature for deposition process is kept constant at the annealing temperature. The CNT or hexagonal diamond deposition processes are carried out for the duration of between 30 minutes and 3 hours under various conditions. Table 4.5 gives the process conditions employed during the preliminary deposition experiments. After CNT or hexagonal diamond deposition, argon gas flow is made to bypass the CCl_4 bubbler for 5 minutes and the substrate heater is turned off. The substrates are cooled prior to their removal from the chamber. CNT and hexagonal diamond deposition is carried out on three different types of catalyst samples previously listed in Table 4.3.

Table 4.5. Deposition conditions utilized during preliminary deposition experiment for CNT and hexagonal diamond deposition.

Deposition temperature (˚C)	Total chamber pressure (Torr)	Partial pressure (Torr)		Deposition time (Hours)
		Ar	CCl_4	
350, 400, 450	3	2.5, 2	0.5, 1	0.5, 1.5, 3
	5	4.5, 4, 3	0.5, 1, 2	
	10	9.5, 9, 7	0.5, 1, 3	

The results of preliminary deposition experiment show no CNT or hexagonal diamond deposited regardless of the deposition time and partial pressure for total chamber pressure under 3 Torr. Moreover, CNT and hexagonal diamond were not observed when the deposition temperature was 350 ˚C. Thus 400 and 450 ˚C deposition temperature and 5 and 10 Torr total chamber pressure conditions were further investigated. Table 4.6 shows deposition conditions for these follow-up experiments.

4.5. Chapter Summary

The details of preliminary experiments for growth of CNT and hexagonal diamond are provided in this chapter. This work can be separated as the annealing step and the deposition process. Annealing process is necessary for the formation of nanoparticles from the thin film catalyst. The optimized annealing conditions which consists of chamber pressure, substrate temperature and thickness of catalyst thin film, are decided through the preliminary experiments. The precursor gas selection is discussed for the deposition process. Preliminary experiments determine conditions for deposition process in terms of chamber pressure, partial pressure of Ar and CCl_4, deposition substrate temperature and deposition time for the follow-up experiments.

Table 4.6. Process conditions for follow-up deposition experiments for CNT and hexagonal diamond.

Deposition temperature (˚C)	Total chamber pressure (Torr)	Partial pressure (Torr)		Deposition time (Hours)
		Ar	CCl_4	
400	5	4.5	0.5	0.5
				1.5
				3
		4	1	0.5
				1.5
				3
		3	2	0.5
				1.5
				3
	10	9.5	0.5	0.5
				1.5
				3
		9	1	0.5
				1.5
				3
		7	3	0.5
				1.5
				3
450	5	4.5	0.5	0.5
				1.5
				3
		4	1	0.5
				1.5
				3
		3	2	0.5
				1.5
				3
	10	9.5	0.5	0.5
				1.5
				3
		9	1	0.5
				1.5
				3
		7	3	0.5
				1.5
				3

CHAPTER 5. RESULTS

Several different conditions for annealing and deposition process have been experimented to synthesize CNT and hexagonal diamond on SiO_2 coated Si and glass substrates. Different conditions of annealing and deposition process give different results. The annealing process and result of nanoparticle formation is explained in chapter 4.

Substrate temperature, total chamber pressure and the ratio of Ar and CCl_4 partial pressure during deposition process are among the factors involved in deposition of carbon films in the photo-enhanced CVD system assembled here for this research. When annealing temperature is lower than 300 ˚C, the catalyst thin film layers do not change to nanoparticles properly. When the annealing temperature is higher than 350 ˚C, catalyst thin film changes to nanoparticles. However, carbon nanotube or hexagonal diamond deposition was not observed when the deposition substrate temperature was 350 ˚C. Growth of CNT is observed for substrate temperatures on or above 400 ˚C and hexagonal diamond growth is observed for substrate temperature of 450 ˚C. The total chamber pressure and the ratio of Ar and CCl_4 partial pressures during deposition process are critical factors for growth. CNT is deposited when total pressure is 5 Torr and partial pressures of Ar and CCl_4 are respectively 4.5 and 0.5 Torr. Hexagonal diamond growth was observed at 10 Torr total pressure with 9 Torr Ar and 1 Torr CCl_4 partial pressure or 7 Torr Ar and 3 Torr CCl_4 partial pressure. CNT deposition is not observed with the total pressure of 10 Torr even though the ratio of Ar and CCl_4 partial pressure values are retained the same at 9 to 1. Hexagonal diamond deposition is not observed at the lower total pressure of 5 Torr even though the ratio of Ar and CCl_4 partial pressures is maintained at the same value of 9 to 1. The deposition time in this work is 30 minutes for CNT deposition and 1.5 hours or more

for hexagonal diamond deposition. Hexagonal diamond platelets are almost fully grown during three hour deposition with 1.5 hour deposition time providing intermediary information on hexagonal diamond growth mechanism.

5.1 Results on CNT Growth

Carbon nanotubes can be grown with photo-enhanced CVD at 400 ˚C substrate temperature. The purpose of annealing process is to transform the thin catalyst films to nanoparticles. There are four parameters of interest for the annealing process; thickness of catalyst layers, substrate temperature, chamber pressure and ambient gas. The optimal conditions for catalyst thickness and annealing are based on initial experiments listed in Tables 4.3 and 4.4. The optimal growth conditions are obtained from experiments listed in Table 4.6. The optimal results are repeated for repeatability. CNT can be deposited on three different types of catalyst thickness at both 400 and 450 ˚C substrate temperatures, at 5 Torr total pressure and Ar to CCl_4 partial pressure ratio of 9:1. Figures 5.1 to 5.6 show the results of CNT deposition at different deposition conditions and catalyst thicknesses.

Figures 5.1 - 5.3 show the results of CNT deposition under same annealing and deposition conditions but with different catalyst layers. The annealing condition is 400 ˚C for substrate temperature and 10 Torr chamber pressure in ammonia environment. The deposition condition is 400 ˚C substrate temperature, 5 Torr chamber pressure with Ar to CCl_4 partial pressure ratio of 9:1 and 30 minutes deposition time. The Al/Ni/Al catalyst sandwich layer thickness for Fig. 5.1 is 3/2/3 nm, for Fig. 5.2 is 5/1/5 nm and for Fig. 5.3 is 5/3/5 nm. A comparison of Figs. 5.1 - 5.3 shows the effect due to different catalyst layer thicknesses. Each figure of CNT deposition shows different magnification and location. Figure 5.1 shows deposited CNT sparsely covering the substrate surface. Figure 5.2 shows much more densely deposited

CNT and the width of deposited CNT is approximately 45 nm. Figure 5.3 shows the CNT deposition density to be lower than Fig. 5.2 but the width of CNT is almost same as in Fig. 5.2.

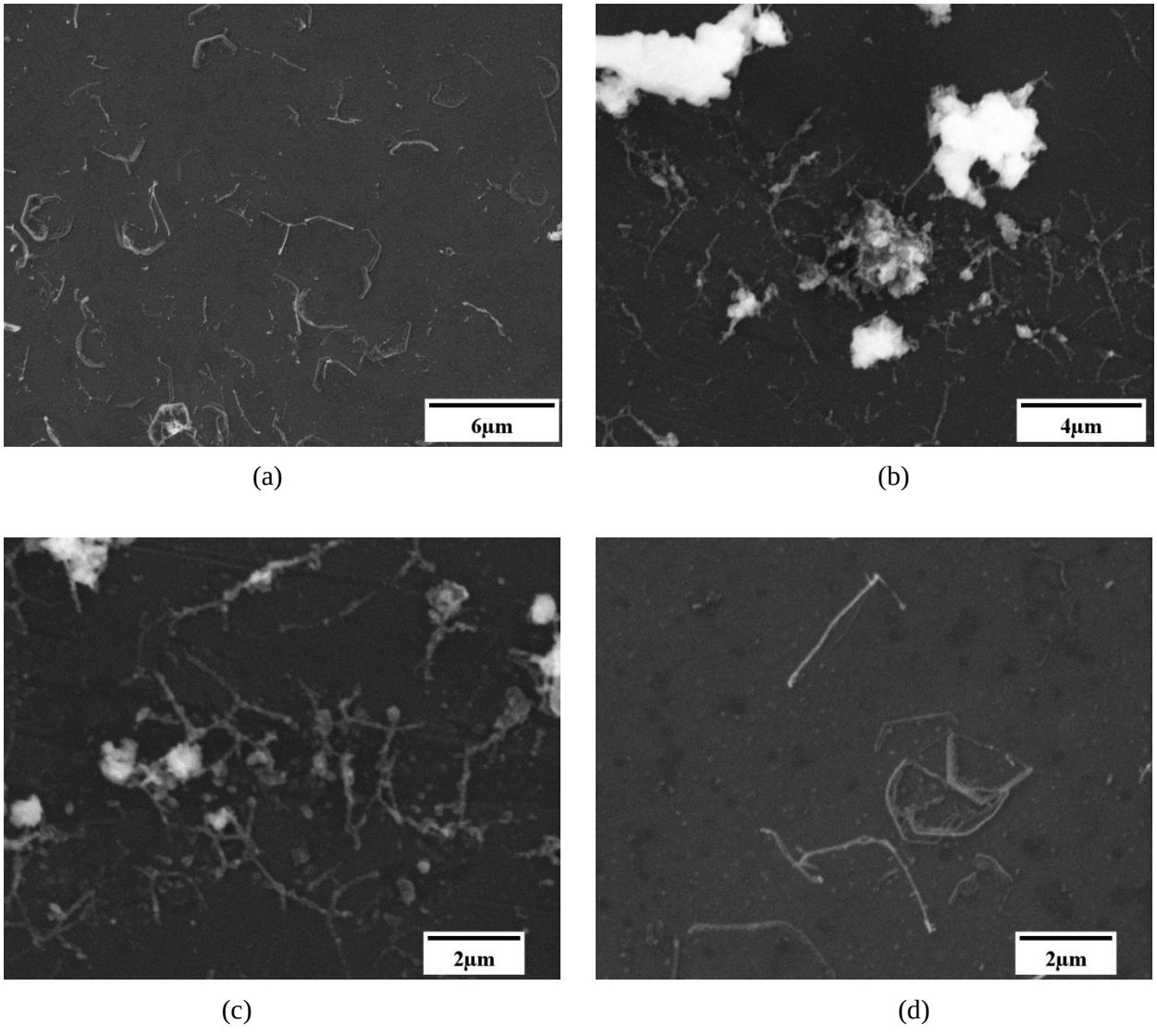

(a) (b)

(c) (d)

Figure 5.1. CNT deposition with 3/2/3 nm catalyst thin film sample, 400 ˚C annealing process under 10 Torr ammonia environment. Deposition temperature of 400 ˚C at 5 Torr total chamber pressure with Ar to CCl_4 partial pressure ratio of 9:1 and 30 min. deposition time.

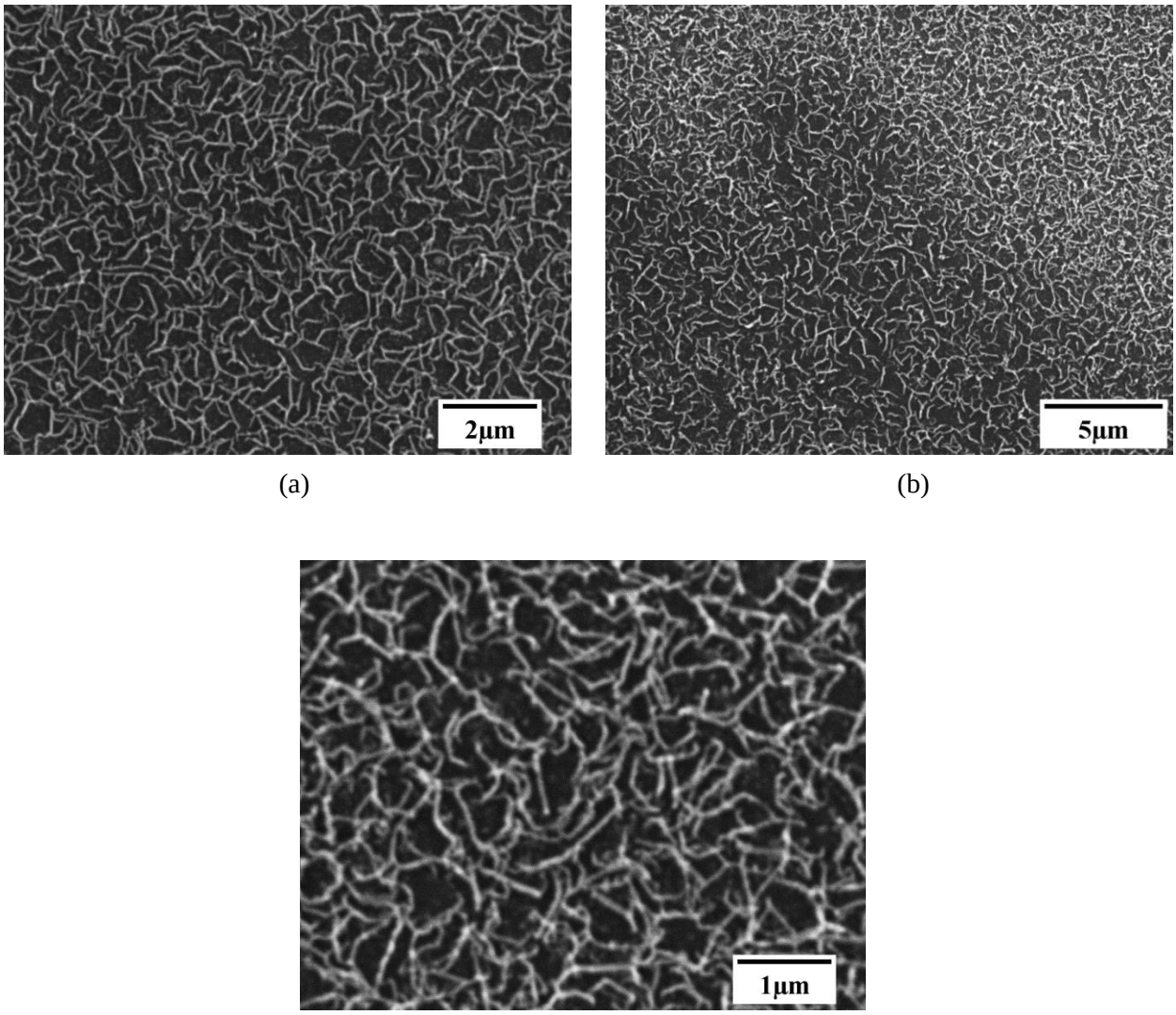

(a) (b)

(c)

Figure 5.2. CNT deposition with 5/1/5 nm catalyst thin film sample, 400 ˚C annealing process under 10 Torr ammonia environment. Deposition temperature of 400 ˚C at 5 Torr total chamber pressure with Ar to CCl_4 partial pressure ratio of 9:1 and 30 min. deposition time.

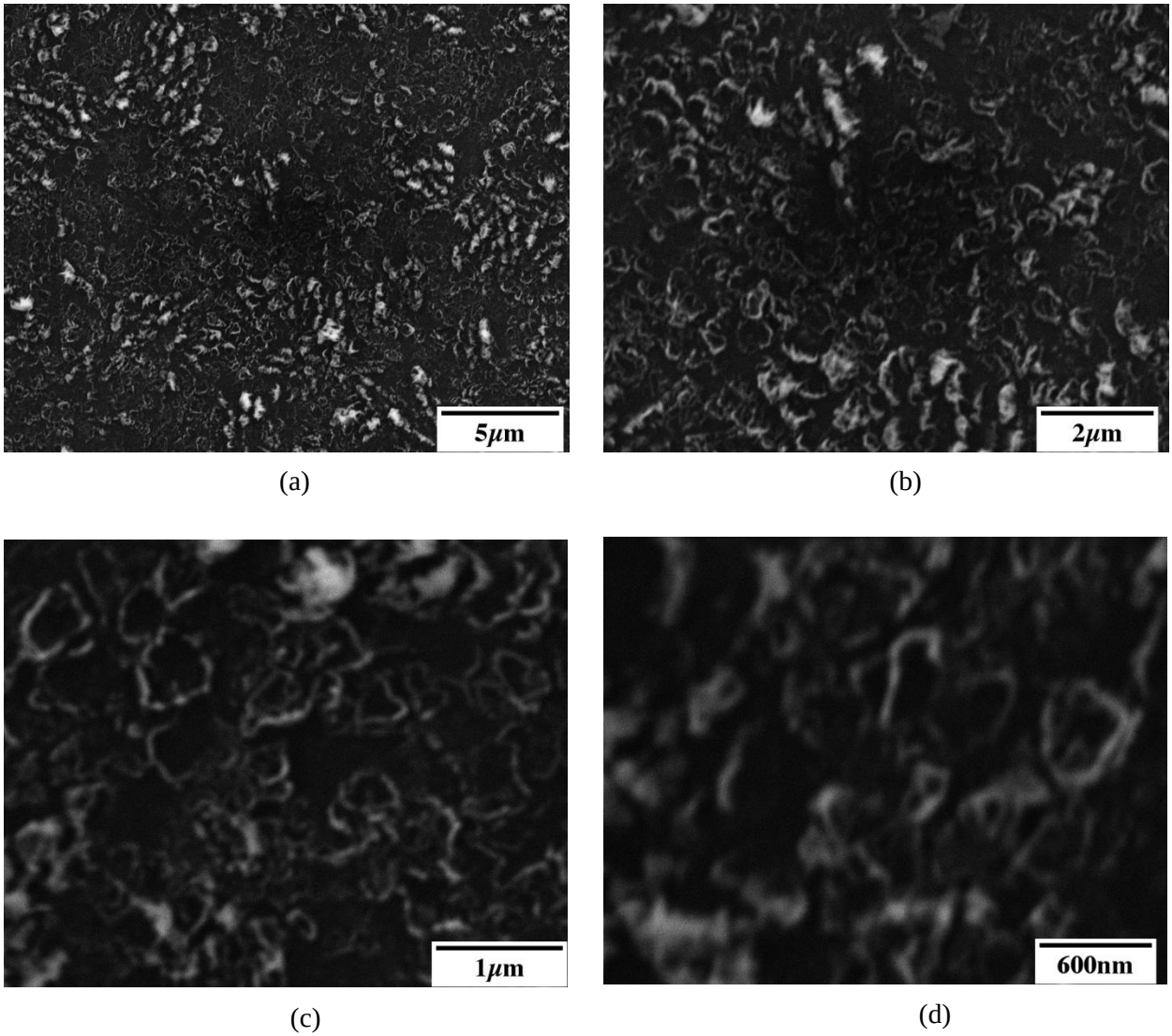

(a) (b)

(c) (d)

Figure 5.3. CNT deposition with 5/3/5 nm catalyst thin film sample, 400 ˚C annealing process under 10 Torr ammonia environment. Deposition temperature of 400 ˚C at 5 Torr total chamber pressure with Ar to CCl_4 partial pressure ratio of 9:1 and 30 min. deposition time.

Figures 5.4 - 5.6 also show the result of CNT deposition for different catalyst layer thicknesses but under different annealing and deposition condition from those for Figs. 5.1 - 5.3. The annealing condition is 450 ˚C for substrate temperature and 10 Torr chamber pressure in ammonia ambient. The deposition condition is 450 ˚C substrate temperature at 5 Torr chamber pressure with Ar to CCl_4 partial pressure ratio of 9:1 and 30 minutes deposition time. The catalyst Al/Ni/Al layer thickness for Fig. 5.4 is 3/2/3 nm, for Fig. 5.5 is 5/1/5 nm and for Fig. 5.6 is 5/3/5 nm. A comparison of Figs. 5.4 - 5.6 show the effects of different catalyst layer thicknesses for the 450 ˚C case.

Figure 5.4 shows sparsely deposited CNT and the width of CNT is approximately 5 nm. The deposition density of Figs. 5.5 and 5.6 is similar and not much denser than Fig. 5.4. The catalyst layer thicknesses for this sample in Fig. 5.4 are same as that for Fig. 5.1. The difference between Figs. 5.1 and 5.4 is deposition temperature. It seems the higher deposition temperature reduces the width of deposited CNT. This is somewhat anticipated from the well known results that indicate that the formation of single wall carbon nanotube (SWCNT) needs more energy than required in the growth of multi wall carbon nanotube (MWCNT).

Figures 5.5 and 5.6 show reduced CNT deposition density compared to Figs. 5.2 and 5.3. It indicates that the proper deposition temperature for CNTs is around 400 ˚C in this experiment. The deposition density of CNT depends on the applied energy. If the energy is lower or higher than the optimum energy, the deposition density decreases.

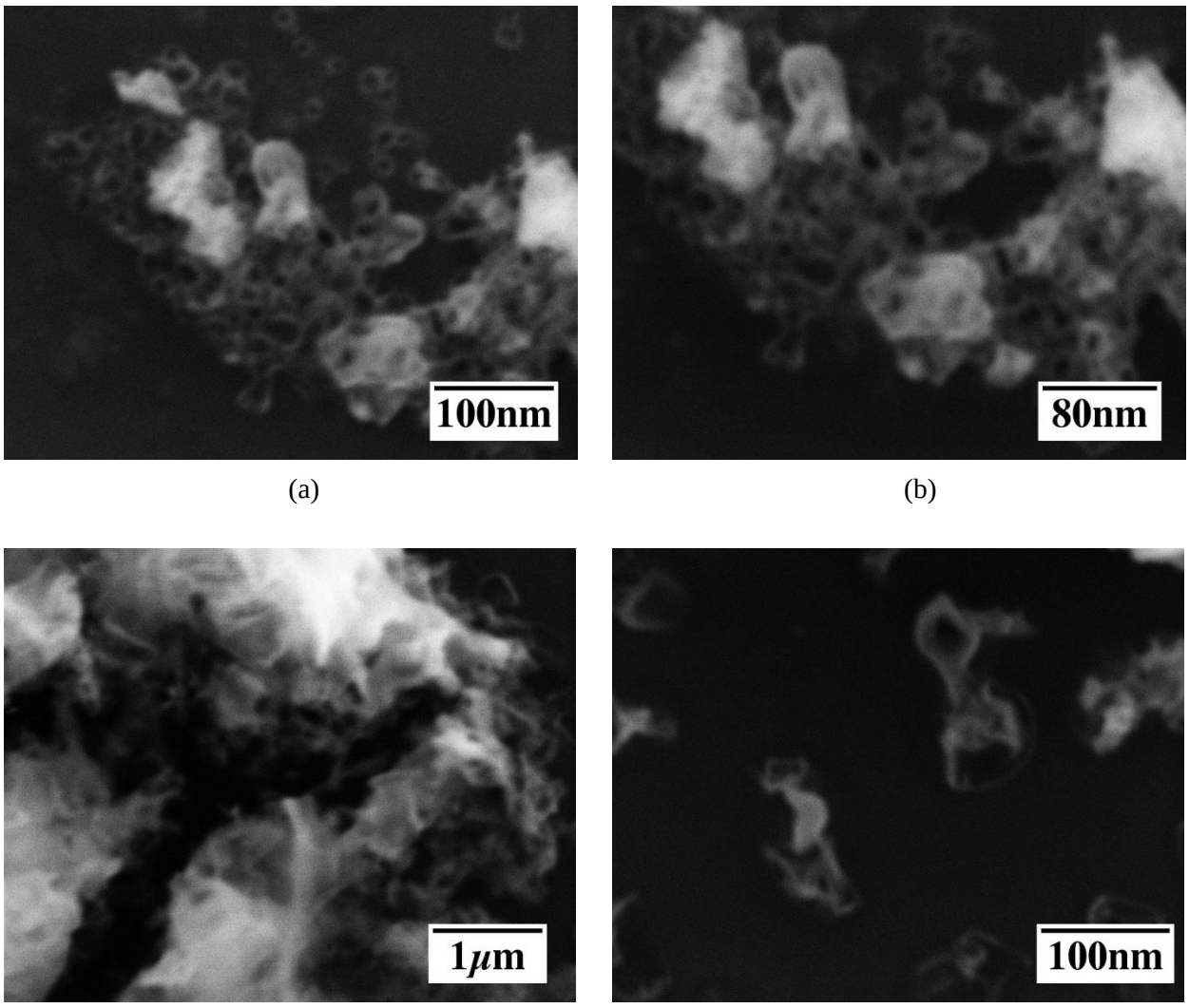

(a) (b)

(c) (d)

Figure 5.4. CNT deposition with 3/2/3 nm catalyst thin film sample, 450 ˚C annealing process under 10 Torr ammonia environment. Deposition temperature of 450 ˚C at 5 Torr total chamber pressure with Ar to CCl_4 partial pressure ratio of 9:1 and 30 min. deposition time.

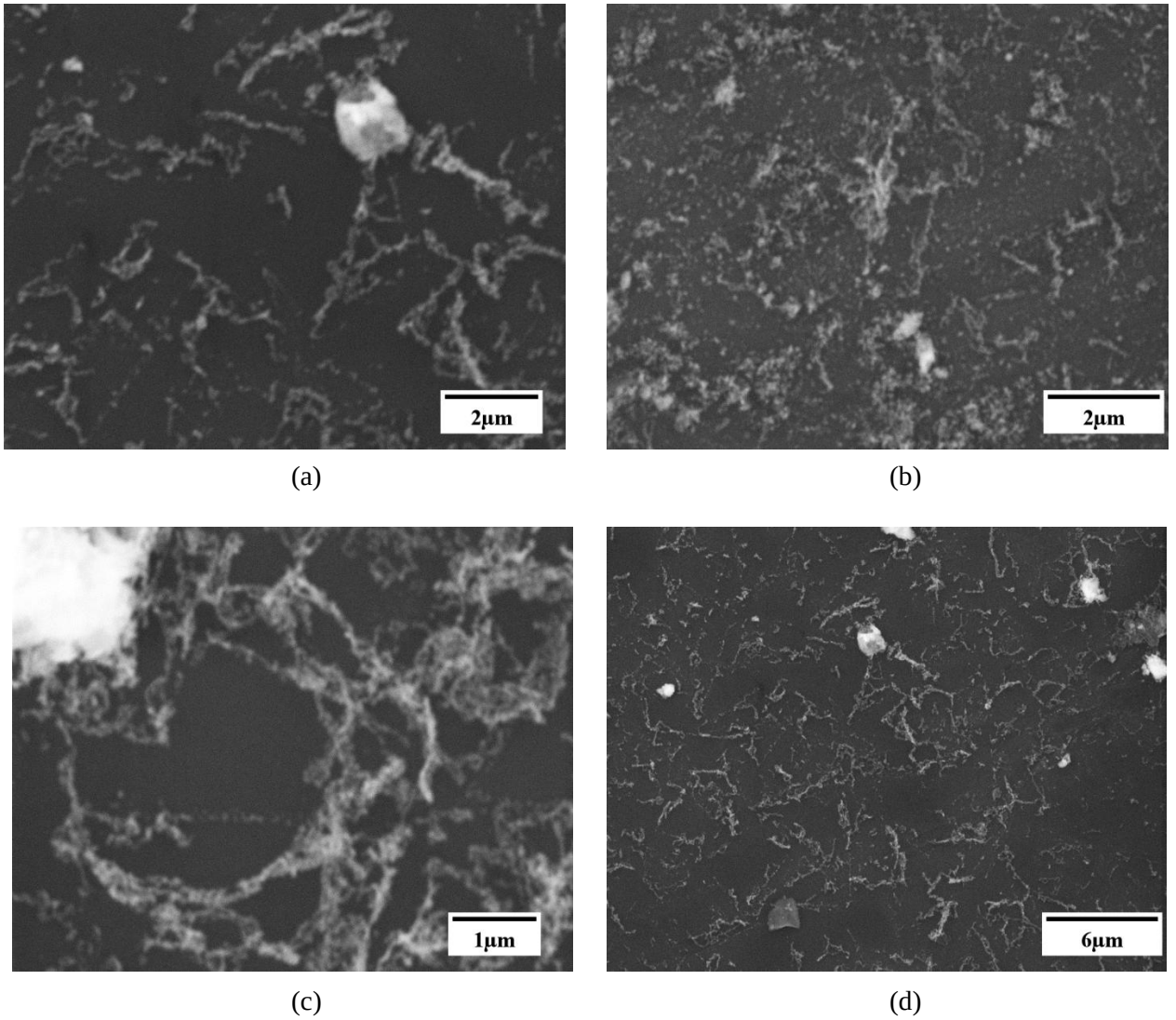

(a) (b)

(c) (d)

Figure 5.5. CNT deposition with 5/1/5 nm catalyst thin film sample, 450 ˚C annealing process under 10 Torr ammonia environment. Deposition temperature of 450 ˚C at 5 Torr total chamber pressure with Ar to CCl_4 partial pressure ratio of 9:1 and 30 min. deposition time.

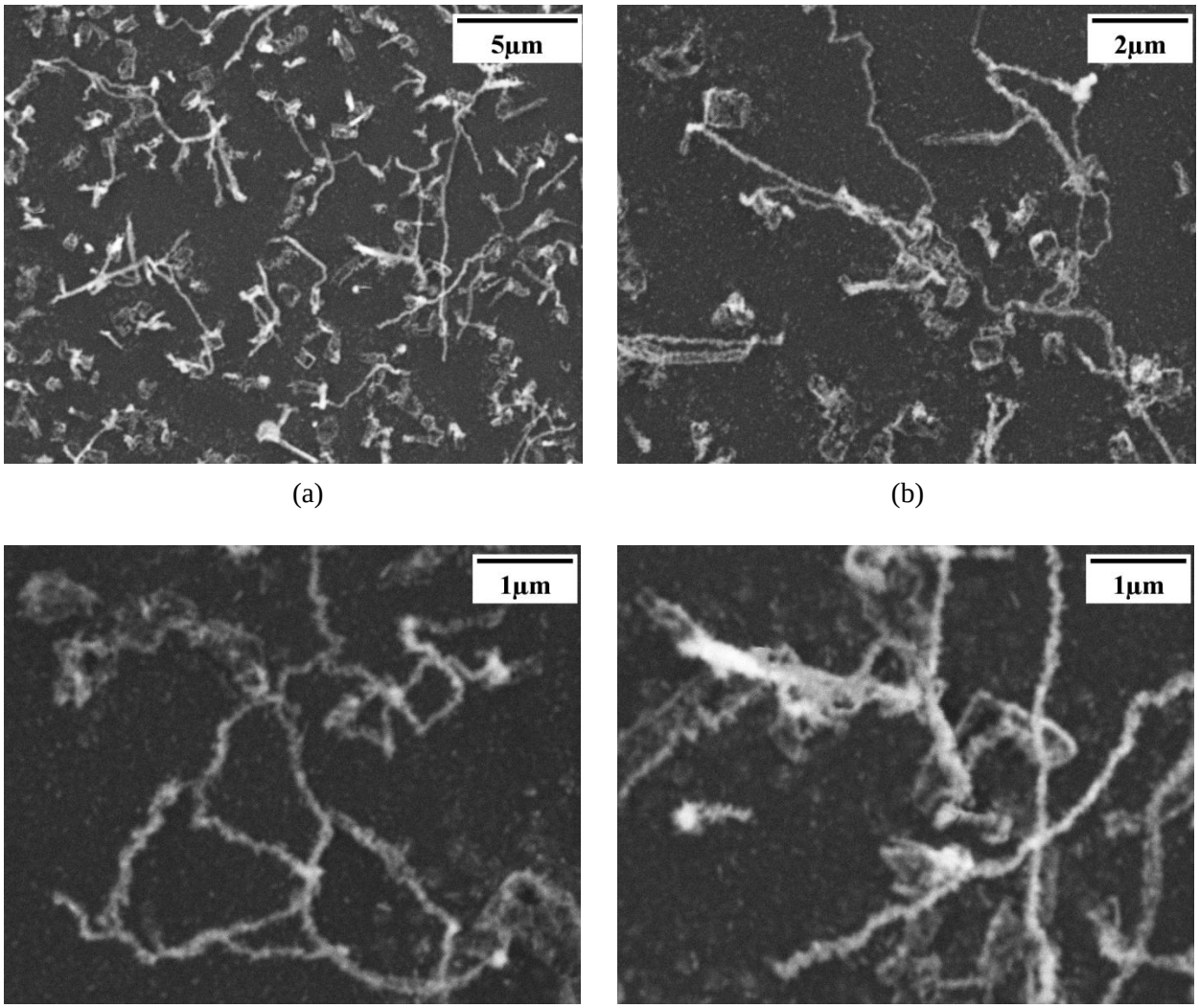

Figure 5.6. CNT deposition with 5/3/5 nm catalyst thin film sample, 450 ˚C annealing process under 10 Torr ammonia environment. Deposition temperature of 450 ˚C at 5 Torr total chamber pressure with Ar to CCl_4 partial pressure ratio of 9:1 and 30 min. deposition time.

5.2 Results on Hexagonal Diamond Deposition

The conditions for hexagonal diamond synthesis are same as those mentioned in Table 4.4 for the annealing process and those in Table 4.6 for the deposition process. In general, it takes longer time to synthesize hexagonal diamond than CNT. The CNT deposition time utilized in this work is approximately 30 minutes but for hexagonal diamond deposition time used varied from 1.5 to 3 hours. One and half hour deposition time for hexagonal diamond provided insight regarding hexagonal diamond growth process. Hexagonal diamond growth is observed with use of each of the three types of catalyst samples. However, the growth was observed only at 450 ˚C substrate temperature and only at 10 Torr total deposition pressure among the different pressures investigated. The partial pressure of Ar and CCl_4 in this work is maintained at either 7 and 3 Torr or 9 and 1 Torr respectively. Figures 5.7 - 5.12 show hexagonal diamond grains or thin films for various catalyst thin film layers and deposition conditions. In chapter 6, data is presented to identify these deposited layers to be hexagonal diamond. The partial pressures of Ar and CCl_4 in Figs. 5.7 - 5.9 is 7 and 3 Torr respectively and Figs. 5.10 - 5.12 is 9 and 1 Torr respectively. Figures 5.7 - 5.9 show SEM pictures of hexagonal diamond deposition with three different catalyst samples but with same annealing and deposition conditions.

Figure 5.7 shows hexagonal diamond deposition on a sample with 3/2/3 nm thick Al/Ni/Al coated substrate. The figure shows growth at various magnifications. Figure 5.7 (a) shows large area deposition and 5.7 (b) indicates sparse deposition of hexagonal diamond. Figure 5.7 (c) indicates that there are other carbon materials deposited along with hexagonal diamond.

Figure 5.8 shows hexagonal diamond deposition on a sample with 5/1/5 nm thick Al/Ni/Al coated substrate. Figure 5.8 (a) shows the deposition over a large area. The deposited hexagonal diamond is denser than observed in Fig. 5.7. Figure 5.8 (c) is a higher magnification

image. It is difficult to identify carbon materials other than hexagonal diamond. The charging problem while taking the SEM image results in blurred edges on the hexagonal diamond.

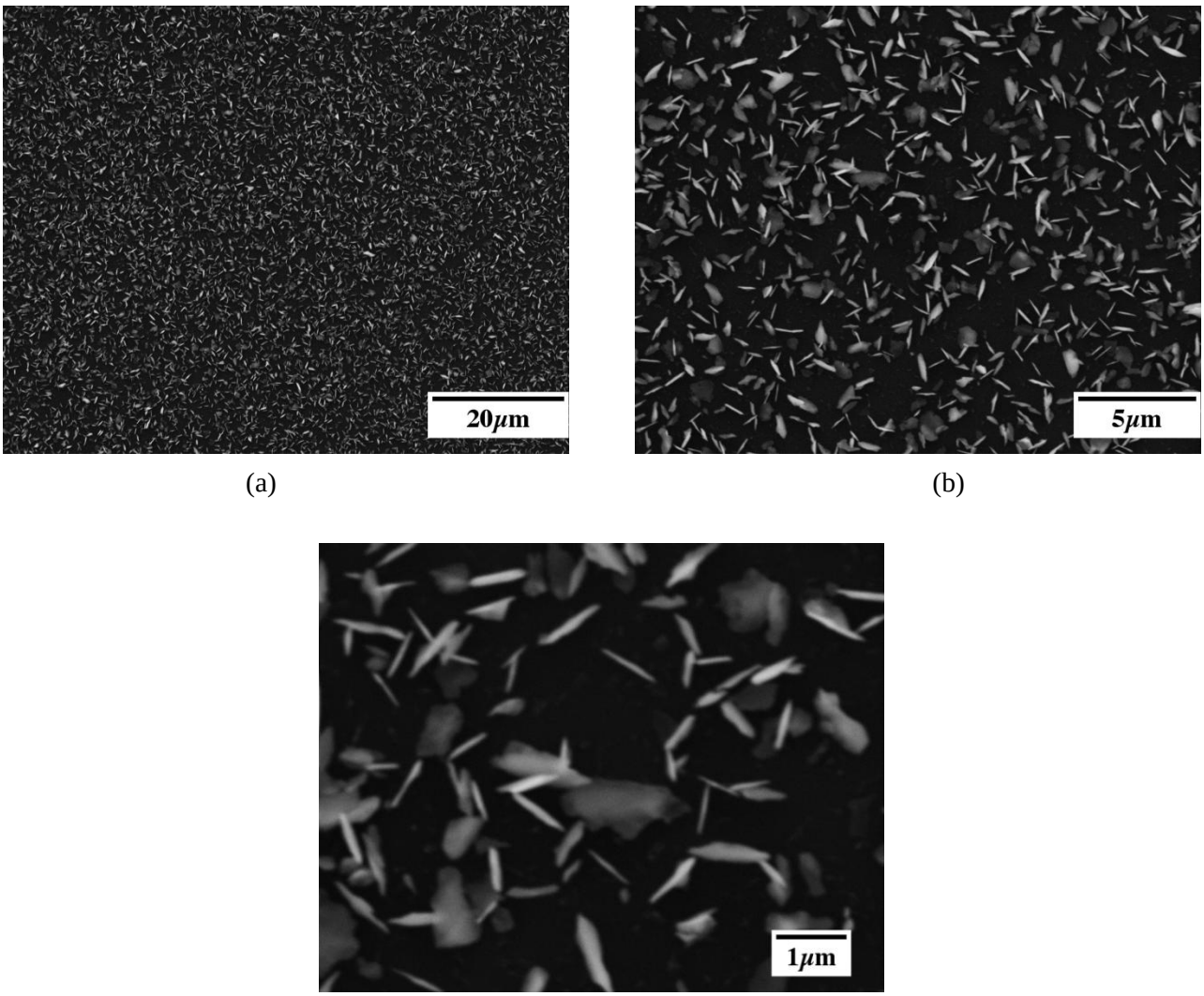

(a) (b)

(c)

Figure 5.7. Deposited hexagonl diamond under 10 Torr total deposition chamber pressure with Ar and CCl_4 partial pressures of 7 and 3 Torr respectively with Al/Ni/Al catalyst thin film thicknesses of 3/2/3 nm. The deposition temperature and time are 450 ˚C and 3 hours respectively.

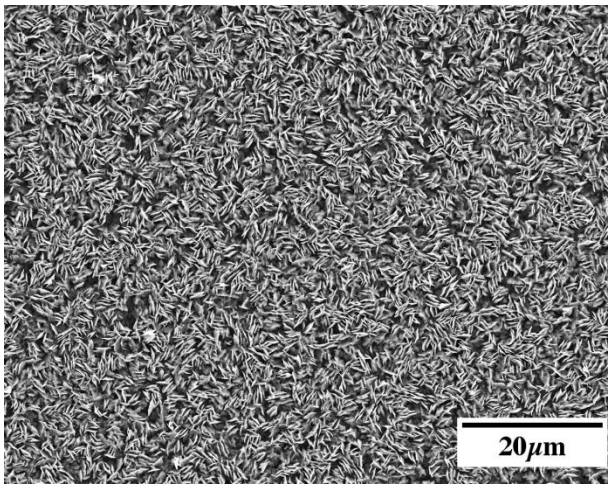

(a)

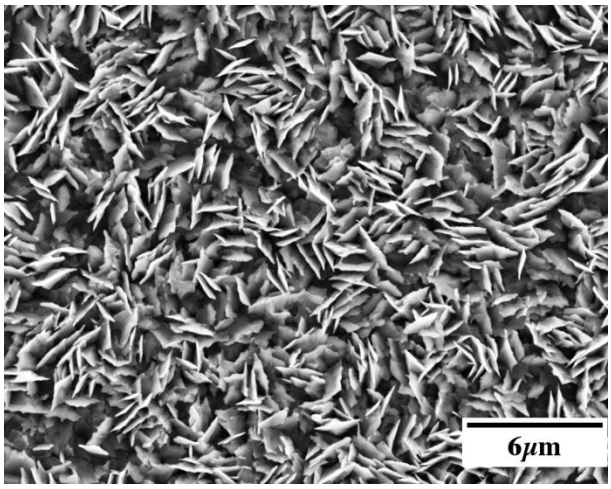

(b)

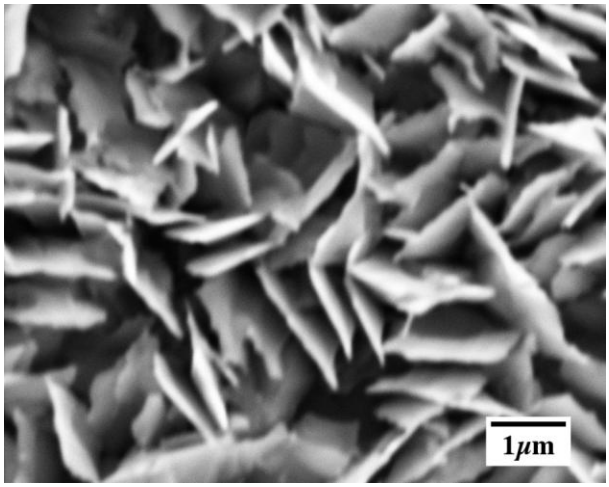

(c)

Figure 5.8 Deposited hexagonl diamond under 10 Torr total deposition chamber pressure with Ar and CCl_4 partial pressures of 7 and 3 Torr respectively with Al/Ni/Al catalyst thin film thicknesses of 5/1/5 nm. The deposition temperature and time are 450 ˚C and 3 hours respectively.

Figure 5.9 shows hexagonal diamond deposition on a sample with 5/3/5 nm thick Al/Ni/Al coated substrate. The deposition time is same as that for Figs. 5.7 and 5.8. This sample has the densest and fastest hexagonal diamond deposition. Figure 5.9 (a) shows a low magnification image of hexagonal diamond film. The hexagonal diamond film has poor adhesion on the SiO_2/Si substrate and the built-in stress causes the film to peel off from the substrate. The image in Fig. 5.9 (a) shows different substrate colors in area A and area B. Another hexagonal diamond film is subsequently deposited on area A but not on area B. The underlying area exposed by the peeled off film has nanoparticles remaining on the SiO_2/Si substrate. Figure 5.9 (b) is focused on the substrate in area A where the hexagonal diamond film has peeled off and where another layer of hexagonal diamond film is deposited under the peeled off film. In area B in Fig. 5.9 (a), it is anticipated that a new film will subsequently nucleate and grow as in area A. Figures 5.9 (c) and (d) show the top and bottom surfaces of hexagonal diamond film respectively. Another type of structure was observed on the top surface of hexagonal diamond film. These are small particles on top of the hexagonal platelets in Fig. 5.9 (c). From shape and morphology, it is presumed to be microcrystalline cubic diamond (MCD). However, MCDs were not found either on the bottom surface or the sparsely distributed hexagonal diamond deposited areas such as in Fig. 5.7. In this experiment, MDCs seem to be synthesized after hexagonal diamond growth is sufficiently dense. MDCs are not embedded in the hexagonal diamond film.

Figure 5.10 show images of hexagonal diamond deposited under 9 and 1 Torr partial pressure of Ar and CCl_4 on 5/1/5 nm thick Al/Ni/Al coated substrate for deposition time of 3 hours. Figure 5.11 shows images of hexagonal diamond deposited under 9 and 1 Torr partial pressure of Ar and CCl_4 on 5/3/5 nm thick Al/Ni/Al coated substrate for deposition time of 3

hours. Figure 5.12 shows images of hexagonal diamond deposited under conditions same as for Fig. 5.11 but for deposition time of 1.5 hours.

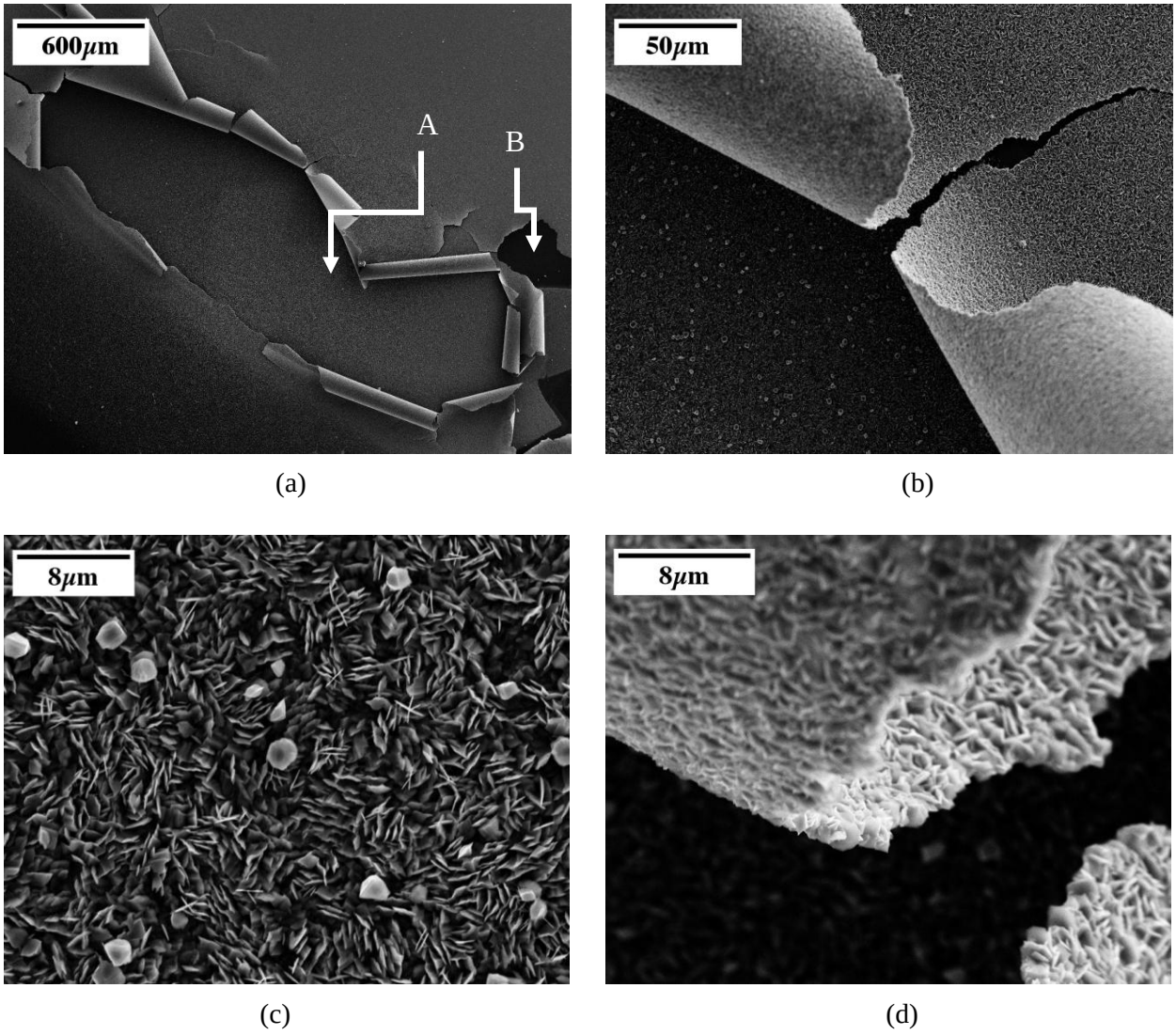

Figure 5.9. Deposited hexagonl diamond under 10 Torr total deposition chamber pressure with Ar and CCl_4 partial pressures of 7 and 3 Torr respectively with Al/Ni/Al catalyst thin film thicknesses of 5/3/5 nm. The deposition temperature and time are 450 ˚C and 3 hours respectively.

The deposited hexagonal diamond is clearly different depending on the partial pressure of Ar and CCl_4. The hexagonal diamond deposited under 9 and 1 Torr partial pressure of Ar and CCl_4 respectively has much less density than the one grown under partial pressure values of 7 and 3 Torr for Ar and CCl_4 respectively. With Ar to CCl_4 partial pressure ratio of 7:3, nucleation sites for hexagonal diamond is greater. This higher density of nucleation sites reduces the average distance between hexagonal diamonds. This closely packed hexagonal diamond interfere with neighbors during growth and build up film stress resulting in cracking of the film followed by peeling off. Thus the deposited hexagonal diamond under Ar:CCl_4 partial pressure ratio of 7:3 has thinner and samller size. However, the deposited hexagonal diamond under Ar to CCl_4 partial pressure of 9:1 has more clear structure and bigger size.

Figure 5.10 (a) shows clear structure of hexagonal diamond. Figure 5.10 (a) and (b) show different number of black spots in the middle of the hexagonal shape. These black spots are holes and are a result of the synthesis mechanism of hexagonal diamond. The detail of synthesis mechanism will be explained in chapter 6. The hexagonal diamond dimensions are approximate 2.5 μm wide, 1.2 μm tall and 50 nm thick. Figure 5.10 (c) shows that the deposited hexagonal diamonds make different angles to the oxide-coated substrate and some hexagonal diamond samples are seen to stand alone. The different standing angles are caused by the nucleation of hexagonal diamond. The comparison between Figs. 5.10 and 5.11 show that size and shape of deposited hexagonal diamond are very similar for the two cases with Fig. 5.11 showing denser deposited hexagonal diamond than Fig. 5.10. The only difference between the two samples is thickness of Ni catalyst which is 1 nm for Fig. 5.10 and 3 nm for Fig. 5.11. We observe similar results in Fig. 5.9 when hexagonal diamond is deposited under Ar to CCl_4 partial pressure ratio of 7:3. The thicker Ni catalyst results in more nucleation sites.

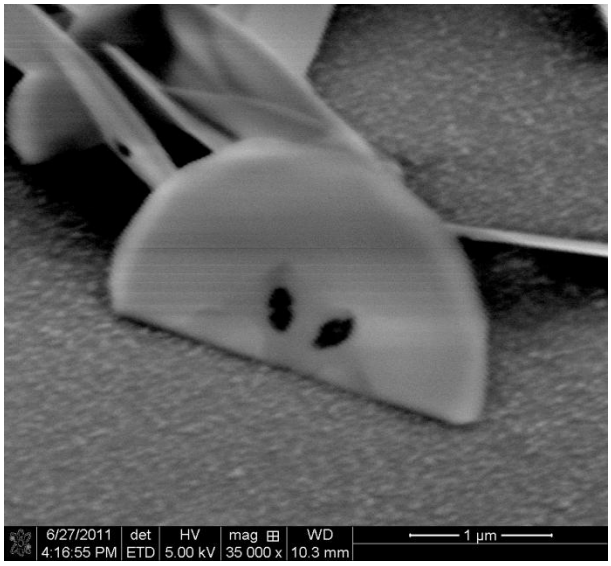

(a)

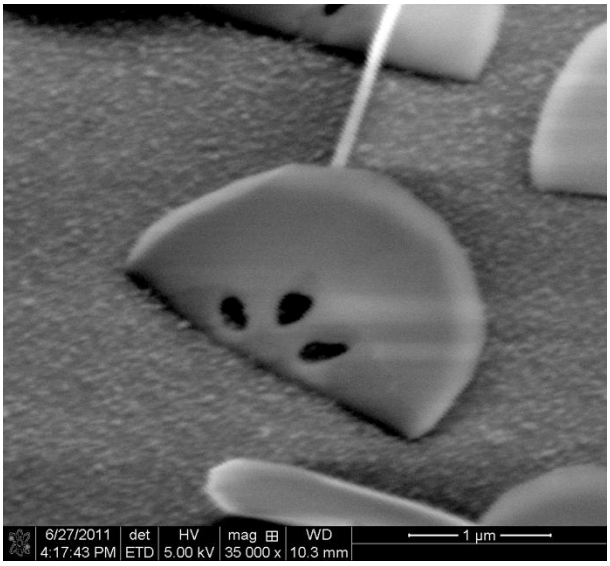

(b)

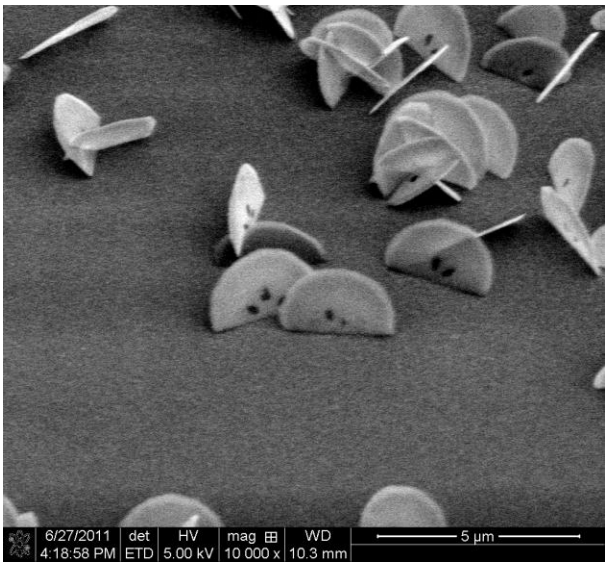

(c)

Figure 5.10. Synthesized hexagonal diamond under 10 Torr total deposition chamber pressure with Ar and CCl_4 partial pressures of 9 and 1 Torr respectively with Al/Ni/Al catalyst thin film thickness of 5/1/5 nm. The deposition temperature and time are 450 ˚C and 3 hours respectively.

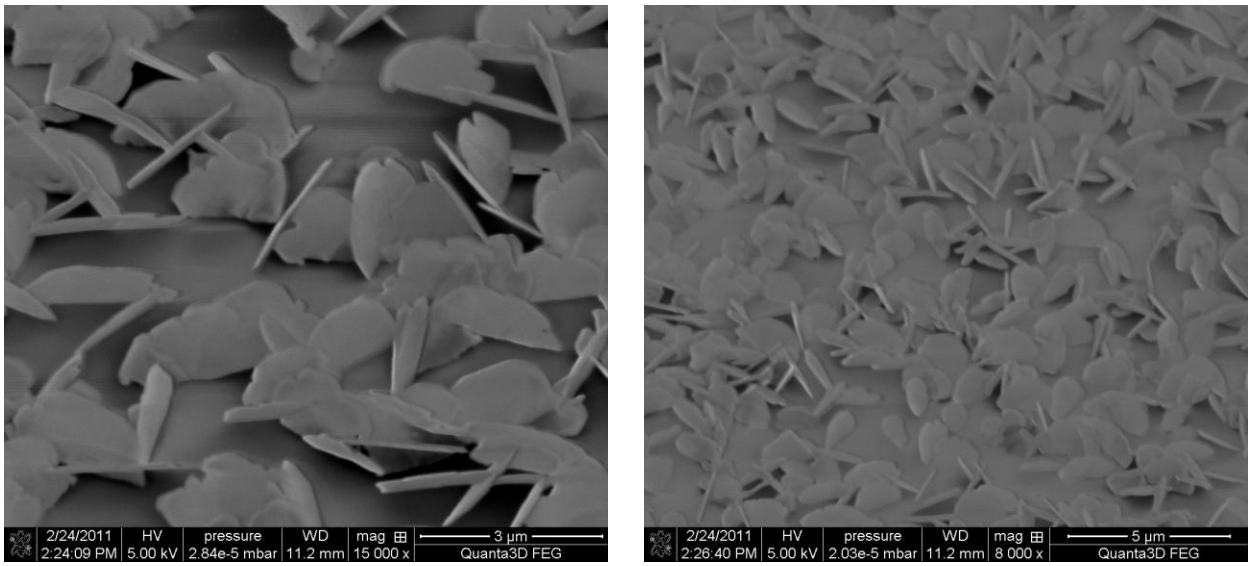

(a) (b)

Figure 5.11. Synthesized hexagonal diamond under 10 Torr total deposition chamber pressure with Ar and CCl_4 partial pressures of 9 and 1 Torr respectively with Al/Ni/Al catalyst thin film thickness of 5/3/5 nm. The deposition temperature and time are 450 ˚C and 3 hours respectively.

Three hour deposition process shows hexagonal diamond platelets with holes or fully grown crystal. However, there is no shape, size or thickness difference between having holes or fully grown hexagonal diamond. It means the growth of hexagonal diamond is terminated at a certain size and 3 hour deposition process is enough for deposition of hexagonal diamond in our experiment. It is hence difficult to find out the growth procedures of hexagonal diamond with 3 hour deposition time. Reducing deposition time from 3 to 1.5 hours gives various shapes and intermediary structures of hexagonal diamond during growth. Figure 5.12 shows intermediary shapes of samples during growth. Figure 5.12 (a) shows two different growing platelets of hexagonal diamond. The larger structure in the foreground in Fig. 5.12 (a) is at a more advanced stage of growth compared to the smaller upright structure. Figure 5.12 (b) shows a structure at a more advanced stage in the growth than Fig. 5.12 (a). Figure 5.12 (c) indicates the thickness of the grown hexagonal diamond platelet, which is approximately in the range of 50 - 80 nm. The details of hexagonal diamond growth mechanism will be explained in chapter 6.

5.3 Chapter Summary

CNT and hexagonal diamond deposition utilizing photo-enhanced CVD at relatively low substrate temperature is reported in this chapter. Deposition results under various conditions are reported. The CNT and hexagonal diamond deposition is affected by the total chamber pressure, partial pressure of Ar and CCl_4, deposition time, substrate temperature and catalyst layer thicknesses. CNT can be observed at lower chamber pressure, lower partial pressure of CCl_4, lower substrate temperature and thin Ni catalyst. The best CNT deposition condition is 5 Torr total chamber pressure, 9 to 1 partial pressure ratio of Ar to CCl_4, 400 ˚C substrate temperature and 5/1/5 nm thick catalyst film. The hexagonal diamond can be observed at higher chamber pressure, higher partial pressure of CCl_4, higher substrate temperature and thicker Ni catalyst.

The optimized condition for hexagonal diamond deposition in this work is 10 Torr total chamber pressure, 7 to 3 partial pressure ratio of Ar to CCl_4, 450 ˚C substrate temperature and 5/3/5 nm thick catalyst sandwich layer.

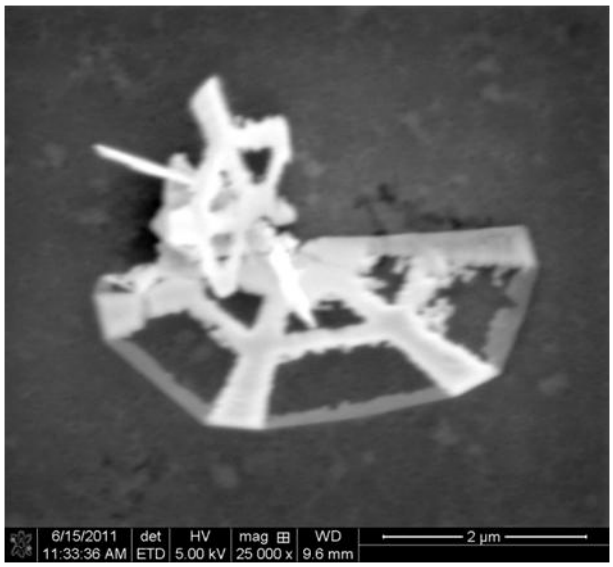

(a)

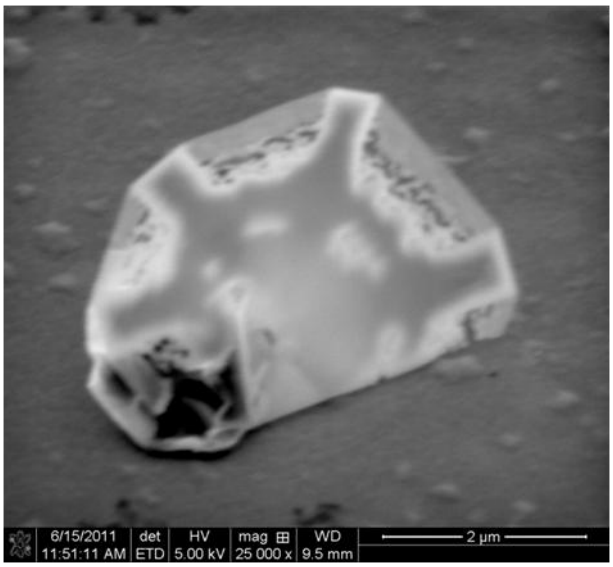

(b)

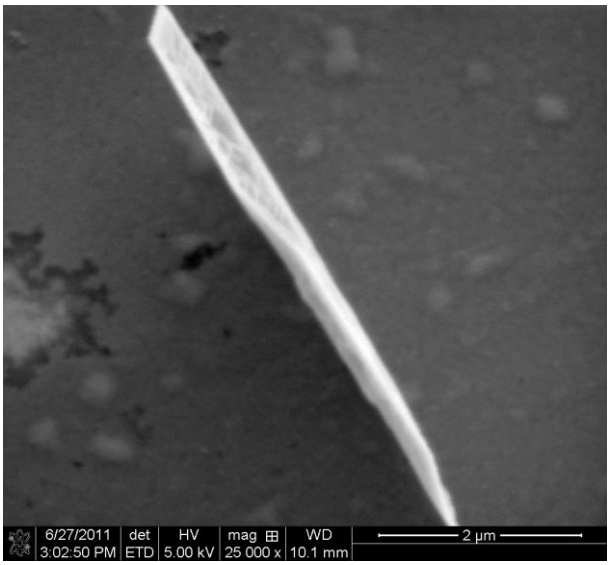

(c)

Figure 5.12. Synthesized hexagonal diamond under 10 Torr total deposition chamber pressure with Ar and CCl_4 partial pressures of 9 and 1 Torr respectively with Al/Ni/Al catalyst thin film thickness of 5/3/5 nm. The deposition temperature and time are 450 ˚C and 1.5 hours respectively.

CHAPTER 6. CHARACTERIZATION OF GROWN CNT AND HEXAGONAL DIAMOND

Carbon has three hybridizations, namely, sp, sp^2 and sp^3. These different hybridizations make various carbon allotropes and result in their own unique properties. CNT and hexagonal diamond has sp^2 and sp^3 hybridization, respectively. There are plenty of references on CNTs including their growth methods, growth mechanisms, and their electrical and mechanical properties. These experimental and theoretical reports reveal the properties of CNTs. Geometrically, the CNTs are classified as single wall or multi-wall in structures. Semiconductor and metallic properties of CNTs depend on the structure of carbon atoms. Mechanically, CNTs have high values for Young's modulus and hardness. However, limited information is currently available on hexagonal diamond because of the difficulties in synthesizing this material. Thus the reports on hexagonal diamond properties are mainly from simulation. Furthermore, the growth procedure and mechanism of hexagonal diamond formation are still not well understood. Therefore, more explanations and measurements on hexagonal diamonds are needed.

In this chapter, various measurement results are provided. Raman spectroscopy results are provided to identify CNT and hexagonal diamond structures. XRD and XPS data are provided to verify the hexagonal diamond structure. A possible mechanism for nucleation and synthesis for the hexagonal diamond is provided based on SEM images. Lithography based I-V curve is measured for electrical property of CNT sample. Young's modulus and I-V curve of hexagonal diamond are measured with nano-indentation equipment. The color and UV-Visible transmittance of hexagonal diamond can be observed by using glass substrate for hexagonal diamond deposition. The optical band gap of hexagonal diamond is calculated using Tauc plot.

6.1 A Proposed Model for Hexagonal Diamond Growth

Some of the work given in sections from 6.1.1 to 6.1.3 has been reported elsewhere [89].

6.1.1 SEM Images of Hexagonal Diamond Formation

Figure 6.1 shows SEM pictures at different stages of hexagonal diamond platelet growth. These progression images of hexagonal diamond formation provide a clue for mechanism of its growth. Figure 6.1 (a) corresponds to an early stage of the hexagonal diamond formation consisting of radial spokes like frame structures. Figure 6.1 (b) shows what is presumed to be formation of graphene layers along the peripheral directions starting from the edges of the radial frame structures. This presumption is based on the differences between the observed morphology of this thin layer and the subsequent thicker grown layer above it. The hexagonal diamond-graphene layer hybrid structure has been examined in some detail elsewhere [90–92]. Comparing Figs. 6.1 (b) to 6.1 (a), it is apparent that the growth in the radial direction of the hexagonal diamond occurs first followed by synthesis of presumably several layers of graphene along the peripheral directions providing a hexagonal boundary shape. The inner peripheral layer is completed in Fig. 6.1 (b) creating empty space between two adjoining radial arms. Figure 6.1 (c) shows the connection of two radial arms with layers of graphene. Although these peripheral layers of graphene grow from two different radial arms, there does not appear to be a discontinuity in the connected graphene layers. This indicates that the lengths of the adjoining diagonal frames are equal and the angles between the diagonal frame on either side and the graphene layers forming on that side are also the same. This is consistent with the assumption that the starting point of the hexagonal diamond platelet growth is at the center and the growth rate of each radial arm is same. Figure 6.1 (d) is a more detailed image than Fig. 6.1 (c) and shows filling of empty spaces between the peripheral layer and the diagonal arms. The proposed

mechanism stipulates growth of graphene layers first as indicated in Fig. 6.1 (c). The bond length of hexagonal diamond projected on (0001) plane is 1.45 Å which matches closely to bond length in graphene of 1.42 Å. Figure 6.1 (e) shows the difference between graphene layer structures and the overlaying connecting structures. The graphene layer structures appear to be smooth and flat but the structure connecting the adjacent graphene layers or overlaying the graphene layers appears coarse and somewhat rougher. This difference is attributed to the 2-dimensional (graphene) and 3-dimensional (hexagonal diamond) structures. It shows that when hexagonal diamond grows to cover the few layers of graphene structure, the formation starts from the edge of the graphene layer structure and not from the inside. Thus the graphene layer structure enhances and helps the growth of hexagonal diamond. Figure 6.1 (f) shows an almost filled up hexagonal diamond platelet.

Figure 6.1. SEM images at different stages of hexagonal diamond formation. (a) early stage of hexagonal diamond platelet growth, (b) early stage of graphene layer(s) formation, (c) connection of radial spokes with graphene layer(s), (d) beginning stage of spaces filling up, (e) more filled up stage and (f) almost filled up hexagonal diamond platelet. The scale bar shown in a, d and e is 1 μm long and that in b, c and f is 2 μm long.

(a)

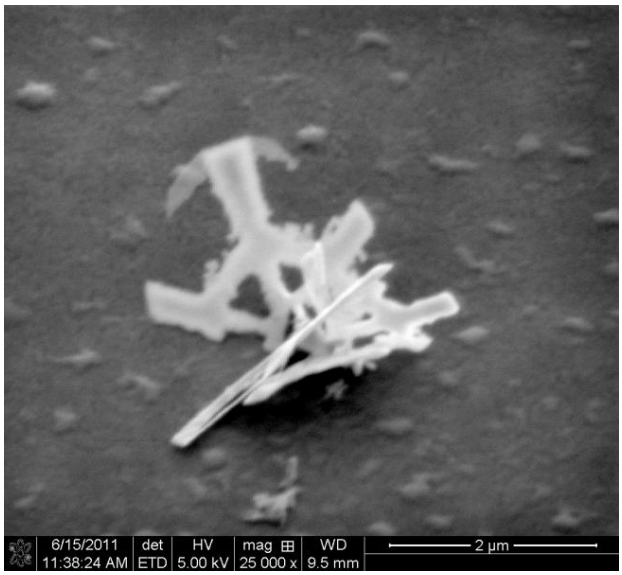

(b)

Fig.6.1 continued.

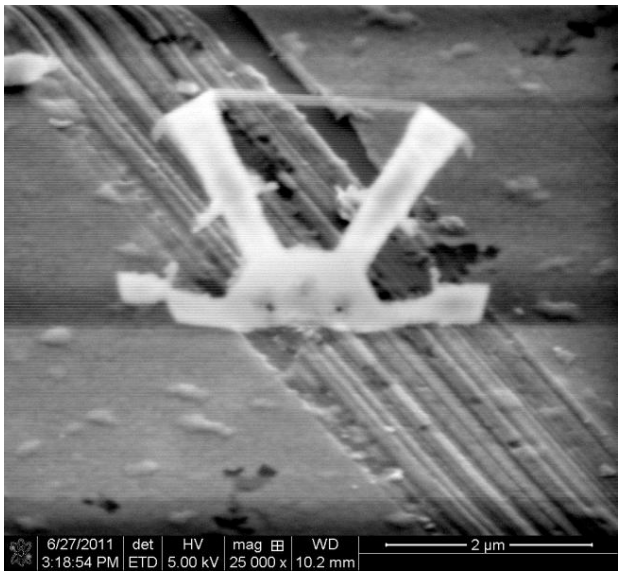

(c)

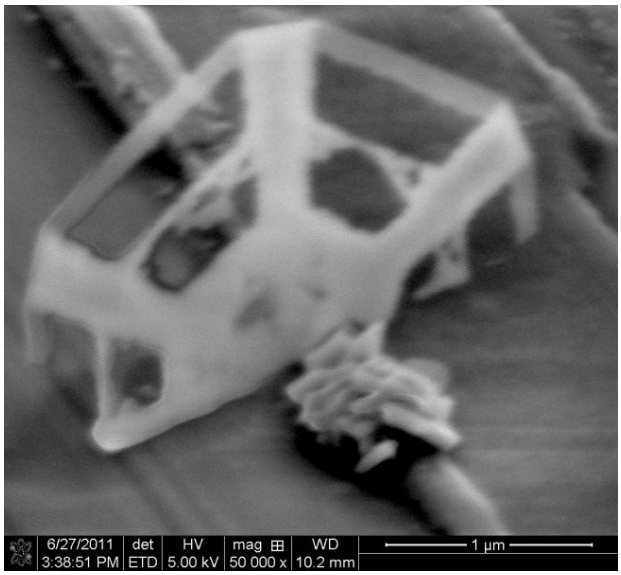

(d)

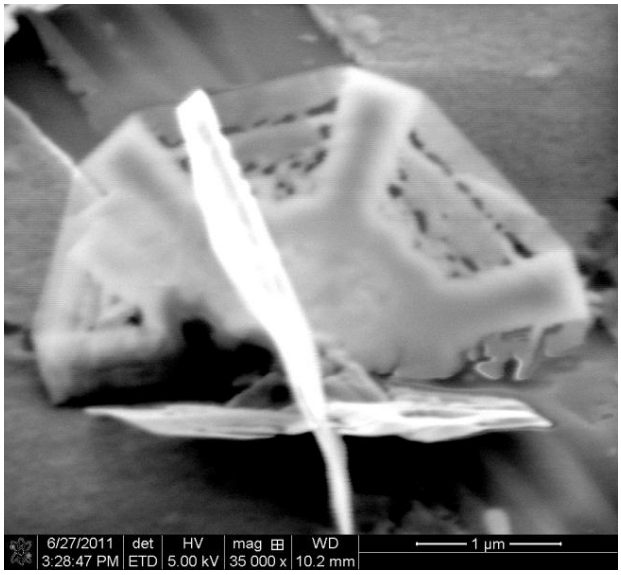

(e)

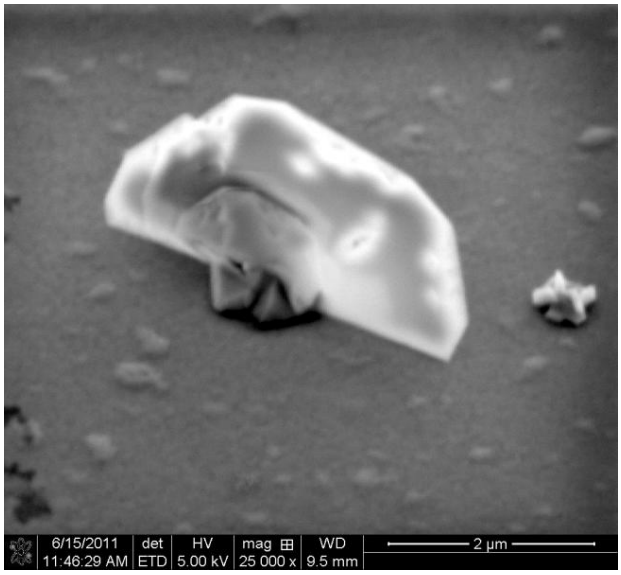

(f)

6.1.2 A Proposed Model for Nucleation of Hexagonal Diamond

Figure 6.2 shows schematic diagrams of a possible mechanism for the observed hexagonal diamond formation process. When the catalyst deposited sample is annealed, the thin catalyst film layer changes to nanoparticles. An amorphous carbon film is formed prior to hexagonal diamond formation. This carbon film plays a critical role in synthesizing hexagonal diamond. Xu *et al*. showed that fullerene encapsulates Al nanoparticle and that Al nanoparticle improves formation of fullerene [93]. Thus, it is reasonable to assume that amorphous carbon layer first covers the Al/Ni nanoparticle on the substrate and begins to form a fullerene on the Al/Ni nanoparticle. Figure 6.2 (a) shows a schematic diagram of hexagonal diamond nucleation on a catalyst nanoparticle covered with onion-like fullerene with the CVD method. Figures 6.2 (a) and 6.2 (c) show perfect half-spheres for convenience even though the shapes of nanoparticles formed during annealing need not be perfect half-spheres. The geometric size of the graphene layer is determined from carbon-carbon bond length of 1.42 Å and a hexagonal lattice parameter of 2.46 Å. The carbon-carbon bond length of fullerene increases with the size of the fullerene [14]. If the size of fullerene is increased, nano-diamond structure is more stable than that of the fullerene of a larger size [77]. Thus, there is a critical point on the nanoparticle enclosed by the fullerene where the energy is no longer stable and the nucleation of diamond is initiated on the fullerene. Figure 6.2 (b) is a SEM image of synthesized hexagonal diamond platelets having different standing angles with the substrate surface. These standing angles are related to the location of seed atom on the fullerene as indicated in Fig. 6.2 (c). If the seed atom is located near the bottom of the fullerene, then the standing angle of hexagonal diamond platelet will be close to the perpendicular to the substrate surface. If the seed atom bond is close to the top of the fullerene, then the angle of hexagonal diamond platelet is almost parallel to the substrate surface.

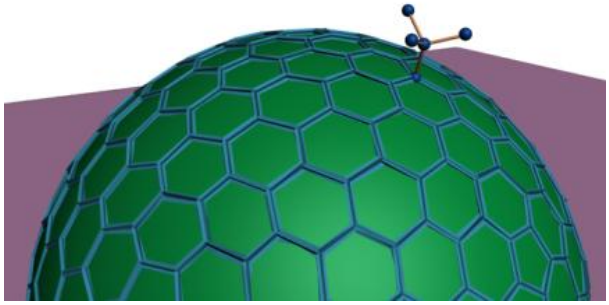

(a)

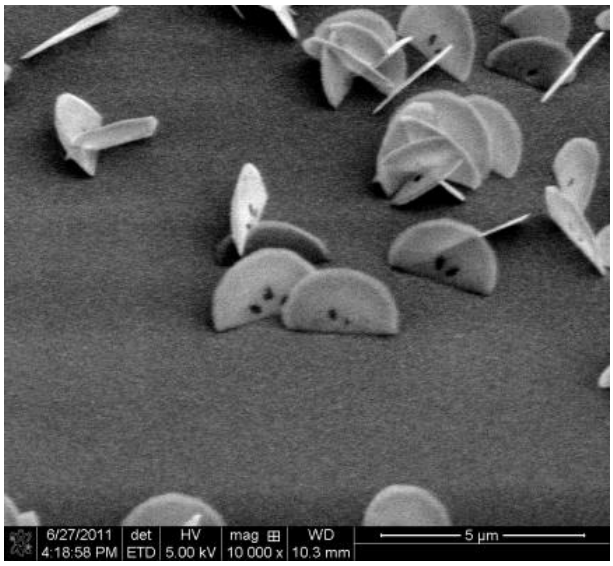

(b)

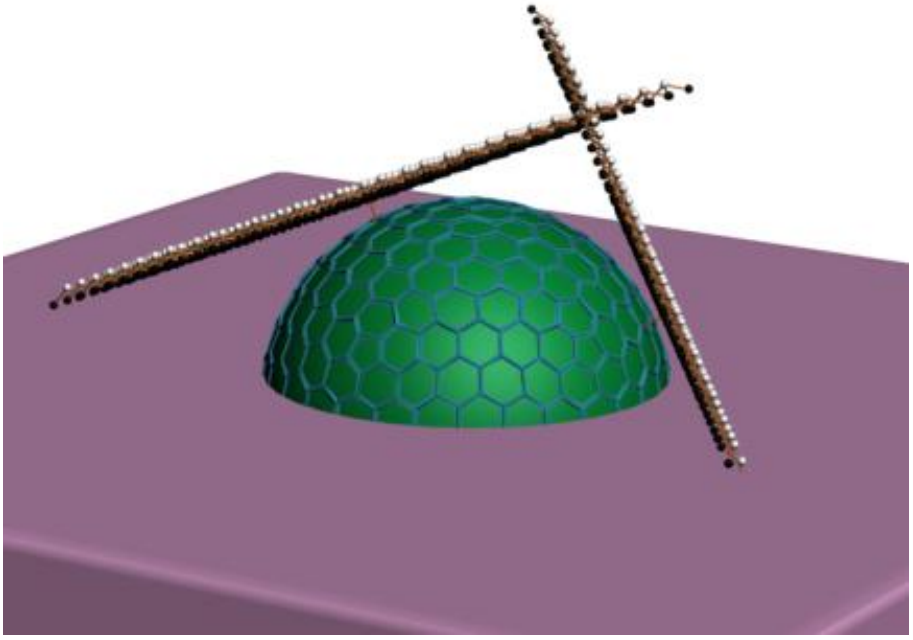

(c)

Figure 6.2. (a) Hexagonal diamond nucleation, (b) various standing angles of hexagonal diamond platelets and (c) schematic diagram of various standing angle formation. The scale bar shown in b is 5 µm long.

6.1.3 Hexagonal Diamond Synthesis Mechanism

Figures 6.3 (a)-(c) depict top views of hexagonal diamond formation process with a seed carbon atom or atoms. The open and filled circles represent carbon atoms projected on the (0001) plane of hexagonal diamond. The open circles are carbon atoms that are closer to the (0001) surface than the filled circles. The filled circles at the center of Figs. 6.3 (a)-(d) are seed atoms. Figure 6.3 (a) is a schematic diagram of hexagonal diamond formation process with one seed atom. The seed carbon atom forms a covalent bond with another carbon atom and the latter forms three more covalent bonds with three other carbon atoms as a follow-up step. These three carbon atoms form an equilateral triangle. These three atoms need to make nine more bonds with neighboring carbon atoms. Since three carbon atoms are bonded perpendicularly to the surface, six carbon atoms form an equilateral hexagonal shape. This step will be repeated and the hexagonal formation continues to grow. Figures 6.3 (b) and 6.3 (c) respectively are schematic diagrams corresponding to two and three seed atoms resulting into defect free hexagonal diamond formation procedure. The shape of hexagonal diamond will depend on the number of seed atoms. If there is no defect during the growth of hexagonal diamond, the final shape of hexagonal diamond will be the same as illustrated in these figures. However, we did not find a perfectly synthesized hexagonal diamond in this work. All hexagonal diamonds in images of Fig. 6.1 have defects. Figure 6.3 (d) is a schematic diagram of hexagonal diamond formation with one seed atom that has defects. In general, the defects will occur at carbon atom locations at the corners of the growing hexagonal shape. The missing carbon atoms at the corners along with subsequent carbon atoms, which would have been connected to the missing carbon atom, give rise to empty space in the structure while the radial arms along the six sides continue to grow. Theoretically, the edges of the missing hexagonal corner carbon atoms make a 60˚ angle and form an equilateral triangle with the peripheral boundary. The open and black solid circles

Figure 6.3. Schematic diagrams for growth of hexagonal diamond structure: Defect free growth progression with (a) one seed atom, (b) two seed atoms, (c) three seed atoms, (d) growth with one seed atom with defects, (e) front oblique view of hexagonal diamond and graphene interface, (f) side oblique view of hexagonal diamond and graphene interface, (g) magnified of front oblique view of hexagonal diamond and graphene interface, (h) magnified side oblique view of hexagonal diamond and graphene interface and (i) a tilted regular hexagonal superimposed on a SEM image. The scale bar in (g) is 1 μm long.

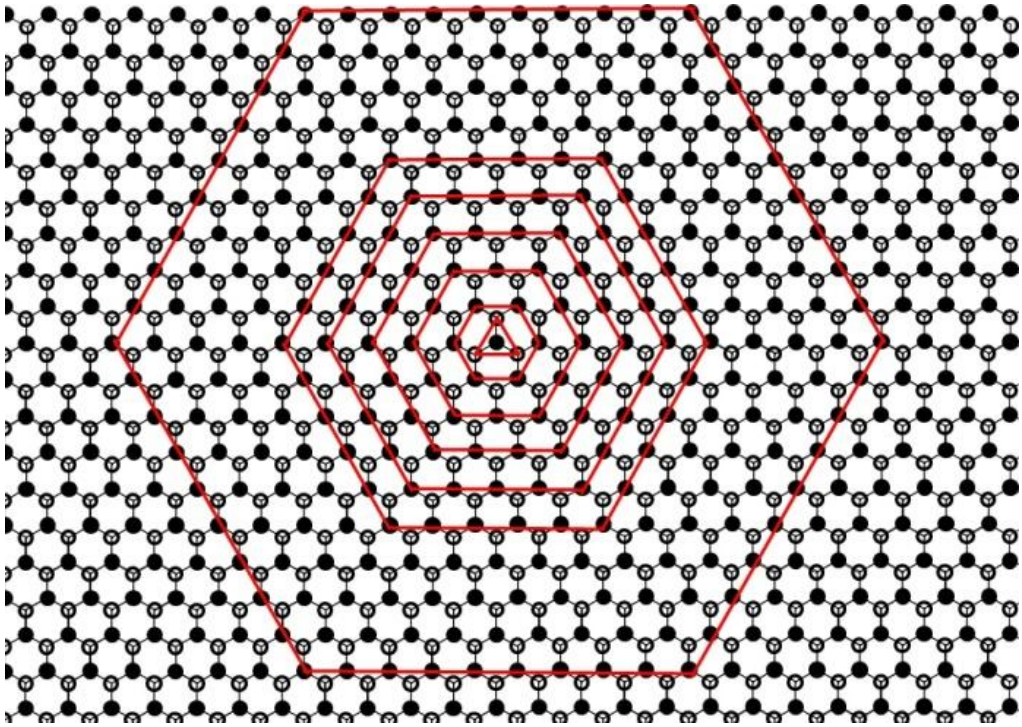

(a)

Figure 6.3 continued

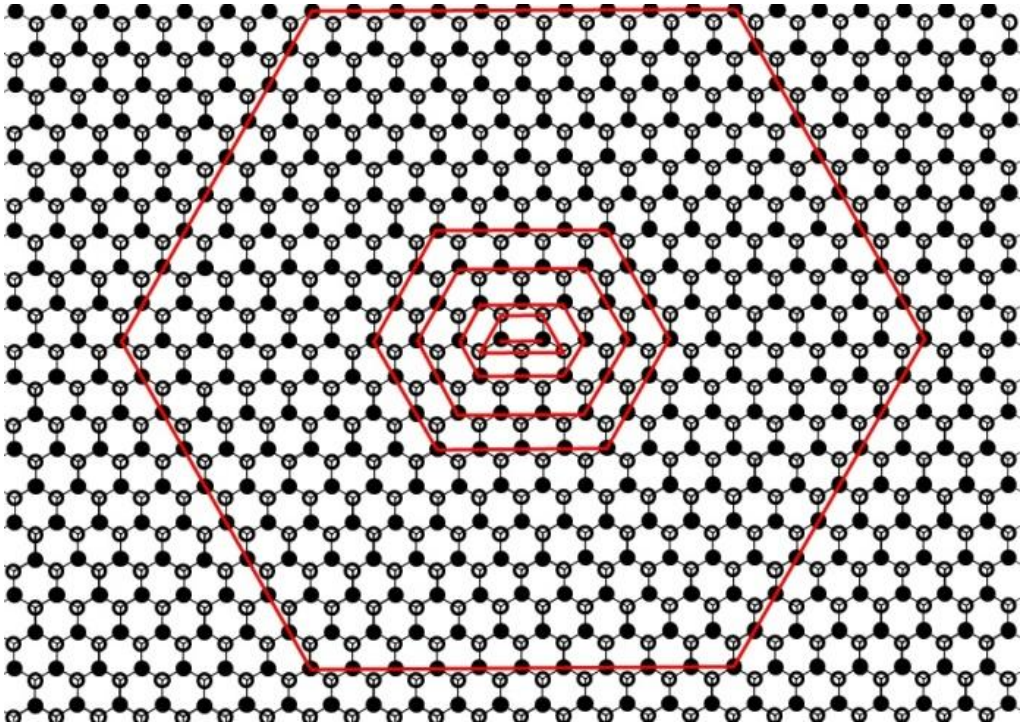

(b)

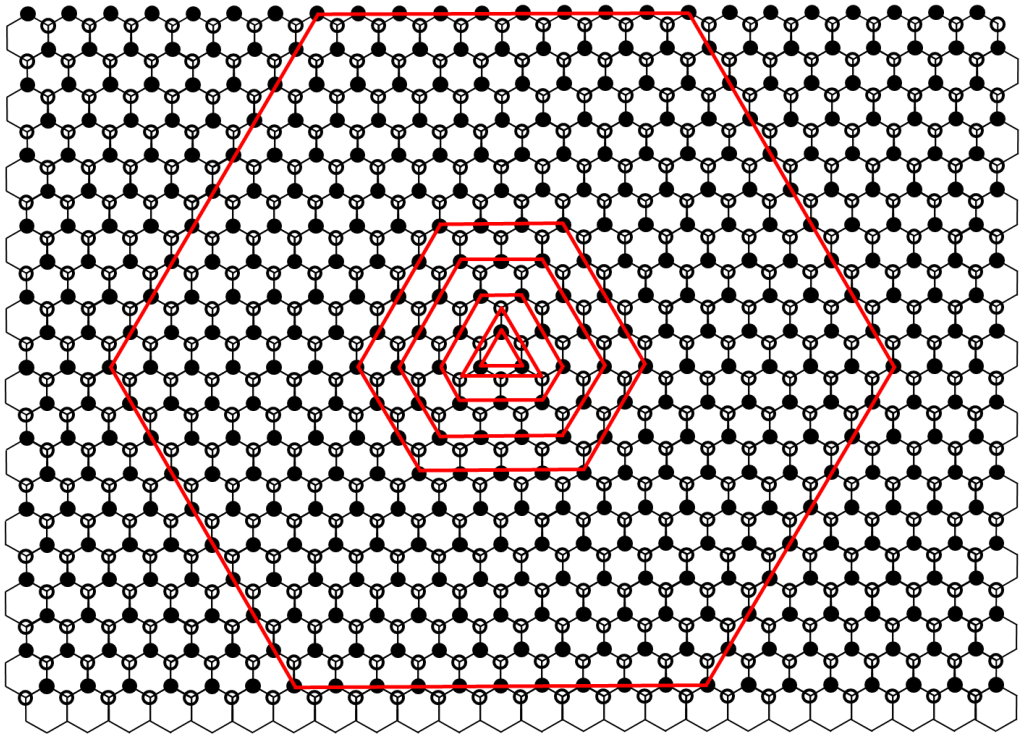

(c)

Figure 6.3 continued

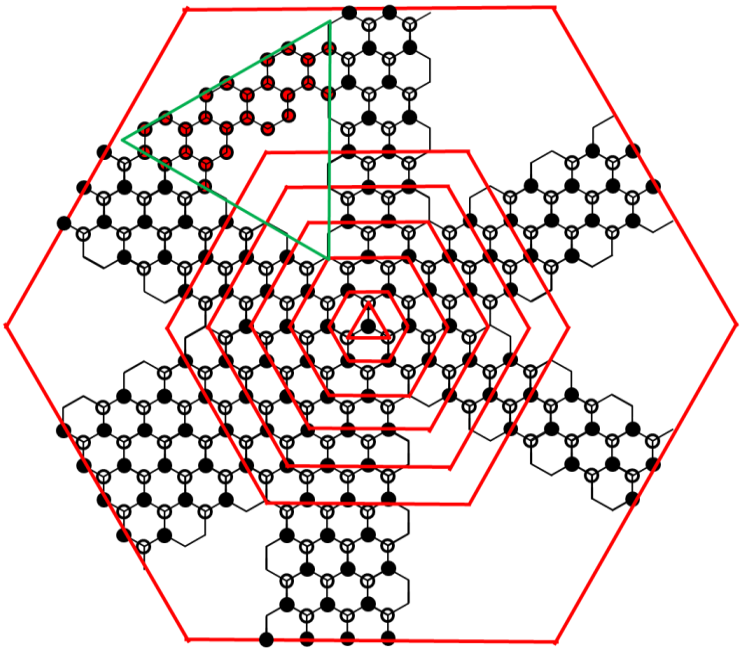

(d)

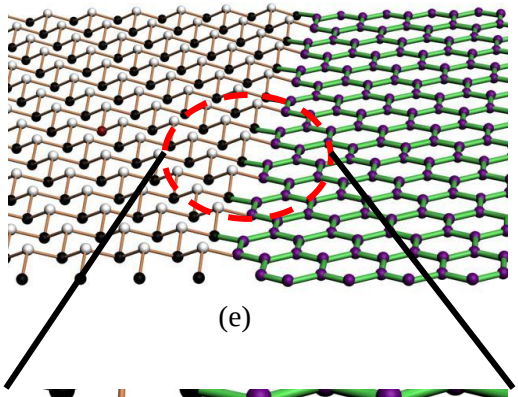

(e)

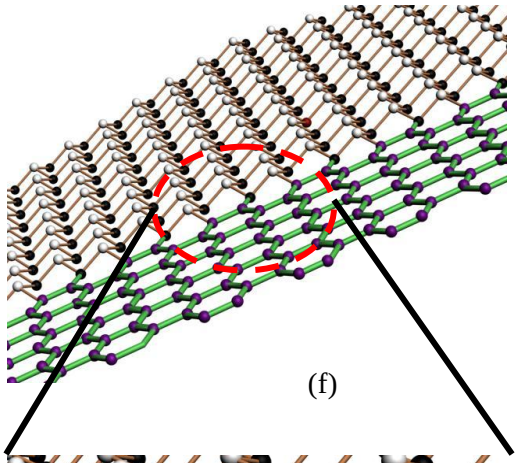

(f)

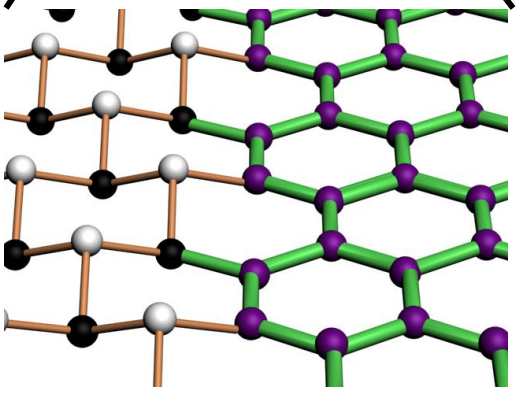

(g)

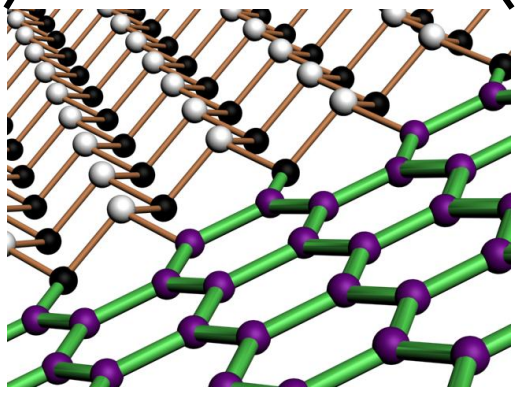

(h)

Figure 6.3 continued

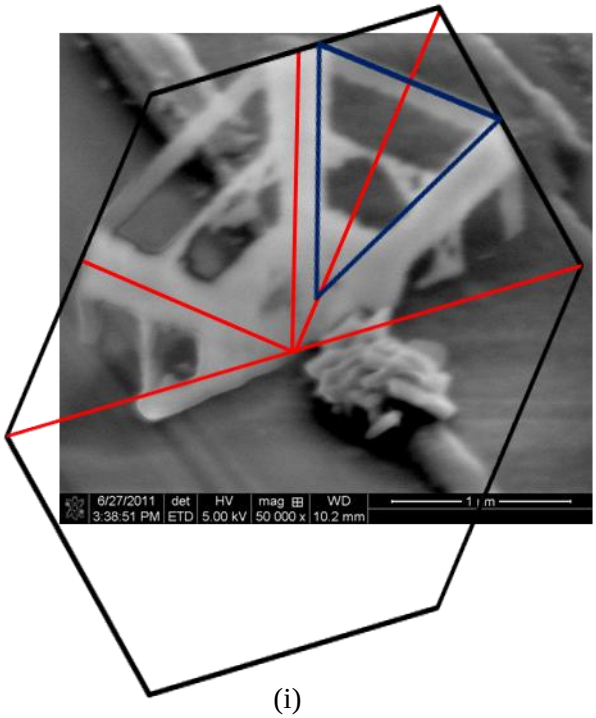

(i)

represent projected hexagonal diamond structure on (0001) plane and red filled circles in Fig. 6.3 (d) represent the graphene layer structure. Figure 6.3 (e) and (f) show the hexagonal diamond and graphene hybrid structure. The brown and green connections represent hexagonal diamond and graphene respectively. The (0001) plane of hexagonal diamond projection has 2% larger bond length than that of graphite. This small difference of bond length minimizes interface strain between hexagonal diamond and graphene. Figure 6.3 (g) and (h) show the interface of hexagonal diamond and graphene layer at higher magnifications. In figure 6.3 (i), a tilted regular hexagonal shape and an equilateral triangle are superimposed on a SEM image of a grown hexagonal diamond platelet. Since the sketched regular hexagonal shape does not match accurately to the hexagonal diamond structure in Fig. 6.3 (i), the latter does not appear to have

resulted from a single seed carbon atom corresponding to Fig. 6.3 (a). The angle between the two radial diagonal spokes in Fig. 6.3 (i) is approximately 60˚ attributed to the difference in the carbon-carbon bond length for hexagonal diamond and for fullerene. The seed carbon atoms are bonded to the fullerene, thus the bond length between the seed atoms and the fullerene is close to the bond length of fullerene. However, the bond length of hexagonal diamond will keep increasing until it reaches 1.54 Å and when the carbon atoms are projected to the (0001) plane, the bond length will be 1.45 Å.

6.2 Hexagonal Diamond Characterization

6.2.1 Raman Spectroscopy of Hexagonal Diamond

Raman spectroscopy is a useful method to characterize carbon materials. Since different carbon allotropes show different Raman spectra peaks. Single crystal of graphite has a peak approximately at 1580 cm^{-1} (G band). However, sp^2 carbon materials generally show D and G band at the same time. The D band appears around 1350 cm^{-1} and is the disorder-induced band of sp^2 carbon materials. In general, Raman spectra peaks of hexagonal diamond can be distinguished from the peaks of cubic diamond. Cubic diamond has a single peak at approximately 1332 cm^{-1} and a narrow FWHM value while hexagonal diamond shows a single peak between 1315 ~ 1326 cm^{-1} [94] and a broad FWHM value.

Figure 6.4 is Raman spectra of hexagonal diamond sample grown in this work. Raman spectra were measured on a LABRAM Integrated Raman Spectroscopy System. A 632.81 nm HeNe laser is used as the excitation source. The Raman spectra in Fig. 6.4 show a peak at 1322 cm^{-1} with a FWHM value of 75.4 cm^{-1}. This peak and FWHM indicate that the sample grown is a hexagonal diamond [95].

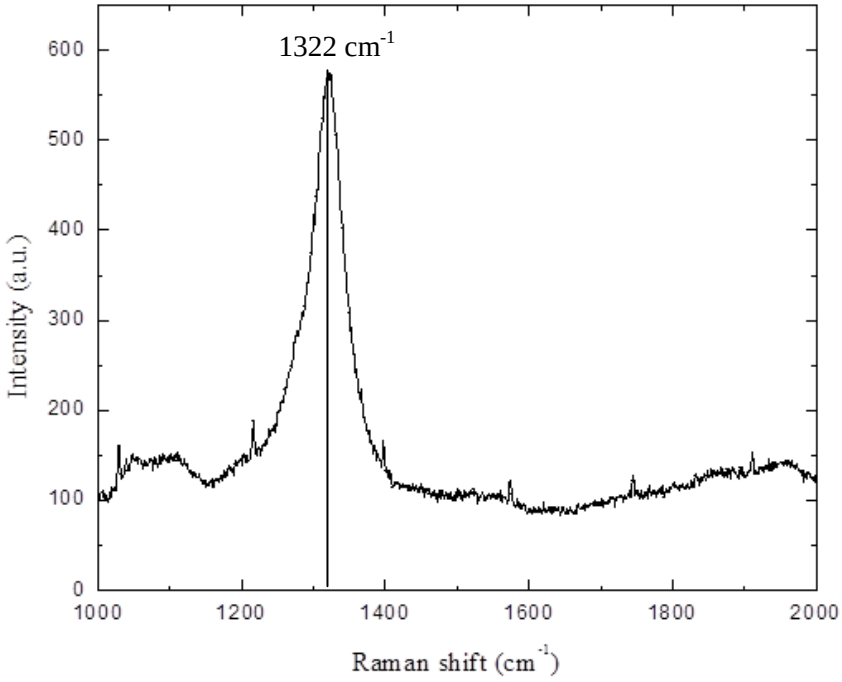

Figure 6.4. Raman spectroscopy of hexagonal diamond using 5/1/5 nm catalyst substrate. The deposition condition is 450 C substrate temperature, 3 hour deposition time, 10 Torr total chamber pressure with 7 Torr and 3 Torr partial pressures of Ar and CCl_4 respectively.

6.2.2 XPS of Hexagonal Diamond

XPS spectra were measured on a Kratos AXIS-165 XPS/Auger surface analysis system. Figure 6.5 shows high resolution XPS spectra corresponding to C_{1s} region indicating deconvoluted binding energy associated with the C_{1s} region. The gray-solid line is the raw data and two dotted blue lines are the decomposed graph from the original plot and red-broken line is the sum of two decomposed graph. C_{1s} peak is a result of 282.89 and 285.12 eV sub peaks. The 282.89 eV energy position peak arises due to aluminum carbide and the peak appearing at 285.12 eV is due to C-C sigma bond of diamond. In general, C=C double bond is obtained at around 284.4 eV but it is not observed in our sample. Therefore, it indicates that the deposited thin film

is composed of mainly C-C sigma bond consistent with both hexagonal and cubic diamond structures.

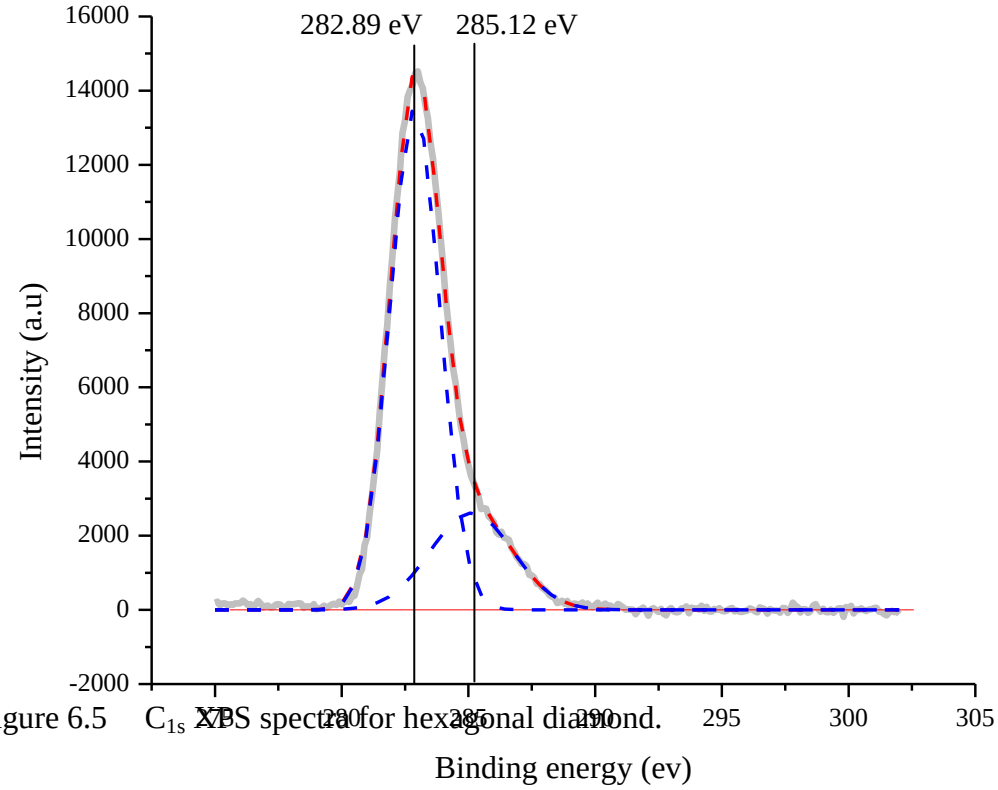

Figure 6.5 C_{1s} XPS spectra for hexagonal diamond.

6.2.3 X-Ray Diffraction (XRD) Spectroscopy

X-ray diffraction data is useful to define crystal structure by measuring interplanar spacing. X-ray diffraction measurements are made at the synchrotron ring at J. Bennett Johnston, Sr., Center for Advanced Microstructures and Devices (CAMD), Louisiana State University with monochromatic x-ray wavelength of 1.48 Å.

Figure 6.6 shows the XRD data taken on the grown samples. The peak at 23.5˚ corresponds to 0.363 nm interplanar spacing which is close to 0.36 nm of carbon onion d-spacing

[96]. The two peaks at 31.8 and 34.2 degrees correspond to 0.269 and 0.251 nm interplanar spacing, respectively, and they are close to 0.27 and 0.25 nm d-spacing of AlN (1100) and (0002) planes, respectively [97]. The presence of AlN peaks in the X-ray diffraction data is attributed to Al catalyst used along with NH_3 in the annealing cycle. The three peaks at 39.4, 47.7 and 59.5˚ correspond to 0.219, 0.189 and 0.149 nm interplanar spacing, respectively, which can be attributed to 0.219, 0.192, and 0.150 nm d-spacing of hexagonal diamond (100), (101) and (102) planes, respectively [98]. The peak at 52.1˚ with 0.168 nm of interplanar spacing is currently not identified.

6.2.4 Color of Hexagonal Diamond

The hexagonal diamond is deposited on a transparent glass substrate. The hexagonal diamond deposited on glass substrate shows a brownish-yellow color which is the same as other known samples of hexagonal diamonds [22]. Figure 6.7 is a photograph of hexagonal diamond film deposition on a glass substrate. The size of glass substrate is approximately 2 cm × 1.7 cm and the half circles on the top and bottom of glass substrate are locations for washers for mounting the substrate. The thickness of catalyst is 5/3/5 nm and the deposition temperature and pressure are 450 ˚C and 10 Torr total chamber pressure, respectively. The Ar and CCl_4 partial pressures are respectively 7 and 3 Torr. The deposited hexagonal diamond is similar to Fig. 5.9.

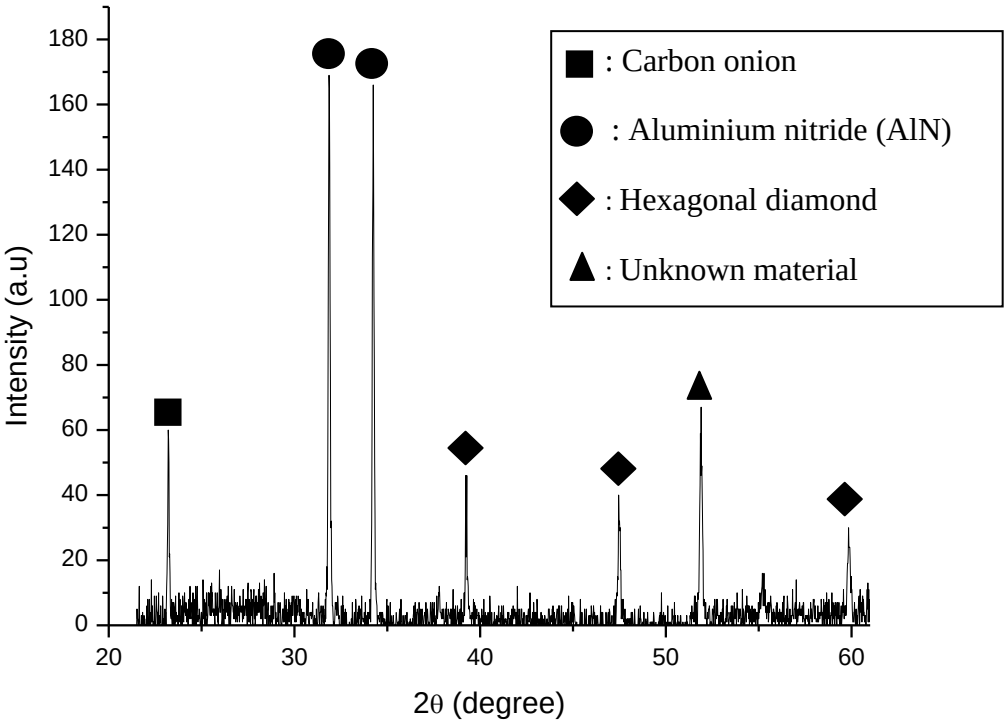

Figure 6.6. XRD spectra of hexagonal diamond.

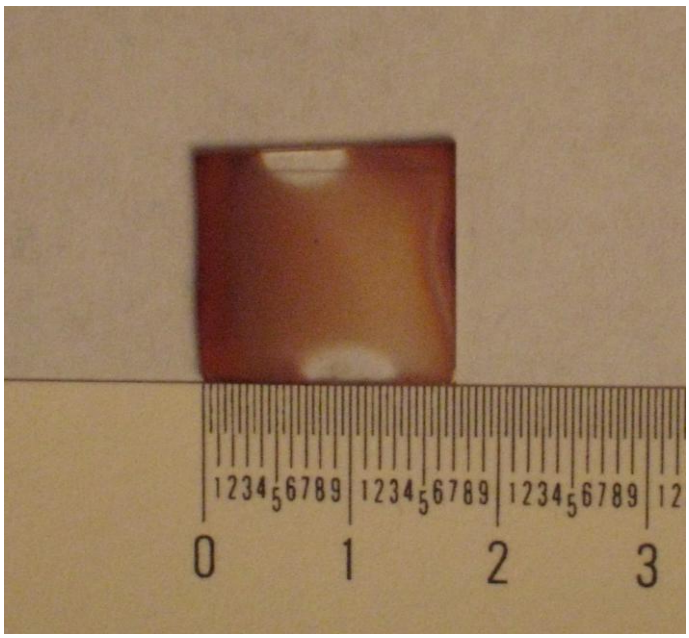

Figure 6.7. Hexagonal diamond deposition on a glass substrate. The major unit on ruler is in cm.

6.2.5 UV-Visible Spectroscopy of Hexagonal Diamond

UV-Visisible spectra are measured on a Varian Carry 50 spectrophotometer. Hexagonal diamonds deposited on a glass substrate is used to measure UV-Vis transmittance. Before the measurement on hexagonal diamond film, baseline transmittance of the machine and the substrate are made. The beam intensity is measured first in air for the baseline calibration of the machine and then transmittance through the catalyst deposited glass sample is measured. The transmittance of hexagonal diamond deposited sample is measured next and the baseline for the catalyst deposited glass is subtracted. Figure 6.8 is the net transmittance through the hexagonal diamond on the glass substrate. The transmittance data can be utilized for optical band gap of thin film by employing the Tauc plot. The electronic band gap of cubic diamond and hexagonal diamond is 5.5 and 4.1 eV, respectively [25], [99]. The electronic band gap of cubic diamond is an experimental value and the value for the hexagonal diamond is based on theoretical simulation. Figure 6.9 shows optical band gap of our sample obtained from the Tauc plot and the value is approximately 1.0 eV. Here, α is absorption coefficient calculated from the transmittance data of hexagonal diamond on glass substrate and $h\nu$ is photon energy. The measured approximate value of the hexagonal diamond film thickness in this case is 1 μm. The optical band gap of cubic diamond varies from 0.2 to 5.54 eV depending on the defect of crystal, ratio of sp^2 hybridization and impurities [100–103]. Table 6.1 shows the optical band gap values for various cubic diamond films and structures. The measured hexagonal diamond sample is as-grown without impurity doping. The observed optical band gap of as-grown nanocrystalline or polycrystalline cubic diamond is observed between 1.5 and 2.2 eV. The optical band gap of hexagonal diamond sample grown in this work is 0.5 to 1.2 eV lower than that observed on nanocrystalline cubic diamond. This difference in the electronic band gap appears reasonable for the two types of diamond structures.

Table 6.1. Measured optical band gap for various cubic diamond samples.

Material condition	Optical band gap (eV)	Reference
Nanocrystalline diamond without nitrogen	2.2	[100]
Nanocrystalline diamond with 5% nitrogen	0.6	
Nanocrystalline diamond with 10% nitrogen	0.5	
Nanocrystalline diamond with 25% nitrogen	0.2	
Polycrystalline and nanocrystalline diamond	2.0	[101]
Microcrystalline diamond	5.54	[102]
Nanocrystalline diamond	2	
Nanocrystalline diamond	1.5	[103]

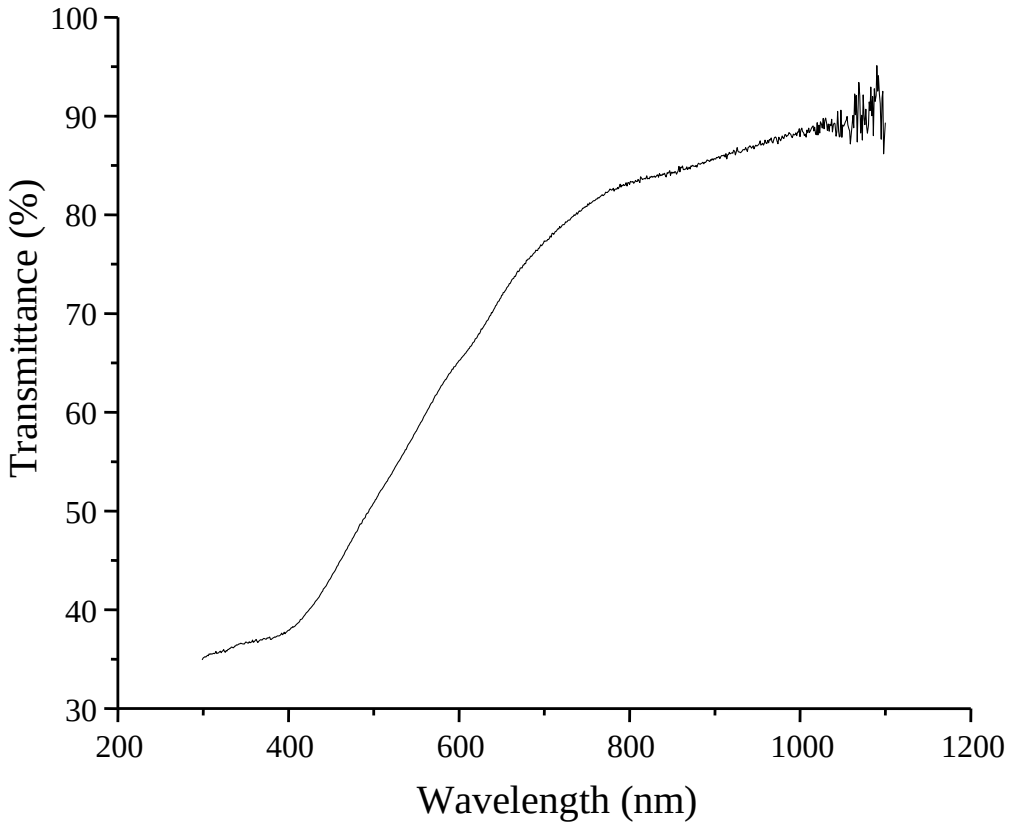

Figure 6.8. UV-Vis transmittance of hexagonal diamond on glass substrate. The data shown is corrected for substrate absorption.

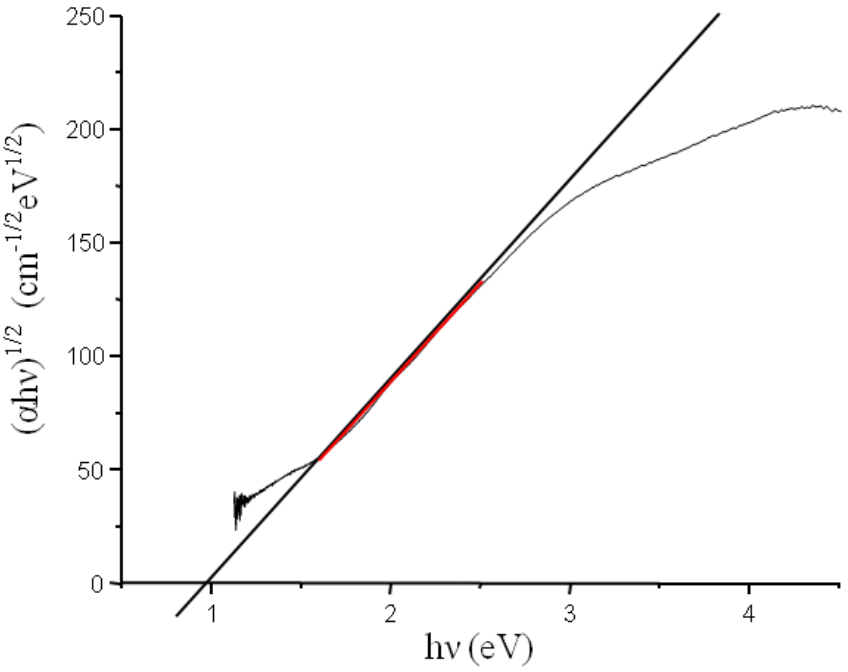

Figure 6.9. Tauc plot for hexagonal diamond film on glass substrate

6.2.6 I-V Measurements and Reduced Modulus of Hexagonal Diamond with Nano-indentation

The I-V curve and the reduced modulus were measured with Hysitron TI 900 Tribo-Indenter. The nano-indentation test is useful for the measurement of mechanical and electrical properties of thin films. In general, a diamond is utilized as an indenter tip. The diamond tip is heavily doped with boron for I-V measurements. The tip has a three-sided pyramid shape and it is known as a Berkovich indenter probe. Figure 6.10 shows the schematic diagram of sample preparation for the measurements of I-V curve and the reduced modulus. Figures 6.10 (a) and (b) are the side and the top views, respectively. The hexagonal diamond deposited sample is first loaded on a Cu plate. Then Ag paste is applied on the edge of the sample for I-V curve measurement. When the tip makes a contact with the sample, the sample properties are measured during the load and unload cycles. The load process applies force to the specimen until the maximum desired setup value, and the unload process releases the force from the maximum setup value to zero. When the tip contacts the sample, a setting voltage is applied during the load and unload cycle. The applied forces for the reduced modulus measurement are from 500 to 2500 μN with 500 μN step intervals. The applied voltages for I-V curve measurement are from 1 to 3 V with 0.5 V step intervals. The sample under each applied force step was tested with five different voltages.

Figure 6.11 is the measured I-V curve on hexagonal diamond film grown on SiO_2 coated Si substrate with 5/3/5 nm thick catalyst annealed at 450 ˚C at 10 Torr pressure in ammonia. The film is also deposited at 450 ˚C at 10 Torr pressure in Ar/CCl_4 ratio of 7/3 similar to the one shown in Fig. 5.9. I-V curve for each applied force and average value for each load are shown in Fig. 6.11. In general, resistivity is a more useful property than resistance as the former is unique to the material whereas resistance depends on the geometry of the sample. In this experiment,

resistance was measured instead of the resistivity because of the sample condition. The hexagonal diamond sample is made of many platelets of hexagonal diamonds. The size of one hexagonal diamond platelet is approximately one micron in width and length and few nanometers in thickness. Measuring resistivity of one hexagonal diamond platelet is a difficult

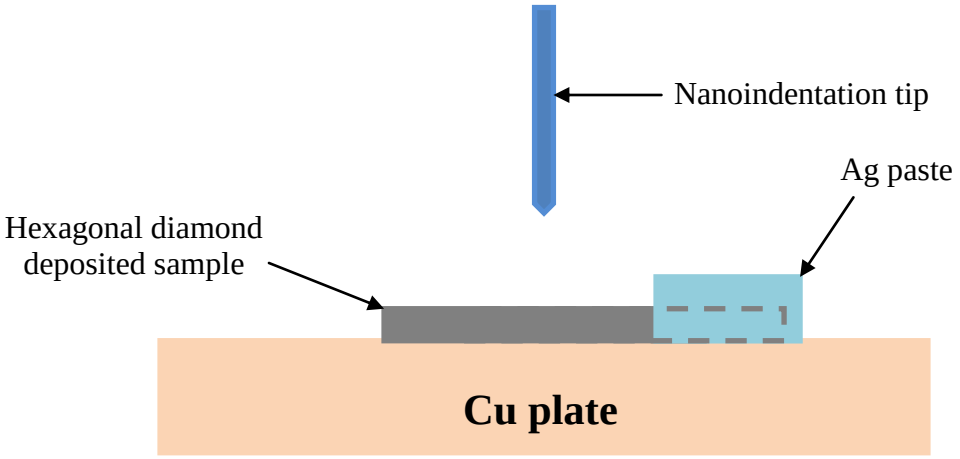

(a)

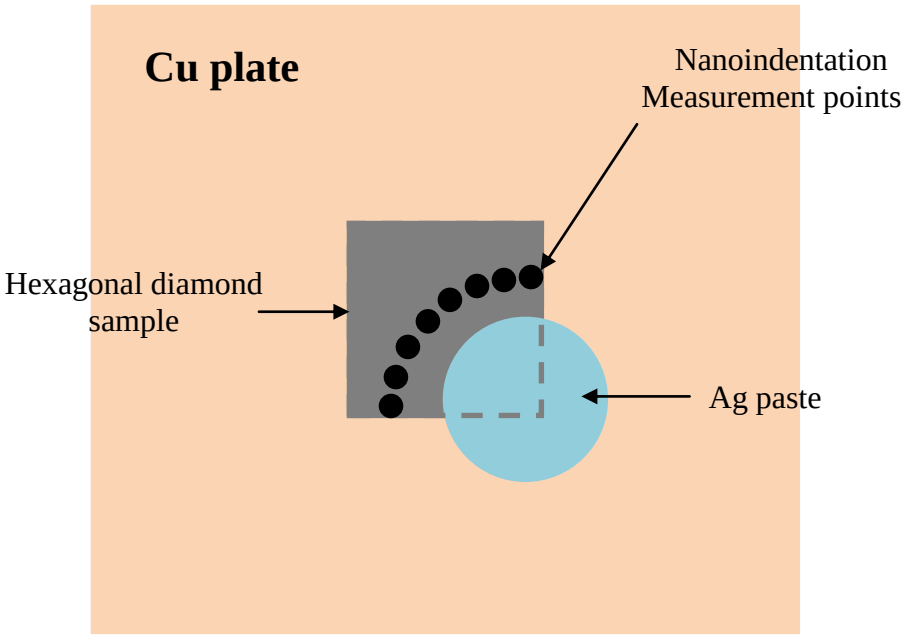

(b)

Figure 6.10. The schematic diagram of nanoindentation and ECR measurement. (a) Side view and (b) top view.

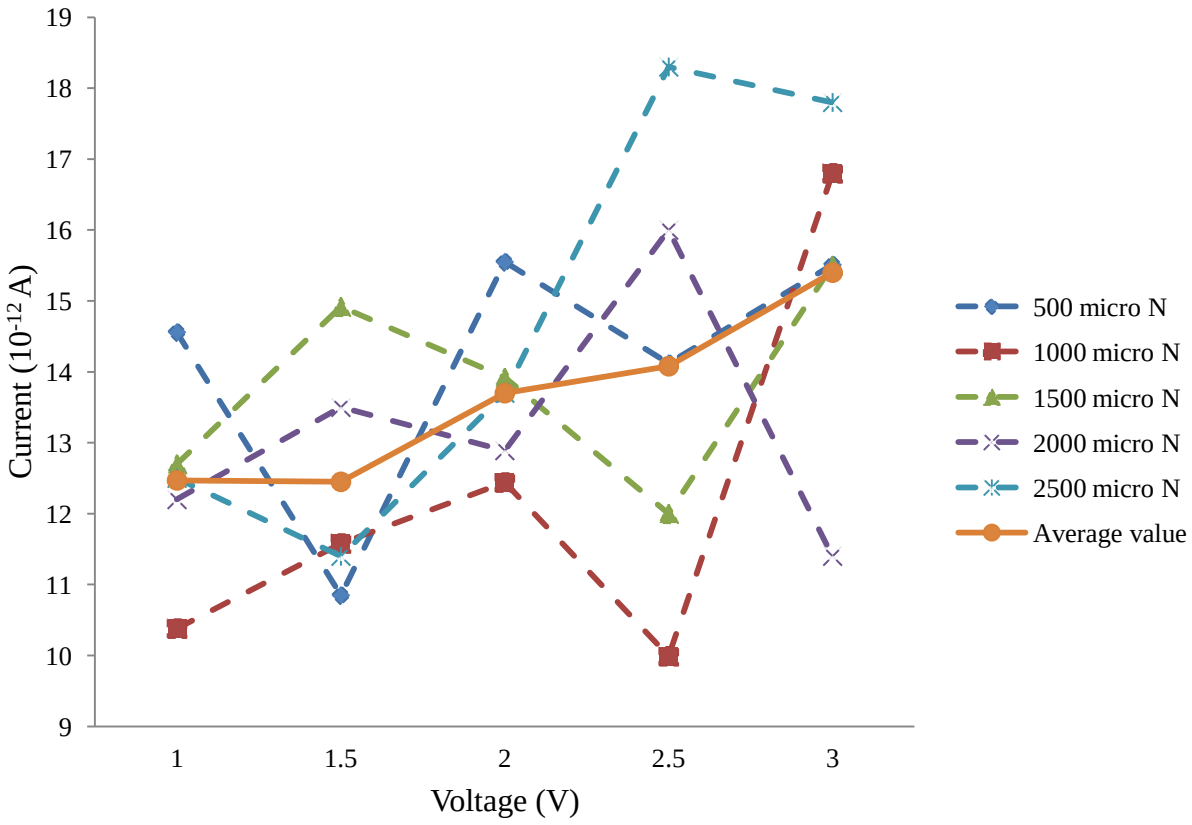

Figure 6.11. I-V characteristic of hexagonal diamond film for various force values. The average value for each case is shown.

task. Unfortunately, references related to resistivity of hexagonal diamond or the I-V curves of hexagonal diamond films have not been reported to our knowledge. Hence, it is not possible to compare the I-V curve measurements here to other reported hexagonal diamond samples. Resistivity or resistance data for a cubic diamond film have been reported in the literature, and the resistivity or resistance of hexagonal diamond film should generally be lower than that of the cubic diamond because hexagonal diamond has lower energy band gap than the cubic diamond. The reported resistivity values of the deposited cubic diamond film with CVD method varies from 10^2 to 10^{16} Ω-cm [104–106]. The resistivity depends on crystal quality, impurity concentration and defects present in the film including the presence of carbon double bond between the grains, if present. The as-grown diamond film has a resistance of between 10 and 10^7 Ω and the annealed diamond film has higher resistance [107–108]. The measured resistance of as-grown hexagonal diamond film ranges approximately from 8×10^{10} to 1.9×10^{11} Ω. This large value of hexagonal diamond resistance may result from the geometrical differences between synthesis of cubic and hexagonal diamonds. The experimented cubic diamond is monolithic thin film but the hexagonal diamond film in this study comprises of separate and inclined thin plates.

Figure 6.12 shows the reduced modulus of the hexagonal diamond sample. The relationship between the reduced modulus E_r and Young's modulus is given by $\frac{1}{E_r} = \frac{(1-\nu^2)}{E} - \frac{(1-\nu_i^2)}{E_i}$, where E and ν are respectively Young's modulus and Poisson's ratio of the sample, and E_i and ν_i are respectively Young's modulus and Poisson's ratio of the diamond tip of the indenter. Reduced modulus was measured with five different forces, and each force was experimented five times. The average reduced modulus varies from approximately 140 to 182 GPa. Young's modulus can be calculated with above equation and the values approximately range from 160 to

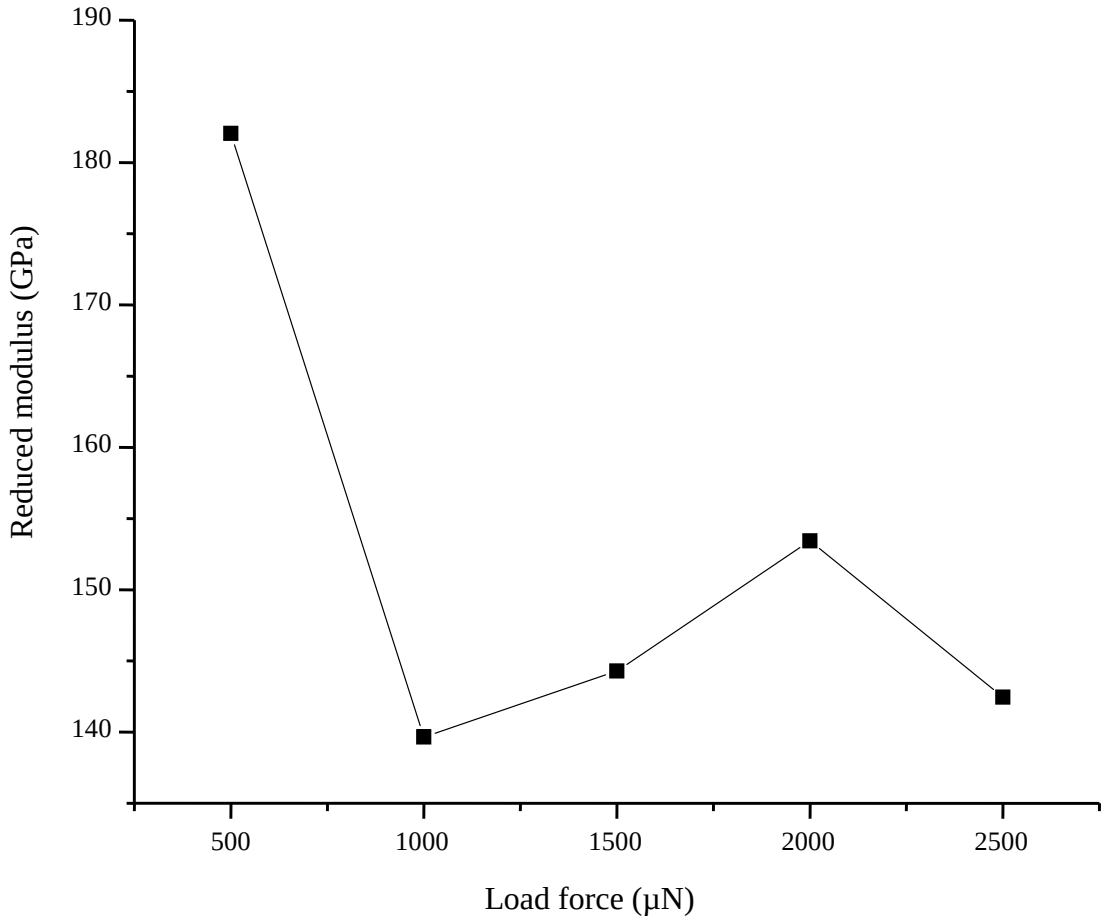

Figure 6.12. Reduced modulus of hexagonal diamond film.

213 GPa. The absolute maximum reduced modulus value obtained from our measurement is 233 GPa and the calculated Young's modulus value is 289 GPa. These measured Young's moduli are much smaller than those obtained for diamond. The Young's modulus of natural cubic diamond is known to be 1140 GPa [109]. However, the Young's modulus of a synthesized cubic diamond depends on the grain size. Bulk synthesized cubic diamond has a similar value of Young's modulus to the natural cubic diamond. The Young's modulus of nanocrystalline or ultra nanocrystalline diamond varies from 400 to 800 GPa [110–111]. The maximum value of measured Young's modulus on the sample reported here is lower than the minimum value of the reported Young's modulus on cubic diamond. However, there is a significant difference between the two. The small Young's modulus of the sample in this work can be caused by the structure, shape of the sample and calculation of contact area of nanoindentation. In general, a monolithic structure has higher Young's modulus than that of a porous structure. Furthermore, the hexagonal diamond sample consists of very thin plates that are inclined at an angle to the substrate, thus the bending effect cannot be ignored. The maximum displacement in the measurements reported here depends on the setup force and varies approximately from 36 to 150 nm. If there is no bending, the mark of the tip should be observable in AFM images. However, no such mark is observed for more than 30 indentation experiments. If the bending effect is considered, the Young's modulus of hexagonal diamond sample should have a higher value. The definition of Young's modulus is the ratio of stress to strain and the displacement causes an increase in strain, which means that if there is a bending effect, the value of Young's modulus will be smaller than the expected value. The calculated contact area of nanoindentation equipment affect the value of Young's modulus. The contact area is calculated by measuring indented depth of the tip. Thus if the sample is monolithic, calculated contact area is acceptable.

However, the sample here being platelets, the real contact area is smaller than that of the calculated one. Thus when these factors are considered, the real Young's modulus of the sample in consideration here should have a higher than the measured value.

6.3 Characterization of CNT

Characterization of the deposited CNT provides the information about the type and resistance of the CNT. In general, CNT can be classified into two types: single-wall carbon nanotube (SWCNT) and multi-wall carbon nanotube (MWCNT). The properties of both CNTs are mentioned in section 1.2. The diameter of a CNT generally defines whether a CNT is SWCNT or MWCNT. The diameter of SWCNT can be up to 5 nm but it is generally less than 2 nm [112]. However, MWCNT diameter can be as high as 100 nm [113]. The deposited CNT samples had various diameters ranging from approximately 10 nm to 50 nm in SEM images shown in Figs. 5.1 - 5.6. Raman spectroscopy on these samples shows D-band and G-band peaks. These two peaks support that the deposited CNTs are MWCNT. The I-V curve gives the resistance of the deposited CNT sample.

6.3.1 Raman Spectroscopy of CNT

General explanation of Raman spectroscopy of carbon materials is provided in section 6. 2.1. Raman spectroscopy of graphitic materials have two peaks. One is called the G-band which is approximately located at 1580 cm^{-1}. The other peak is called the D-band which is approximately located at 1350 cm^{-1}. G-band represents sp^2 hybridization thus both the SWCNT and MWCNT show this band. However, D-band indicates defects and amorphous carbon. Thus D-band for SWCNT is much smaller than that of MWCNT. This difference allows for classifying CNTs as SWCNT and MWCNT by Raman spectroscopy. In general, the ratio of D-band to G-band intensity $\left(\frac{I_D}{I_G}\right)$ for SWCNT is less than 0.5 and for MWCNT, it is approximately

between 1 and 2 [114]. Figure 6.13 shows Raman spectra of a deposited CNT sample. There are two peaks D-band and G-band at 1327 cm^{-1} and 1576 cm^{-1}, respectively. The ratio of D-band intensity to G-band intensity of the CNT sample is approximately 1.47 indicating that the growth is MWCNT.

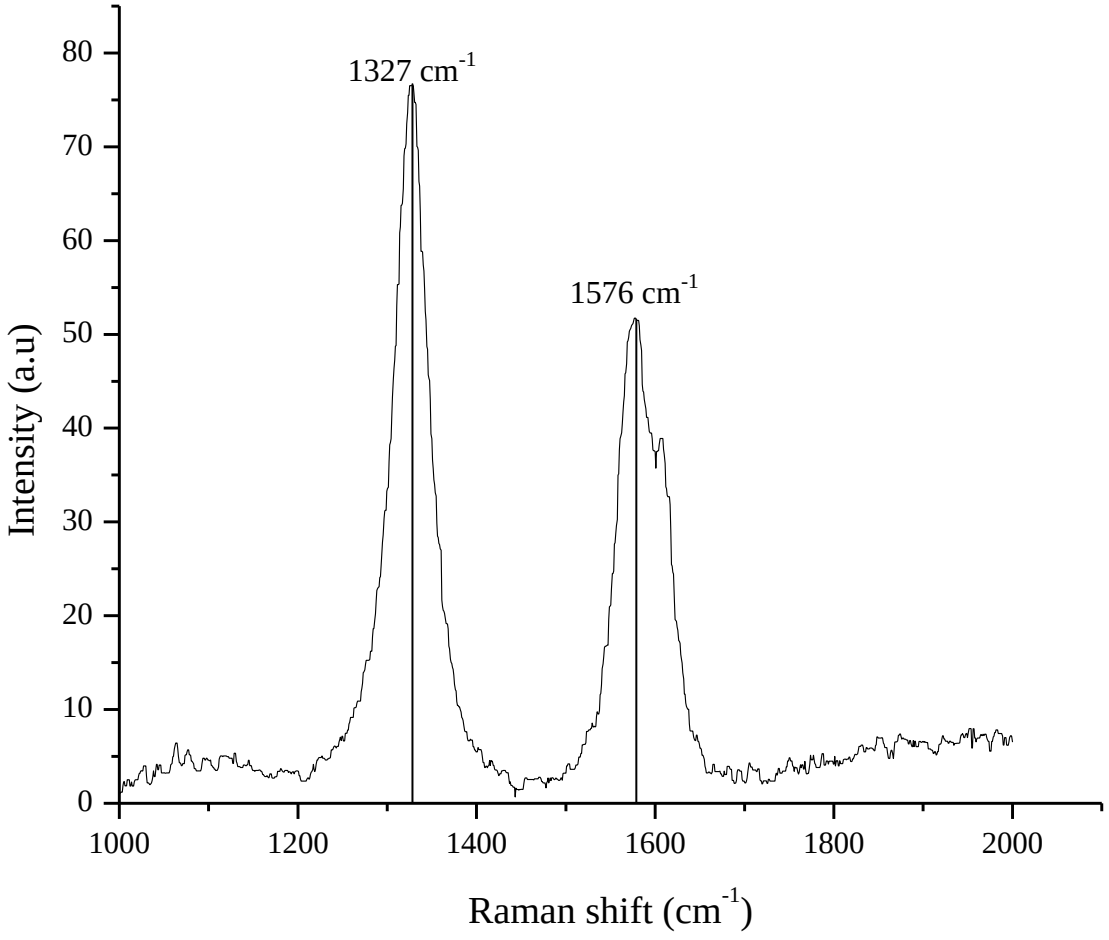

Figure 6.13. Raman spectra of deposited CNT.

6.3.2 I-V Characteristics of CNTs

The I-V curve of grown CNT film is measured using Au/Ti as contacting electrodes. The electrodes are patterned on the glass substrate. The electrodes have 5 μm gap between them and a width of 1 mm. The CNTs are separated from the substrate by scratching and are then mixed with toluene. The CNTs and the solvent mixture is sonicated for a thorough dispersion and then one drop of mixed solution is placed between the electrode gap. After evaporation of solvent, Au was deposited on the area where each electrode and CNT makes connect. Figure 6.14 shows the measured I-V characteristic. This graph shows a linear resistance of 110 Ω for the CNT sample. This gives sheet resistivity of 22 kΩ/square.

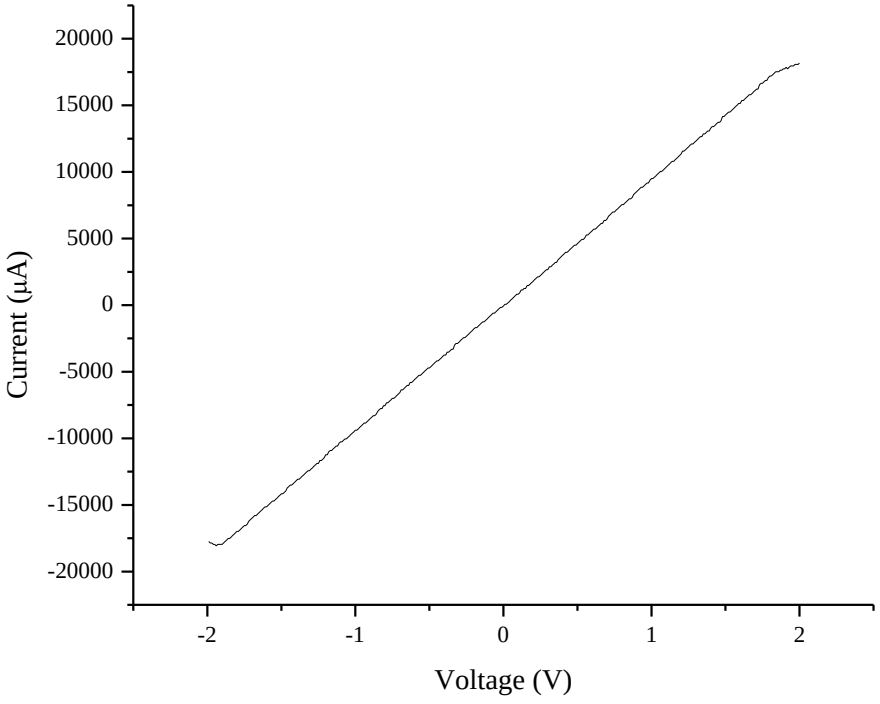

Figure 6.14. I-V curve for grown CNT on a glass substrate.

6.4 Chapter Summary

The characterizations of hexagonal diamond and CNT are reported in this chapter. The results reported here add to limited information available to date on hexagonal diamonds. Raman spectroscopy, XPS, XRD and the color of deposited sample on glass substrate confirm the hexagonal diamond deposition. The SEM images show various stages of growth. A nucleation and synthesis mechanism for hexagonal diamonds is proposed based on these observations. UV-Vis transmittance allows estimation of optical bandgap with Tauc plot. The Young's modulus and I-V characteristics are measured with a nanoindenter. Raman spectroscopy and SEM images verify MWCNT deposition. The I-V characteristic is measured using microfabricated electrodes.

CHAPTER 7. SUMMARY, CONCLUSIONS AND FUTURE WORK

7.1 Summary and Conclusions

The bonding structure of carbon atoms determines the specific carbon material such as graphite, graphene, carbon nanotubes, fullerene and diamond. Each carbon material has unique geometrical, electrical and mechanical properties. Many different methods are utilized to deposit carbon materials resulting in different material structure and properties. In this research, the primary objective is to deposit CNT and hexagonal diamond at low substrate temperatures.

In general, the deposition temperature depends on the deposition method. The current available deposition techniques for CNT are arc-discharge, laser ablation, thermal chemical vapor deposition (CVD) and plasma-enhanced CVD. These methods are useful to grow CNT but they pose drawbacks for the semiconductor industry applications. Arc-discharge, laser ablation and thermal CVD methods require high temperature for CNT deposition. PECVD can deposit CNT at low temperature but ion bombardment causes substrate damage. Photo-enhanced CVD method allows thin film deposition at low temperature without substrate damage.

Photo-enhanced CVD method has been utilized earlier for deposition of other materials but, to the best of the author's knowledge, has never been used for the growth of carbon materials. The feasibility of CNT and hexagonal diamond deposition is demonstrated in this research utilizing photo-enhanced CVD, which can be a powerful alternative method to deposit various carbon materials.

Photo-enhanced CVD method utilizes photon energy to extract carbon atoms from its precursor molecule. Thus, absorption coefficient of precursor at a given photon wavelength is an important factor. Xe lamp with output in 200 – 2400 nm wavelength range is utilized in this experiment. In general, hydrocarbon gases, which are commonly utilized for CNT or diamond

deposition as precursors, have much lower absorption coefficient in this wavelength range than CCl_4. Hence, CCl_4 is selected as a precursor molecule for this research.

The deposition chamber of photo-enhanced CVD is assembled with a six-way and a four-way cross fitting. This chamber contains two gas inlets for ammonia and CCl_4/Ar gas mixture. UV grade fused silica is used as the optical window perpendicular to the incident light beam. Two mass flow controllers (MFC) are utilized for ammonia and Ar gas flow. Carbon tetrachloride is in liquid phase under atmospheric condition at room temperature. Hence, a bubbler is used to transform from liquid to gas phase. The chamber pressure is adjusted by adjusting the exhaust throughout for a specified flow of inlet gases. A resistive heater encapsulated inside a graphite rod is utilized for heating the substrate. The substrates are held perpendicular to the incident light beam. Temperature controller maintains the set substrate temperature utilizing a type-K thermocouple through a feed-through connection. A rotary exhaust mechanical pump is utilized to control the chamber pressure.

Catalyst nanoparticles are necessary for CNT and hexagonal diamond deposition. There are several methods for nanoparticle formation process. In this research, thin film annealing method is utilized because it is a simple and convenient technique. Electron beam deposited Al and Ni thin films are utilized as catalysts. Ni film is sandwiched between two layers of Al. Ni serves as the main catalyst and Al is utilized as a co-catalyst. Thickness combinations of Al/Ni/Al experimented here are 1/1/1, 3/1/3, 5/1/5, 10/1/10, 3/2/3 and 5/3/5 nm. The catalyst layer thicknesses are measured with a crystal monitor during the deposition after calibrating the layer with an atomic force microscope (AFM). The catalyst layers are deposited on SiO_2 coated Si or glass substrates.

Annealing process produces nanoparticles from the catalyst thin film. The formation of nanoparticle is a critical factor for CNT and hexagonal diamond deposition and therefore various thicknesses of Al/Ni catalyst samples are annealed at different temperatures and pressures in ammonia gas ambient in a preliminary experiment to obtain optimized annealing conditions. Annealing process is implemented under ammonia environment because ammonia gas improve nanoparticle formation. The temperatures and pressures used for the preliminary annealing runs are 350, 375, 400, 450 ˚C and 0.22, 1, 10 Torr, respectively. The results show that optimal annealing pressure is 10 Torr. The selected annealing conditions employ 3/2/3, 5/1/5, 5/3/5 nm Al/Ni/Al sample thicknesses, 350, 400, 450 ˚C temperatures and 10 Torr pressure.

The CNT or hexagonal diamond deposition is carried out under Ar/CCl_4 ambient immediately after the annealing process in presence of incident light from Xe arc lamp. Preliminary results of the deposition process indicate that no CNT and hexagonal diamond are deposited at 350 ˚C and 3 Torr total chamber pressure.

The optimal deposition conditions for CNT and hexagonal diamond obtained in these experiments are different. CNTs can be deposited under lower chamber pressure of 5 Torr and a smaller amount of CCl_4 contained in Ar/CCl_4 gas mixture (9:1 Ar/CCl_4 partial pressure ratio) at both 400 and 450 ˚C substrate temperatures. However, hexagonal diamond deposition is observed at 450 ˚C substrate temperature and under a higher chamber pressure value of 10 Torr and with Ar/CCl_4 gas partial pressure ratios of 9:1 and 7:3. A longer deposition time is utilized for hexagonal diamond growth than that for CNT growth.

The optimized photo-enhanced CVD growth conditions obtained in this work for CNT growth under Xe arc lamp incident light is 5/1/5 nm thick Al/Ni/Al catalyst thickness, 400 ˚C substrate temperature and 10 Torr chamber pressure in ammonia environment for the annealing

cycle followed by CNT deposition at 400 ˚C substrate temperature, 5 Torr chamber pressure and Ar to CCl_4 partial pressure ratio of 9:1.

Hexagonal diamonds are deposited most densely under annealing condition of 450 ˚C for substrate temperature, Al/Ni/Al catalyst thin film with thicknesses of 5/3/5 nm and 10 Torr chamber pressure in ammonia environment followed by deposition at 10 Torr total chamber pressure with Ar/CCl_4 partial pressure ratio of 7:3 at 450 ˚C substrate temperature. However, hexagonal diamond deposited at substrate temperature of 450 ˚C under Ar/CCl_4 partial pressure ratio of 9:1 at 10 Torr chamber pressure, on Al/Ni/Al catalyst thin film thicknesses of 5/3/5 nm annealed at 450 ˚C in ammonia gives a clearer indication of geometrical shape of grown hexagonal diamond platelets.

After the deposition of CNT and hexagonal diamond, electrical and mechanical properties are measured. More focus was placed on the characterization of hexagonal diamond because currently very little information is available in literature on hexagonal diamond.

SEM is utilized for the image capturing and the geometrical study of deposited hexagonal diamond samples. Hexagonal diamond nucleation, formation and the role of graphene layer during growth are proposed in this work from different stages of hexagonal diamond synthesis images. The nucleation of hexagonal diamond seems to begin from an onion-like fullerene and the shape of the hexagonal diamond depends on the number of carbon seed atoms. In general, early stage of hexagonal diamond shows growth of radial arms attributed to defects at the corners during growth. The empty space between the radial arms is seen to be filled with graphene layers. Hexagonal diamond continues to grow over the graphene layers. The close similarity between carbon-carbon bond length of graphene and bond length of hexagonal diamond projected on (0001) plane allows for this type of growth.

XPS data indicates that the deposited material consists of C-C sigma bond observed in diamond material. The deposited carbon material is revealed as hexagonal diamond by Raman spectroscopy measurement. The Raman spectra shows a peak at 1322 cm^{-1} with a FWHM value of 75.4 cm^{-1}. This peak and FWHM indicate that the sample grown is a hexagonal diamond.

XRD data supports the conclusions drawn from Raman spectra. XRD measurement gives three peaks at 39.4, 47.7 and 59.5˚, which correspond to 0.219, 0.189 and 0.149 nm interplanar spacing, respectively, which can be attributed to 0.219, 0.192, and 0.150 nm d-spacing of hexagonal diamond (100), (101) and (102) planes, respectively.

Hexagonal diamond deposited on a glass substrate indicates a brownish-yellow color which is the same as other known samples of hexagonal diamonds and is utilized for measurement of transmittance. The net transmittance of hexagonal diamond film is measured with UV-Vis spectroscopy and optical band gap is calculated by using Tauc plot. The observed optical band gap of our sample is approximately 1.0 eV.

A nanoindenter is utilized to measure reduced modulus and resistance of hexagonal diamond film. Young's modulus can be obtained from the reduced modulus and the calculated Young's modulus value varies approximately from 160 to 213 GPa. Significant difference between Young's modulus of hexagonal diamond and cubic diamond seems to be caused by bending effect and measurement error of contact area of the nanoindenter because of the nature of the grown hexagonal diamond film in this work. The average resistance of our measured as-grown hexagonal diamond film varied from approximately 8×10^{10} to 1.95×10^{11} Ω.

As mentioned earlier, there is limited hexagonal diamond information available in literature thus it is difficult to compare our observed data with other reported values. The

measured data such as optical band gap, resistance and Young's modulus are hence compared to simulation data or the corresponding measured values for cubic diamond.

The type and resistance of the deposited CNT layers are characterized with Raman spectroscopy and fabricated electrode geometry, respectively. Raman spectra show two peaks, namely D-band and G-band at 1327 cm^{-1} and 1576 cm^{-1}, respectively. The ratio of D-band intensity to G-band intensity of our CNT sample is approximately 1.47 indicating that the growth is MWCNT. The resistance of CNT on a glass substrate is measured with Au/Ti electrodes assembly. The measured resistance is 110 Ω and the sheet resistivity is 22 kΩ/square.

7.2 Future Work

The successful deposition of CNT and hexagonal diamonds by utilizing photo-enhanced CVD is demonstrated through this research. Photo-enhanced CVD is a novel method in carbon material synthesis and this research shows the possibility of CNT deposition with photo-enhanced CVD at low temperature for integration with semiconductor devices. However, more research needs to be done for selectively controlling the CNT deposition on the substrate.

Hexagonal diamond is a rare material naturally as well as synthetically thus there are limited references on measured hexagonal diamond properties. Most hexagonal diamond properties come from simulation results. The Young's modulus and I-V curve of our hexagonal diamond samples are measured with a nanoindenter. The nanoindenter gives accurate values in Young's modulus and I-V curve for monolithic sample but the measured sample with densely packed hexagonal diamond platelets leads to a lower value for Young's modulus than the actual value because of the error in calculated contact area and estimation of strain. Thus, it is necessary to measure a single hexagonal diamond platelet for more accurate properties. However this experiment could not be performed, because separating a single hexagonal diamond platelet for

measurements is difficult. The hexagonal diamond is a superhard material and has a large surface-to-volume ratio. Thus the manipulation of hexagonal diamond platelet standing angle has potentials for many applications.

Photo-enhanced CVD is a low temperature deposition technique for hexagonal diamond and CNT growth and needs to be studied in detail with a wavelength tunable light source in conjunction with in situ analytical tools like laser induced fluorescence and/or laser raman spectroscopy to observe photo-fragment chemistry of the growth process.

BIBLIOGRAPHY

[1] S. Iijima, "Helical microtubules of graphitic carbon," *Nature*, vol. 354, pp. 56–58, 1991.

[2] T. Guo, P. Nikolaev, A. Thess, D. T. Colbert, and R. E. Smalley, "Catalytic growth of single walled nanotubes by laser vaporization," *Chemical Physics Letters*, vol. 243, pp. 49–54, 1995.

[3] A. V. Melechko, V. I. Merkulov, T. E. McKnight, M. A. Guillorn, K. L. Klein, D. H. Lowndes, and M. L. Simpson, "Vertically aligned carbon nanofibers and related structures: Controlled synthesis and directed assembly," *Journal of Applied Physics*, vol. 97, pp. 041301–39, 2005.

[4] S. Wei, W. P. Kang, J. L. Davidson, and J. H. Huang, "Aligned carbon nanotubes fabricated by thermal CVD at atmospheric pressure using Co as catalyst with NH_3 as reactive gas," *Diamond and Related Materials*, vol. 15, pp. 1828–1833, 2006.

[5] F. P. Bundy and J. S. Kasper, "Hexagonal Diamond—A New Form of Carbon," *The Journal of Chemical Physics*, vol. 46, pp. 3437–3446, 1967.

[6] L. F. Trueb, "An Electron-Microscope Study of Shock-Synthesized Diamond," *Journal of Applied Physics*, vol. 39, pp. 4707–4716, 1968.

[7] H. He, T. Sekine, and T. Kobayashi, "Direct transformation of cubic diamond to hexagonal diamond," *Applied Physics Letters*, vol. 81, pp. 610–612, 2002.

[8] C. X. Wang, Y. H. Yang, Q. X. Liu, G. W. Yang, Y. L. Mao, and X. H. Yan, "Phase stability of diamond nanocrystals upon pulsed-laser-induced liquid-solid interfacial reaction: Experiments and ab initio calculations," *Applied Physics Letters*, vol. 84, pp. 1471–1473, 2004.

[9] V. Amornkitbamrung, T. Burinprakhone, and W. Jarernboon, "Hexagonal diamond formation on steel substrates by negative bias microwave plasma enhanced chemical vapor deposition," *Surface and Coatings Technology*, vol. 203, pp. 1645–1648, 2009.

[10] A. Misra, P. K. Tyagi, B. S. Yadav, P. Rai, D. S. Misra, V. Pancholi, and I. D. Samajdar, "Hexagonal diamond synthesis on h-GaN strained films," *Applied Physics Letters*, vol. 89, pp. 071911–3, 2006.

[11] R. Z. Khaliullin, H. Eshet, T. D. Kühne, J. Behler, and M. Parrinello, "Nucleation mechanism for the direct graphite-to-diamond phase transition," *Nature Materials*, vol. 10, pp.693–697, 2011.

[12] D. P. Norton and P. K. Ajmera, "Spatially selective photochemical vapor deposition of GaAs on synthetic fused silica," *Applied Physics Letters*, vol. 53, pp. 595–597, 1988.

[13] R. B. Heimann, J. Kleiman, and N. M. Salansky, "A unified structural approach to linear

carbon polytypes," *Nature*, vol. 306, pp. 164–167, 1983.

[14] M. S. Dresselhaus, G. Dresselhaus, and P. C. Eklund, *Science of Fullerenes and Carbon Nanotubes: Their Properties and Applications*. Elsevier Science, 1996.

[15] S. Iijima and T. Ichihashi, "Single-shell carbon nanotubes of 1-nm diameter," *Nature*, vol. 363, pp. 603–605, 1993.

[16] R. Saito, G. Dresselhaus, and M. S. Dresselhaus, *Physical Properties of Carbon Nanotubes*. Imperial College Press, 1998.

[17] R. Saito, G. Dresselhaus, and M. S. Dresselhaus, "Electronic structure of double-layer graphene tubules," *Journal of Applied Physics*, vol. 73, pp. 494–500, 1993.

[18] P. Lambin, L. Philippe, J. C. Charlier, and J. P. Michenaud, "Electronic band structure of multilayered carbon tubules," *Computational Materials Science*, vol. 2, pp. 350–356, 1994.

[19] R. Saito, M. Fujita, G. Dresselhaus, and M. S. Dresselhaus, "Electronic structure and growth mechanism of carbon tubules," *Materials Science and Engineering: B*, vol. 19, pp. 185–191, 1993.

[20] M. S. Dresselhaus, G. Dresselhaus, and R. Saito, "Group theoretical concepts for C_{60} and other fullerenes," *Materials Science and Engineering: B*, vol. 19, pp. 122–128, 1993.

[21] J. C. Charlier and J. P. Michenaud, "Energetics of multilayered carbon tubules," *Physical Review Letters*, vol. 70, pp. 1858–1861, 1993.

[22] C. Frondel and U. B. Marvin, "Lonsdaleite, a Hexagonal Polymorph of Diamond," *Nature*, vol. 214, pp. 587–589, 1967.

[23] B. R. Wu and J. Xu, "Total energy calculations of the lattice properties of cubic and hexagonal diamond," *Physica. Review B*, vol. 57, pp. 13355–13358, 1998.

[24] Z. Pan, H. Sun, Y. Zhang, and C. Chen, "Harder than Diamond: Superior Indentation Strength of Wurtzite BN and Lonsdaleite," *Physical Review Letters*, vol. 102, pp. 055503, 2009.

[25] M. R. Salehpour and S. Satpathy, "Comparison of electron bands of hexagonal and cubic diamond," *Physical Review B*, vol. 41, pp. 3048–3052, 1990.

[26] G. B. Adams, O. F. Sankey, J. B. Page, M. O'keeffe, and D. A. Drabold, "Energetics of large fullerenes: balls, tubes, and capsules," *Science*, vol. 256, pp. 1792–1795, 1992.

[27] W. K. Maser, E. Muñoz, A. M. Benito, M. T. Martínez, G. F. de la Fuente, Y. Maniette, E. Anglaret, and J.-L. Sauvajol, "Production of high-density single-walled nanotube material

by a simple laser-ablation method," *Chemical Physics Letters*, vol. 292, pp. 587–593, 1998.

[28] Y. Joon Yoon, J. Cheol Bae, H. Koo Baik, S. Cho, S.-J. Lee, K. Moon Song, and N. Seung Myung, "Growth control of single and multi-walled carbon nanotubes by thin film catalyst," *Chemical Physics Letters*, vol. 366, pp. 109–114, 2002.

[29] M. Cantoro, S. Hofmann, S. Pisana, V. Scardaci, A. Parvez, C. Ducati, A. C. Ferrari, A. M. Blackburn, K. Y. Wang, and J. Robertson, "Catalytic Chemical Vapor Deposition of Single-Wall Carbon Nanotubes at Low Temperatures," *Nano Letters*, vol. 6, pp. 1107–1112, 2006.

[30] L. Delzeit, B. Chen, A. Cassell, R. Stevens, C. Nguyen, and M. Meyyappan, "Multilayered metal catalysts for controlling the density of single-walled carbon nanotube growth," *Chemical Physics Letters*, vol. 348, pp. 368–374, 2001.

[31] A. C. Dupuis, "The catalyst in the CCVD of carbon nanotubes—a review," *Progress in Materials Science*, vol. 50, pp. 929–961, 2005.

[32] M. A. Ermakova, D. Y. Ermakov, A. L. Chuvilin, and G. G. Kuvshinov, "Decomposition of Methane over Iron Catalysts at the Range of Moderate Temperatures: The Influence of Structure of the Catalytic Systems and the Reaction Conditions on the Yield of Carbon and Morphology of Carbon Filaments," *Journal of Catalysis*, vol. 201, pp. 183–197, 2001.

[33] Z. W. Pan, S. S. Xie, B. H. Chang, L. F. Sun, W. Y. Zhou, and G. Wang, "Direct growth of aligned open carbon nanotubes by chemical vapor deposition," *Chemical Physics Letters*, vol. 299, pp. 97–102, 1999.

[34] P. S. Dario Venegoni, "Parametric study for the growth of carbon nanotubes by catalytic chemical vapor deposition in a fluidized bed reactor," *Carbon*, vol. 40, pp. 1799–1807, 2002.

[35] H. Ago, T. Komatsu, S. Ohshima, Y. Kuriki, and M. Yumura, "Dispersion of metal nanoparticles for aligned carbon nanotube arrays," *Applied Physics Letters*, vol. 77, pp. 79–81, 2000.

[36] Y. H. Wang, J. Lin, C. H. A. Huan, and G. S. Chen, "Synthesis of large area aligned carbon nanotube arrays from C_2H_2–H_2 mixture by rf plasma-enhanced chemical vapor deposition," *Applied Physics Letters*, vol. 79, pp. 680–682, Jul. 2001.

[37] H. G. Jiang, H. Y. Tong, X. M. Xue, B. Z. Ding, Q. H. Song, Z. Q. Hu, and J. T. Wang, "Observation of rapid explosive reaction in Ni-Al bilayer films," *Journal of Materials Science Letters*, vol. 12, pp. 1687–1689, 1993.

[38] E. Ma, C. V. Thompson, L. A. Clevenger, and K. N. Tu, "Self-propagating explosive reactions in Al/Ni multilayer thin films," *Applied Physics Letters*, vol. 57, pp. 1262, 1990.

[39] Y. Zhang, Y. Li, W. Kim, D. Wang, and H. Dai, “Imaging as-grown single-walled carbon nanotubes originated from isolated catalytic nanoparticles,” *Applied Physics A: Materials Science & Processing*, vol. 74, pp. 325–328, 2002.

[40] I. Willems, Z. Kónya, J. F. Colomer, G. Van Tendeloo, N. Nagaraju, A. Fonseca, and J. B. Nagy, “Control of the outer diameter of thin carbon nanotubes synthesized by catalytic decomposition of hydrocarbons,” *Chemical Physics Letters*, vol. 317, pp. 71–76, 2000.

[41] P. A. Tesner, E. Y. Robinovich, I. S. Rafalkes, and E. F. Arefieva, “Formation of carbon fibers from acetylene,” *Carbon*, vol. 8, pp. 435–442, 1970.

[42] R. T. K. Baker, M. A. Barber, P. S. Harris, F. S. Feates, and R. J. Waite, “Nucleation and growth of carbon deposits from the nickel catalyzed decomposition of acetylene,” *Journal of Catalysis*, vol. 26, pp. 51–62, 1972.

[43] R. T. K. Baker, “Catalytic growth of carbon filaments,” *Carbon*, vol. 27, pp. 315–323, 1989.

[44] A. V. Melechko, V. I. Merkulov, D. H. Lowndes, M. A. Guillorn, and M. L. Simpson, “Transition between `base' and `tip' carbon nanofiber growth modes,” *Chemical Physics Letters*, vol. 356, pp. 527–533, 2002.

[45] S. Helveg, C.Lopez-Cartes, J. Sehested, P.L. Hansen, B.S. Clausen, J.R. Rostrup-Nielsen, F. Abild-Pedersen and J.K. Norskov, *Atomic-scale imaging of carbon nanofibre growth.* Nature, vol. 427, pp. 426-429, 2004

[46] D. Takagi, Y. Homma, H. Hibino, S. Suzuki, and Y. Kobayashi, “Single-Walled Carbon Nanotube Growth from Highly Activated Metal Nanoparticles,” *Nano Letters*, vol. 6, pp. 2642–2645, 2006.

[47] J. Rostrup-Nielsen and D. L. Trimm, “Mechanisms of carbon formation on nickel-containing catalysts,” *Journal of Catalysis*, vol. 48, pp. 155–165, 1977.

[48] P. K. de Bokx, A. J. H. M. Kock, E. Boellaard, W. Klop, and J. W. Geus, “The formation of filamentous carbon on iron and nickel catalysts: I. Thermodynamics,” *Journal of Catalysis*, vol. 96, pp. 454–467, 1985.

[49] P. M. Ajayan, J. M. Lambert, P. Bernier, L. Barbedette, C. Colliex, and J. M. Planeix, “Growth morphologies during cobalt-catalyzed single-shell carbon nanotube synthesis,” *Chemical Physics Letters*, vol. 215, pp. 509–517, 1993.

[50] S. Seraphin and D. Zhou, “Single-walled carbon nanotubes produced at high yield by mixed catalysts,” *Applied Physics Letters*, vol. 64, pp. 2087, 1994.

[51] H. Kanzow and A. Ding, “Formation mechanism of single-wall carbon nanotubes on liquid metal particles,” *Physical Review B*, vol. 60, pp. 11180–11186, 1999.

[52] J. Robertson, "Growth of nanotubes for electronics," *Materials Today*, vol. 10, pp. 36–43, 2007.

[53] V. I. Merkulov, M. A. Guillorn, D. H. Lowndes, M. L. Simpson, and E. Voelkl, "Shaping carbon nanostructures by controlling the synthesis process," *Applied Physics Letters*, vol. 79, pp. 1178 –1180, 2001.

[54] A. T. S. W. G. W. Ho, "Synthesis of well-aligned multiwalled carbon nanotubes on Ni catalyst using radio frequency plasma-enhanced chemical vapor deposition," *Thin Solid Films*, vol. 388, pp. 73–77, 2001.

[55] S. H. Tsai, C. W. Chao, C. L. Lee, and H. C. Shih, "Bias-enhanced nucleation and growth of the aligned carbon nanotubes with open ends under microwave plasma synthesis," *Applied Physics Letters*, vol. 74, pp. 3462 –3464, 1999.

[56] N. Satake, G. H. Jeong, T. Hirata, R. Hatakeyama, H. Ishida, K. Tohji, and K. Motomiya, "Production of carbon nanotubes by controlling radio-frequency glow discharge with reactive gases," *Physica B: Condensed Matter*, vol. 323, pp. 290–292, 2002.

[57] M. Meyyappan, L. Delzeit, A. Cassell, and D. Hash, "Carbon nanotube growth by PECVD: a review," *Plasma Sources Science and Technology*, vol. 12, pp. 205–216, 2003.

[58] T. Kato, G. H. Jeong, T. Hirata, R. Hatakeyama, K. Tohji, and K. Motomiya, "Single-walled carbon nanotubes produced by plasma-enhanced chemical vapor deposition," *Chemical Physics Letters*, vol. 381, pp. 422–426, 2003.

[59] A. Gohier, T. M. Minea, A. M. Djouadi, A. Granier, and M. Dubosc, "Limits of the PECVD process for single wall carbon nanotubes growth," *Chemical Physics Letters*, vol. 421, pp. 242–245, 2006.

[60] H. Niki and G. J. Mains, "The 3P1 Mercury-Photosensitized Decomposition of Monosilane," *J. Phys. Chem.*, vol. 68, pp. 304–309, 1964.

[61] S. J. C. Irvine, J. B. Mullin, and J. Tunnicliffe, "Photosensitisation: A stimulant for the low temperature growth of epitaxial HgTe," *Journal of Crystal Growth*, vol. 68, pp. 188–193, 1984.

[62] V. K. Rathi, M. Gupta, R. Thangaraj, K. S. Chari, and O. P. Agnihotri, "Photo-processing of silicon nitride," *Thin Solid Films*, vol. 266, pp. 219–223, 1995.

[63] S. Mukhopadhyay, T. Jana, and S. Ray, "Development of low temperature silicon oxide thin films by photo-CVD for surface passivation," *Journal of Vacuum Science & Technology A: Vacuum, Surfaces, and Films*, vol. 23, p. 417, 2005.

[64] S. N. Bondi, W. J. Lackey, R. W. Johnson, X. Wang, and Z. L. Wang, "Laser assisted chemical vapor deposition synthesis of carbon nanotubes and their characterization," *Carbon*, vol. 44, pp. 1393–1403, 2006.

[65] D. Ehrlich, R. Osgood, and T. Deutsch, "Laser microphotochemistry for use in solid-state electronics," *IEEE Journal of Quantum Electronics*, vol. 16, pp. 1233–1243, 1980.

[66] D. Bäuerle, P. Irsigler, G. Leyendecker, H. Noll, and D. Wagner, "Ar^+ laser induced chemical vapor deposition of Si from SiH_4," *Applied Physics Letters*, vol. 40, pp. 819–821, 1982.

[67] Y. Kawate, A. Nakaue, and H. Tachibana, "Excimer Laser Induced Chemical Vapor Deposition of Amorphous Carbon Films," *Kobelco Technology Review*, vol. 5, pp. 45–48, 1998.

[68] S. L. B. Fowler, "Epitaxial silicon growth conditions and kinetics in low-temperature ArF excimer laser photochemical-vapor deposition from disilane," *Journal of Applied Physics*, pp. 1137–1148, 1992.

[69] Y. F. Chen, C. S. Tsai, and Y. Chang, "Photoluminescence study of hydrogen passivation in GaAs and AlGaAs by the photochemical vapor deposition system," *Applied Physics Letters*, vol. 57, pp. 70–72, 1990.

[70] B. S. Sahu, A. Kapoor, P. Srivastava, O. P. Agnihotri, and S. M. Shivaprasad, "Study of thermally grown and photo-CVD deposited silicon oxide–silicon nitride stack layers," *Semiconductor Science and Technology*, vol. 18, pp. 670–675, 2003.

[71] Y. Z. Chiou, S. J. Chang, Y. K. Su, C. K. Wang, T. K. Lin, and B. R. Huang, "Photo-CVD SiO_2 layers on AlGaN and AlGaN-GaN MOSHFET," *IEEE Transactions on Electron Devices*, vol. 50, pp. 1748–1752, 2003.

[72] F. Rohmund, R. E. Morjan, G. Ledoux, F. Huisken, and R. Alexandrescu, "Carbon nanotube films grown by laser-assisted chemical vapor deposition," *Journal of Vacuum Science & Technology B: Microelectronics and Nanometer Structures*, vol. 20, pp. 802, 2002.

[73] R. Alexandrescu, A. Crunteanu, R. E. Morjan, I. Morjan, F. Rohmund, L. K. L. Falk, G. Ledoux, and F. Huisken, "Synthesis of carbon nanotubes by CO_2-laser-assisted chemical vapour deposition," *Infrared Physics & Technology*, vol. 44, pp. 43–50, Feb. 2003.

[74] A. C. A. Souza and S. K. Srivastava, "Photoabsorption cross sections of Ar, N_2 and $Si(CH_3)_4$ derived from electron energy loss spectroscopy," *Journal of Brazilian Chemical Society*, vol. 5, pp. 59–65, 1994.

[75] M. Nishitani-Gamo, I. Sakaguchi, K. P. Loh, H. Kanda, and T. Ando, "Confocal Raman spectroscopic observation of hexagonal diamond formation from dissolved carbon in nickel under chemical vapor deposition conditions," *Applied Physics Letters*, vol. 73, pp. 765–767, 1998.

[76] Y. Hayashi, N. Shiraokawa, and S. Nishino, "Effect of bias-enhancement in diamond nucleation and growth on nickel," *Thin Solid Films*, vol. 374, pp. 268–273, 2000.

[77] O. A. Shenderova, V. V. Zhirnov, and D. W. Brenner, "Carbon Nanostructures," *Critical Reviews in Solid State & Materials Science*, vol. 27, pp. 227–356, Jul. 2002.

[78] P. Nikolaev, M. J. Bronikowski, R. K. Bradley, F. Rohmund, D. T. Colbert, K. A. Smith, and R. E. Smalley, "Gas-phase catalytic growth of single-walled carbon nanotubes from carbon monoxide," *Chemical Physics Letters*, vol. 313, pp. 91–97, 1999.

[79] J. K. Vohs, J. J. Brege, J. E. Raymond, A. E. Brown, G. L. Williams, and B. D. Fahlman, "Low-Temperature Growth of Carbon Nanotubes from the Catalytic Decomposition of Carbon Tetrachloride," *Journal of the American Chemical Society*, vol. 126, pp. 9936–9937, 2004.

[80] M. Jung, K. Y. Eun, Y. J. Baik, K. R. Lee, J. K. Shin, and S. T. Kim, "Effect of NH_3 environmental gas on the growth of aligned carbon nanotube in catalystically pyrolizing C_2H_2," *Thin Solid Films*, vol. 398–399, pp. 150–155, 2001.

[81] J. Kong, A. M. Cassell, and H. Dai, "Chemical vapor deposition of methane for single walled carbon nanotubes," *Chemical Physics Letters*, vol. 292, pp. 567–574, 1998.

[82] B. Louis, G. Gulino, R. Vieira, J. Amadou, T. Dintzer, S. Galvagno, G. Centi, M. J. Ledoux, and C. Pham-Huu, "High yield synthesis of multi-walled carbon nanotubes by catalytic decomposition of ethane over iron supported on alumina catalyst," *Catalysis Today*, vol. 102–103, pp. 23–28, 2005.

[83] S. Takenaka, T. Iguchi, E. Tanabe, H. Matsune, and M. Kishida, "Formation of carbon nanotubes through ethylene decomposition over supported Pt catalysts and silica-coated Pt catalysts," *Carbon*, vol. 47, pp. 1251–1257, 2009.

[84] R. I. Schoen, "Absorption, Ionization, and Ion-Fragmentation Cross Sections of Hydrocarbon Vapors under Vacuum-Ultraviolet Radiation," *The Journal of Chemical Physics*, vol. 37, pp. 2032, 1962.

[85] F. Z. Chen and C. Y. R. Wu, "Temperature-dependent photoabsorption cross sections in the VUV-UV region. I. Methane and ethane," *Journal of Quantitative Spectroscopy and Radiative Transfer*, vol. 85, pp. 195–209, 2004.

[86] J. A. Myer and J. A. R. Samson, "Vacuum-Ultraviolet Absorption Cross Sections of CO, HCl, and ICN between 1050 and 2100 Å," *The Journal of Chemical Physics*, vol. 52, pp. 266–271, 1970.

[87] V. Prahlad and V. Kumar, "Temperature dependence of photoabsorption cross sections of carbon tetrachloride at 186–240 nm," *Journal of Quantitative Spectroscopy and Radiative Transfer*, vol. 54, pp. 945–955, 1995.

[88] Y. T. Jang, J. H. Ahn, Y. H. Lee, and B. K. Ju, "Effect of NH_3 and thickness of catalyst on growth of carbon nanotubes using thermal chemical vapor deposition," *Chemical Physics Letters*, vol. 372, pp. 745–749, 2003.

[89] K. Kang, Y. Jin, J. Kim, and P. K. Ajmera, "Study on low temperature growth and formation mechanism of hexagonal diamond," *Diamond and Related Materials*, vol. 27–28, pp. 76–81, 2012.

[90] W. R. L. Lambrecht, C. H. Lee, B. Segall, J. C. Angus, Z. Li, and M. Sunkara, "Diamond nucleation by hydrogenation of the edges of graphitic precursors," *Nature*, vol. 364, pp. 607–610, 1993.

[91] A. T. Balaban, D. J. Klein, and C. A. Folden, "Diamond-graphite hybrids," *Chemical Physics Letters*, vol. 217, pp. 266–270, 1994.

[92] J. J. Dubray, C. G. Pantano, and W. A. Yarbrough, "Graphite as a substrate for diamond growth," *Journal of Applied Physics*, vol. 72, pp. 3136 –3142, 1992.

[93] B. S. Xu and S. I. Tanaka, "Formation of giant onion-like fullerenes under Al nanoparticles by electron irradiation," *Acta Materialia*, vol. 46, pp. 5249–5257, 1998.

[94] D. S. Knight and W. B. White, "Characterization of diamond films by Raman spectroscopy," *Journal of Materials Research*, vol. 4, pp. 385–393, 1989.

[95] D. C. Smith and G. Godard, "UV and VIS Raman spectra of natural lonsdaleites: towards a recognised standard," *Spectrochimica Acta Part A: Molecular and Biomolecular Spectroscopy*, vol. 73, pp. 428–435, 2009.

[96] C. N. He, N. Q. Zhao, C. S. Shi, X. W. Du, and J. J. Li, "Effect of annealing on the structure of carbon onions and the annealed carbon coated Ni nanoparticles fabricated by chemical vapor deposition," *Journal of Alloys and Compounds*, vol. 472, pp. 230–233, 2009.

[97] J. Y. L. Jae Hyoung Choi, "Phase evolution in aluminum nitride thin films on Si (100) prepared by radio frequency magnetron sputtering," *Thin Solid Films*, vol. 384, pp. 166–172, 2001.

[98] M. M. Grady, M. R. Lee, J. W. Arden, and C. T. Pillinger, "Multiple diamond components in Acfer 182," *Earth and Planetary Science Letters*, vol. 136, pp. 677–692, 1995.

[99] J. Schein, K. M. Campbell, N. Qi, and A. Krishnan, "Ultra-fast UV-triggered high voltage diamond switch," in *Pulsed Power Plasma Science, 2001. IEEE Conference Record - Abstracts*, 2001, p. 243.

[100] V. Ralchenko, S. Pimenov, V. Konov, A. Khomich, A. Saveliev, A. Popovich, I. Vlasov, E. Zavedeev, A. Bozhko, E. Loubnin, and R. Khmelnitskii, "Nitrogenated nanocrystalline diamond films: Thermal and optical properties," *Diamond and Related Materials*, vol. 16, pp. 2067–2073, 2007.

[101] Z. Hu, P. Prunici, P. Hess, and K. Chen, "Optical properties of nanocrystalline diamond

films from mid-infrared to ultraviolet using reflectometry and ellipsometry," *Journal of Materials Science: Materials in Electronics*, vol. 18, pp. 37–41, 2007.

[102] T. Sharda, M. M. Rahaman, Y. Nukaya, T. Soga, T. Jimbo, and M. Umeno, "Structural and optical properties of diamond and nano-diamond films grown by microwave plasma chemical vapor deposition," *Diamond and Related Materials*, vol. 10, pp. 561–567, 2001.

[103] A. Khomich, M. Kanzyuba, I. Vlasov, V. Ral'chenko, and N. Gorbachuk, "Optical spectroscopy of the surface of nanoporous diamond films," *Journal of Applied Spectroscopy*, vol. 78, pp. 563–571, 2011.

[104] A. K. Kulkarni, K. Tey, and H. Rodrigo, "Electrical characterization of CVD diamond thin films grown on silicon substrates," *Thin Solid Films*, vol. 270, pp. 189–193, 1995.

[105] M. I. Landstrass and K. V. Ravi, "Resistivity of chemical vapor deposited diamond films," *Applied Physics Letters*, vol. 55, pp. 975–977, 1989.

[106] P. W. May, "CVD diamond: a new technology for the future?," *Endeavour*, vol. 19, pp. 101–106, 1995.

[107] Y. Show, M. Iwase, and T. Izumi, "Structural characterization of CVD diamond films using the ESR method," *Thin Solid Films*, vol. 274, pp. 50–54, 1996.

[108] K. Subramanian, W. P. Kang, J. L. Davidson, and W. H. Hofmeister, "Growth aspects of nanocrystalline diamond films and their effects on electron field emissions," *Journal of Vacuum Science Technology B: Microelectronics and Nanometer Structures*, vol. 23, pp. 786 –792, 2005.

[109] N. Dubrovinskaia, S. Dub, and L. Dubrovinsky, "Superior Wear Resistance of Aggregated Diamond Nanorods," *Nano Lett.*, vol. 6, pp. 824–826, 2006.

[110] M. Wiora, K. Brühne, A. Flöter, P. Gluche, T. M. Willey, S. O. Kucheyev, A. W. Van Buuren, A. V. Hamza, J. Biener, and H. J. Fecht, "Grain size dependent mechanical properties of nanocrystalline diamond films grown by hot-filament CVD," *Diamond and Related Materials*, vol. 18, pp. 927–930, 2009.

[111] S. A. Catledge, J. Borham, Y. K. Vohra, W. R. Lacefield, and J. E. Lemons, "Nanoindentation hardness and adhesion investigations of vapor deposited nanostructured diamond films," *Journal of Applied Physics*, vol. 91, pp. 5347–5352, 2002.

[112] J. F. Colomer, G. Bister, I. Willems, Z. Kónya, A. Fonseca, J. B. Nagy, and G. Van Tendeloo, "Synthesis of single-wall carbon nanotubes by catalytic decomposition of hydrocarbons," *Chemical Communications*, pp. 1343–1344, 1999.

[113] D. K. Singh, P. K. Iyer, and P. K. Giri, "Diameter dependence of interwall separation and strain in multiwalled carbon nanotubes probed by X-ray diffraction and Raman scattering

studies," *Diamond and Related Materials*, vol. 19, pp. 1281–1288, 2010.

[114] H. M. Heise, R. Kuckuk, A. K. Ojha, A. Srivastava, V. Srivastava, and B. P. Asthana, "Characterisation of carbonaceous materials using Raman spectroscopy: a comparison of carbon nanotube filters, single- and multi-walled nanotubes, graphitised porous carbon and graphite," *Journal of Raman Spectroscopy*, vol. 40, pp. 344–353, 2009.

APPENDIX A. PERMISSION FROM PUBLISHERS

Permission for figure 4.1 and 4.2

All payments must be made in full to CCC. For payment instructions, please see information listed at the bottom of this form.

License Number	3010250229134
Order Date	Oct 15, 2012
Publisher	American Institute of Physics
Publication	Journal of Chemical Physics
Article Title	Absorption, Ionization, and Ion-Fragmentation Cross Sections of Hydrocarbon Vapors under Vacuum-Ultraviolet Radiation
Author	Richard I. Schoen
Online Publication Date	Nov 1, 1962
Volume number	37
Issue number	9
Type of Use	Thesis/Dissertation
Requestor type	Student
Format	Print and electronic
Portion	Figure/Table
Number of figures/tables	2
Title of your thesis / dissertation	Low Temperature Deposition of Carbon Materials with Photo-Enhanced CVD
Expected completion date	Dec 2012
Estimated size (number of pages)	110
Total	0.00 USD

Permission for figure 4.3 and 4.4.

All payments must be made in full to CCC. For payment instructions, please see information listed at the bottom of this form.

Supplier	Elsevier Limited The Boulevard,Langford Lane Kidlington,Oxford,OX5 1GB,UK
Registered Company Number	1982084
Customer name	KyungNam Kang
Customer address	375 W. Roosevelt St. # 2223 Baton Rouge, LA 70802
License number	3026410660076
License date	Nov 12, 2012
Licensed content publisher	Elsevier
Licensed content publication	Journal of Quantitative Spectroscopy and Radiative Transfer
Licensed content title	Temperature-dependent photoabsorption cross sections in the VUV-UV region. I. Methane and ethane
Licensed content author	F.Z. Chen,C.Y.Robert Wu
Licensed content date	1 May 2004
Licensed content volume number	85
Licensed content issue number	2
Number of pages	15
Start Page	195
End Page	209
Type of Use	reuse in a thesis/dissertation
Intended publisher of new work	other
Portion	figures/tables/illustrations
Number of figures/tables/illustrations	2
Format	both print and electronic
Are you the author of this Elsevier article?	No
Will you be translating?	No
Order reference number	
Title of your thesis/dissertation	Low Temperature Deposition of Carbon Materials with Photo-Enhanced CVD
Expected completion date	Dec 2012
Estimated size (number of pages)	110
Elsevier VAT number	GB 494 6272 12
Permissions price	0.00 USD
VAT/Local Sales Tax	0.0 USD / 0.0 GBP
Total	0.00 USD

Permission for figure 4.5

All payments must be made in full to CCC. For payment instructions, please see information listed at the bottom of this form.

License Number	3010250381748
Order Date	Oct 15, 2012
Publisher	American Institute of Physics
Publication	Journal of Chemical Physics
Article Title	Vacuum-Ultraviolet Absorption Cross Sections of CO, HCl, and ICN between 1050 and 2100 Å
Author	James A. Myer, James A. R. Samson
Online Publication Date	Jan 1, 1970
Volume number	52
Issue number	1
Type of Use	Thesis/Dissertation
Requestor type	Student
Format	Print and electronic
Portion	Figure/Table
Number of figures/tables	1
Title of your thesis / dissertation	Low Temperature Deposition of Carbon Materials with Photo-Enhanced CVD
Expected completion date	Dec 2012
Estimated size (number of pages)	110
Total	0.00 USD

Permission for figure 4.6.

All payments must be made in full to CCC. For payment instructions, please see information listed at the bottom of this form.

Supplier	Elsevier Limited The Boulevard,Langford Lane Kidlington,Oxford,OX5 1GB,UK
Registered Company Number	1982084
Customer name	KyungNam Kang
Customer address	375 W. Roosevelt St. # 2223
	Baton Rouge, LA 70802
License number	3026410379619
License date	Nov 12, 2012
Licensed content publisher	Elsevier
Licensed content publication	Journal of Quantitative Spectroscopy and Radiative Transfer
Licensed content title	Temperature dependence of photoabsorption cross sections of carbon tetrachloride at 186–240 nm
Licensed content author	V. Prahlad,Vijay Kumar
Licensed content date	December 1995
Licensed content volume number	54
Licensed content issue number	6
Number of pages	11
Start Page	945
End Page	955
Type of Use	reuse in a thesis/dissertation
Intended publisher of new work	other
Portion	figures/tables/illustrations
Number of figures/tables/illustrations	1
Format	both print and electronic
Are you the author of this Elsevier article?	No
Will you be translating?	No
Order reference number	
Title of your thesis/dissertation	Low Temperature Deposition of Carbon Materials with Photo-Enhanced CVD
Expected completion date	Dec 2012
Estimated size (number of pages)	110
Elsevier VAT number	GB 494 6272 12
Permissions price	0.00 USD
VAT/Local Sales Tax	0.0 USD / 0.0 GBP
Total	0.00 USD

Permission for chapter 6.1 and 6.2. Author reuse.

All payments must be made in full to CCC. For payment instructions, please see information listed at the bottom of this form.

Supplier	Elsevier Limited The Boulevard,Langford Lane Kidlington,Oxford,OX5 1GB,UK
Registered Company Number	1982084
Customer name	KyungNam Kang
Customer address	375 W. Roosevelt St. # 2223 Baton Rouge, LA 70802
License number	2997990953223
License date	Sep 28, 2012
Licensed content publisher	Elsevier
Licensed content publication	Diamond and Related Materials
Licensed content title	Study on low temperature growth and formation mechanism of hexagonal diamond
Licensed content author	KyungNam Kang,Yoonyoung Jin,Jeonghwan Kim,Pratul K. Ajmera
Licensed content date	July–August 2012
Licensed content volume number	27–28
Licensed content issue number	
Number of pages	6
Start Page	76
End Page	81
Type of Use	reuse in a thesis/dissertation
Portion	full article
Format	both print and electronic
Are you the author of this Elsevier article?	Yes
Will you be translating?	No
Order reference number	
Title of your thesis/dissertation	Low Temperature Deposition of Carbon Materials with Photo-Enhanced CVD
Expected completion date	Dec 2012
Estimated size (number of pages)	110
Elsevier VAT number	GB 494 6272 12
Permissions price	0.00 USD
VAT/Local Sales Tax	0.0 USD / 0.0 GBP
Total	0.00 USD

VITA

KyungNam Kang was born in Pusan, South Korea, on December 1973. He graduated with his bachelor of science degree in physics department at Chung-Ang University, Seoul in August 1999. He studied biomedical engineering at Texas A&M University, College Station, for his Master of Engineering degree in December 2003. He obtained his Master of Science degree in electrical engineering at Louisiana State University (LSU), Baton Rouge, in December 2007. Since then he has been pursuing his doctoral degree at LSU.